eXPRESS Polymer Letters Vol.10, No.5 (2016) 360
Available online at www.expresspolymlett.com
DOI: 10.3144/expresspolymlett.2016.33

Editorial corner – a personal view
Challenges in fracture toughness modelling of nanocomposites

B. Lauke[1*], *J. Karger-Kocsis*[2]

[1]Leibniz-Institut für Polymerforschung Dresden e.V., Hohe Str. 6, D-01069 Dresden, Germany
[2]Department of Polymer Engineering, Faculty of Mechanical Engineering, Budapest University of Technology and Economics, MTA-BME Research Group for Composite Science and Technology, Műegyetem rkp. 3, H-1111 Budapest, Hungary

A basic question when modelling the fracture toughness of hybrid polymer composites is whether or not the particles' agglomerations are considered. Note that even in microparticle reinforced polymers the distribution of the particles is locally inhomogeneous because they get into contact as a consequence of production. In nanoparticle filled elastomers particles agglomerate and the agglomerates build even larger structures. Consequently, if we consider the close neighbourhood of a single particle there exists a much higher particle density than in larger distances. Such behaviour can be described for example by pair distribution functions (DOI: 10.1016/j.compositesb.2014.01.002). Close particles cause high stress or strain concentrations in the matrix in between. This fact must be considered in strength and fracture toughness modelling. Filled polymer composites have been studied extensively because of their technological and scientific importance (DOI: 10.1007/BF01160743; DOI: 10.016/j.compositesb.2008.01.002; DOI: 10.1016/0266-3538(88)90009-7). Generally, crack tip blunting, crack pinning, localized shear bands, debonding of particles as plastic voiding and localized plastic shear yielding were found to be responsible for the increase of toughness in thermoset composites. Models that consider such effects are able to describe some of the experimental results properly (DOI: 10.1007/s10853-009-4064-9; DOI: 10.1016/j.compscitech.2009.12.024). Also the effect of particle size on plastic void growth has been taken in account (DOI: 10.1016/j.mechrescom.2015.2.002). Homogeneous particle distribution cannot be expected in 'real' materials. Increased number of nearest neighbours in microparticle filled composites and agglomerate formation in nanocomposites must be considered. Stiffness is not influenced by these events because at small deformations no debonding occurs. However, if strength or fracture toughness are computed, such local heterogeneities should be considered. As basic mathematical and experimental data are available, the modelling should involve this structural level. In the first step any mathematical pair distribution function can be used to calculate the number of particles close to the chosen one in the ensemble. High stress concentration in between such a pair may initiate debonding. The ligament in between the debonded particles becomes unloaded and their outer region overloaded accompanied with yielding. Debonding does not contribute much to energy dissipation but triggers matrix yielding that enhances the toughness. Debonding of particles leads to a reduction of tensile strength, too.
Let us go in this direction to get a deeper understanding in the mechanical and fracture mechanical behaviours!

Dr. Bernd Lauke

Prof. Dr. Dr. h.c.
József Karger-Kocsis
Editor-in-Chief

*Corresponding author, e-mail: laukeb@ipfdd.de
© BME-PT

eXPRESS Polymer Letters Vol.10, No.5 (2016) 361–372
Available online at www.expresspolymlett.com
DOI: 10.3144/expresspolymlett.2016.34

The effect of PLGA-PEG-PLGA modification on the sol-gel transition and degradation properties

J. Oborná[1*], *L. Mravcová*[1], *L. Michlovská*[2], *L. Vojtová*[2], *M. Vávrová*[1]

[1]Institute of Chemistry and Technology of Enviromental Protection, Faculty of Chemistry, Brno University of Technology, Purkyňova 118, 612 00 Brno, Czech Republic
[2]Central European Institute of Technology, Technická 3058/10, 616 00 Brno, Czech Republic

Received 28 August 2015; accepted in revised form 23 November 2015

Abstract. This paper deals with the influence of an incubation medium pH on the hydrolytic degradation of a novel thermosensitive biodegradable triblock copolymer based on hydrophilic poly(ethylene glycol) and hydrophobic copolymer poly(lactic acid-*co*-glycolic acid) (PLGA-PEG-PLGA), consequently modified at α,ω-ends with itaconic acid (ITA) resulting in α,ω-itaconyl(PLGA-PEG-PLGA). Itaconic acid, obtained from renewable resources, delivers a reactive double bond and carboxylic functional group to the end of PLGA-PEG-PLGA copolymer: this is important for a reaction with biologically active substances. The suitability of the sample degradation was assessed depending on whether the copolymer formed a gel at 37 °C. Two reversible physical sol-gel-sol transitions from a sol (liquid phase) to a gel (solid phase) and back to a sol (suspension) were verified using the tube inverting method. The hydrolytical degradation was evaluated at a physiological temperature (37 °C) in the presence of phosphate solutions, at a pH of either 4.2 or 7.4 by monitoring the decrease of the number average molecular weight of copolymers by GPC. Moreover, the degradation kinetics was confirmed by the HPLC/DAD method, where the increasing amount of final degradation products (lactic and glycolic acids) was detected. The study demonstrated that the carboxylic groups modified copolymer (ITA/PLGA–PEG– PLGA/ITA) is more susceptible to hydrolytical degradation than the unmodified copolymer within first days of degradation at pH 7.4.

Keywords: *biodegradable polymers, degradation, itaconic acid, sol-gel transition, lactic acid*

1. Introduction

'Smart' polymers, based on synthetic linear aliphatic polyesters, have been known for many years. Over the years they have been used in numerous biomedical and pharmaceutical products. ReGel® is one such product, and is frequently cited. It contains tri-block copolymers, (based on poly(lactic acid), poly(glycolic acid) and poly(ethylene glycol) (PLGA-PEG-PLGA)) [1]. PLGA-PEG-PLGA (or ABA) hydrogel systems have played an important role in the development of controlled delivery devices for a variety of drug and food related bioactive ingredients [2]. The use of ABA example as a bioadhesive for the treatment of bone fractures has offered advantages. For example, copolymer which remains in the body during surgery does not cause chronic foreign body reaction. In addition, subsequent removal of the implant surgery is not necessary [3]. Furthermore, PLGA-PEG-PLGA gradually degrades to lactic and glycolic acids, which are natural metabolites of the human body. Gradual external heating of a solution of this copolymer forms a highly viscous gel. A crucial factor is the ratio of the hydrophobic (PLGA) and hydrophilic (PEG) components [4]. Reversible phase behaviors, i.e. the change from the liquid phase (sol) to the gel phase, and from the gel phase to sol phase (a suspension), were demonstrated for the ABA copolymer with a molecular weight of PLGA

*Corresponding author, e-mail: xcoborna@fch.vutbr.cz
© BME-PT

block from 900–1600 g·mol^{-1} [5]. This behavior depends on the concentration of the copolymer in the solution and an increase in the temperature, which can be easily verified using the inverting test tube method. This can be shown graphically using a sol-gel phase diagram [6–14]. 'Smart' hydrogels based on PLGA-PEG-PLGA have been developed primarily as stimuli-responsive materials, which can undergo volume changes in response to a change in temperature, when exposed to a biological target [1]. The use of PLGA-PEG-PLGA as drug delivery systems is, however, limited since the copolymer has a low degree of functionality (it contains only hydroxyl functional groups). For this reason, much attention is devoted to the PLGA-PEG-PLGA functionalization. Modification of the triblock copolymer end-chain structure by itaconic acid (α,ω-itaconyl (PLGA-PEG-PLGA) = ITA/PLGA–PEG–PLGA/ITA) was first reported by our group [18]. Itaconic acid belongs to the group of unsaturated organic carboxylic acid [15] and involving double bond in the structure forms macro monomers permitting easy copolymerization [16]. Ionized itaconic acid has two carboxyl groups with different *pKa* values (pKa_1 3.85 and 5.45): suitable for forming hydrogen 'bridges' [17]. Itaconic acid, derived from renewable sources like molasses and hydrolyzed starch, exhibits high biocompatibility [15] and biodegradability, the main degradation products are acetate, lactate and carbon dioxide [19]. Copolymers based on lactic and glycolic acids undergo hydrolytical degradation of unstable ester bonds in an aqueous environment either *in vitro* or *in vivo* [21]. Whereas the hydrolytic cleavage of the PLGA ester bond under basic conditions is irreversible and leads to hydroxyl group and acid salt, while acidic pH induces reversible hydrolysis resulting in one hydroxyl group and one carboxyl group capable of catalyzing the hydrolysis of other ester bonds [20]. Random chain cleavage results in a substantial reduction in molecular weight for high molecular weight polyesters in this stage, without a consequent loss of polymer mass. In the subsequent phase (erosion) reduction of the molecular weight is accompanied by a significant decrease in polymer weight, resulting in water soluble monomeric and oligomeric products which diffuse to the surface of the polymer material [21]. Numerous factors influence the degradation rate of polyester based copolymers. The most important factors include the size and shape of the object, temperature, pH and basic properties of the copolymer. It was confirmed that the degradation rate of these systems in an aqueous environment depends on the overall hydrophilicity of the copolymer [22]. The proposed work discussed the effect of PLGA-PEG-PLGA modification by bioactive renewable itaconic acid on the rate of copolymer hydrolytic degradation in different incubation media at 37 °C evaluated by the GPC method. The level and the rate of releasing degradation products (lactic and glycolic acid) was compared and interpreted.

2. Experimental section

2.1. Materials

Formic acid (puriss p.a., ≥98%) was obtained from Riedel-de Haën (Germany). 2,6-Di-tert-butyl-4-methylphenol, monopotassium phosphate, dipotassium phosphate, standard D,L-lactic acid 90% and chloroform-d ($CDCl_3$, 99.8 atom% D) were purchased from Sigma-Aldrich (Germany). Tetrahydrofuran (99.9%) and standard glycolic acid (puriss p.a.) were obtained Merck KGaA (Germany). Acetonitrile was procured from Penta (Czech Republic). Polystyrene standards EasyCal 580–377 400 g·mol^{-1} were purchased Polymer Laboratories (USA). All solvents were provided as HPLC grade.

2.2. Materials for copolymer synthesis

Poly(ethylene glycol) (PEG, M_n =1500 g·mol^{-1}, Sigma-Aldrich Germany) was thoroughly degassed under vacuum for 3 hours at 130 °C. D,L-lactide (LA, 99.9%, Polysciences, Pennsylvania), glycolide (GA, 99.9%, Polysciences, Pennsylvania) and itaconic anhydride (ITA 97 , Fluka, Switzerland) were sublimated under reduced pressure (10 Pa) prior to use. Stannous 2-ethylhexanoate (95%, Sigma-Aldrich, Germany) was used as received.

2.3. Copolymer synthesis and purification

The PLGA-PEG-PLGA (ABA) and ITA/PLGA–PEG–PLGA/ITA (ITA-ABA-ITA) tri-block copolymers with different PLGA/PEG weight ratios and LA/GA molar ratios were synthesized in 'one pot' via the ring opening polymerization (ROP) method in bulk under a nitrogen atmosphere [18]. Shortly, PEG, LA and GA were homogenized at 130 °C followed by injecting Sn(II)2-ethylhexanoate. Reaction ran over 3 hours. In following step, ITA was added to the mixture and functionalization proceeded at 110 °C.

Table 1. Copolymer characterization

Sample	Type	$Ratio_{THEOR.}$ PLGA/PEG [wt/wt]	$Ratio_{THEOR.}$ LA/GA [mol/mol]	Theoretical M_n [g·mol^{-1}]
ABA–2.5/3	ABA	2.50	3.00	5250
ABA–2/3	ABA	2.00	3.00	4500
ABA-ITA–2/3	ITA-ABA-ITA	2.00	3.00	4500
ABA-ITA–2/2.5	ITA-ABA-ITA	2.00	2.50	4500

Copolymers were purified three times from unreacted monomers by dissolving in cold water and heating the solution up to 80 °C. Precipitated polymers were separated by decantation and dried in vacuum oven at 30 °C until the constant weight (for approx. 12 h). Purity of the synthesized copolymers was verified by ^{1}H NMR spectroscopy as described elsewhere (Michlovská *et al*. [18]).
Theoretical copolymer characterizations are shown in Table 1.

2.4. NMR characterization

Molecular weight and polymer composition (ratio of PLGA/PEG and GA/LA) were determined by ^{1}H NMR spectroscopy on a 500 MHz Bruker AVANCE III instrument with TMS as internal standard using 128 scans in $CDCl_3$ solvent. Sample concentration was 20 mg/mL in $CDCl_3$.

2.5. Gel permeation chromatography

Number average molecular weight (M_n) and polydisperisity index (PDI) of the copolymer were determined by gel permeation chromatography using an Agilent 1100 Series equipped with an isocratic pump (Agilent 1100 Series), and operated at a flow rate of 1.0 mL/min with tetrahydrofuran (THF), a vacuum degasser, an autosampler (Agilent 1100 Series), a column oven and a refractive index detector (Agilent 1100 Series) with an integrated temperature controller maintained at 30 °C. For molecular mass separation a guard column PLgel Mixed C 50×7.5 mm, 5 μm (Polymer Laboratories, USA) and a column PLgel Mixed C 300×7.5 mm, 5 μm (Polymer Laboratories, USA) were used in-line. The temperature of the column and the detector were set to 30 °C. The THF (HPLC grade) mobile phase was stabilized with 2,6-Di-tert-butyl-4-methylphenol. 50 μL of polymer samples and standards were injected. Number average molecular weight was calculated from a calibration curve constructed on the basis of a series of polystyrene standards EasyCal 580–377 400 g·mol^{-1} (Polymer Laboratories, USA).

2.6. High performance liquid chromatography

Phosphate solutions collected after certain degradation times were analyzed on an Agilent 1100 Series equipped with a gradient pump (Agilent 1100 Series) operated at a flow rate of 0.2 mL/min, a vacuum degasser, an autosampler (Agilent 1100 Series), a column oven and a UV-VIS detector of diode array type. For the separation of lactic and glycolic acids, an in-line guard column Restek Aqueous C18 4×2 mm, 5 μm (Restek, USA) and a column Restek Aqueous C18 250×4.6 mm, 5 μm (Restek, USA) were used. 5 μL of samples and standards were injected. The temperature of the column oven was set to 30 °C. The mobile phase was a mixture of acetonitrile (ACN) and 0.01 M formic acid. Gradient mobile phases were as follows: 0 min.:1% of ACN, 10 min.:1% of ACN, 12 min.: 50% of ACN, 30 min.: 50% of ACN, 30.01 min.: 1% of ACN. Glycolic and lactic acids were detected at a wavelength of 210 nm.
The analytes in the standard mixture and in the various samples were identified by comparing the retention time of the relevant peaks with those of the corresponding standards injected separately. Quantification was carried out by integration of the peak areas using the external standard chromatographic method.

2.7. Sample preparation for GPC analysis

Sample incubation was terminated after the collection of 400 μL of phosphate solution. Each sample was frozen to –30 °C after incubation. The frozen samples were subsequently subjected to lyophilization. The lyophilization was carried out at –80 °C and at a pressure of 15 Pa for 24 hours at Freezone 4.5 Freeze Dry System (Labconco, USA). From each lyophilized sample approximately 5 mg of degraded copolymer was collected. This amount of copolymer was dissolved in 1 mL of tetrahydrofuran and then analyzed by gel permeation chromatography.

2.8. Determining the critical gel concentration and critical gel temperature

A simple method of inverting test tubes is used for the preparation of the sol-gel phase diagram. The

advantage of this method is that it is possible to observe colour transitions and the turbidity of the solutions during the experiment. The disadvantage of the method, however, is the very subjective response of each observer.

A set of polymer samples with different concentrations in water was prepared. The aqueous copolymer solution for each concentration was prepared by dissolving the PLGA-PEG-PLGA or ITA/PLGA–PEG–PLGA/ITA in de-ionized water. For the test tube inverting method, the 4 mL vials (diameter 1.1 cm) contain 3 mL of copolymer solution. Dissolution was carried out in cool box at 4 °C by occasional stirring for a few days until the copolymer completely dissolved. After dissolution, the vials were equilibrated to room temperature. Experiments were performed in a water bath. A warming-up water bath was set at room temperature (23 °C), and thereafter the temperature was gradually increased by 1 °C steps to 60 °C. After 5 minutes the samples were removed from the water bath and the test tubes were turned upside down to observe the change in viscosity and color of each sample. The critical gelation concentration (CGC) and the critical gelation temperature (CGT) of the copolymer, were then determined from the measurement results. The accuracy of the sol-gel transition temperature was ±1 °C.

2.9. Degradation experiment

PLGA-PEG-PLGA (ABA) copolymer and copolymer modified with itaconic acid (ITA-ABA-ITA) are very viscous, 'honey-like' materials. For sample preparation, it was necessary to weigh certain quantities of these copolymers for the weight concentration. For a certain amount of the copolymer, the calculated quantity of de-ionized water was added. The prepared samples were kept in a cool box. Dissolution was carried out with occasional stirring for a few days until the copolymer completely dissolved.

Different concentrations of PLGA-PEG-PLGA and ITA/PLGA–PEG–PLGA/ITA copolymer were prepared in order to determine the degree of degradation. 300 μL of stock copolymer solution was pipetted sol into 2 mL vials. The vials were kept subsequently in an incubator (Nüve cooled incubator EC 110, Turkey) at 37 °C until the solution became a gel. The resulting gel was then added to 700 μL of phosphate solution, which was preheated to 37 °C. Degradation was carried out in two environments: an acidic environment at a pH of 4.2; and a neutral environment at a pH of 7.4. 400 μL of phosphate solution was collected in the first day at the beginning of incubation. The collected solution was subsequently analyzed by high performance liquid chromatography with UV-VIS detection of diode array type. The rest of the hydrogel was frozen and lyophilized. Lyophilized rests samples were measured by GPC.

3. Results and discussion

3.1. Copolymer synthesis and characterization

Molar ratio of synthesis was selected based on a literature review about PLGA-PEG-PLGA triblock copolymers [4]. It was assumed that aqueous solutions of these copolymers will change to gel in the vicinity of the body temperature.

PEG, LA and GA were homogenized at 130 °C followed by injecting Sn(II)2-ethylhexanoate. Sn(II)2-ethylhexanoate was chosen for its low toxicity, approved by FDA. Molar ratio of catalyst to initiator was 0.029. Reaction ran over 3 hours. Yield of synthesized copolymers was in a range from 75 to 87%. In following step, ITA was added to mixture and functionalization proceeded at 110 °C.

The ITA/PLGA–PEG–PLGA/ITA triblock copolymers with weight ratio of PLGA/PEG equal to 2 and 2.5 and molar ratio of LA/GA equal 3 were synthesised in 'one pot' reaction (Figure 1) via the ring opening polymerization (ROP) method in bulk under a nitrogen atmosphere as described elsewhere (Michlovská *et al*., [18]).

The amount of end-capped ITA to the both ends of PLGA-PEG-PLGA and real M_n were determined by ^{1}H NMR spectroscopy. Spectra of PLGA-PEG-PLGA and ITA/PLGA–PEG–PLGA/ITA copoly-

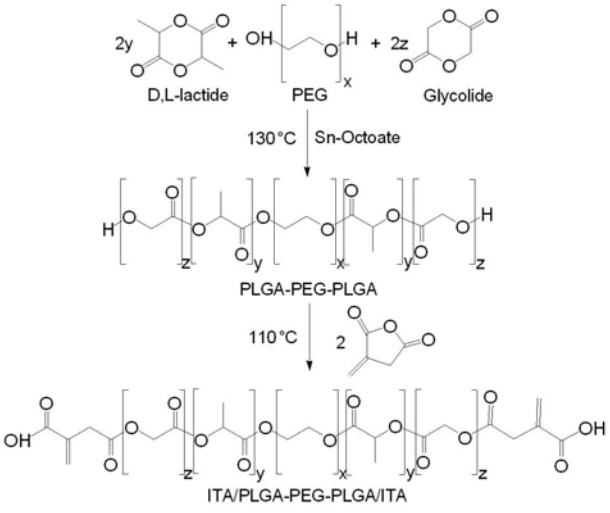

Figure 1. Scheme of PLGA-PEG-PLGA and ITA/PLGA-PEG-PLGA/ITA synthesis

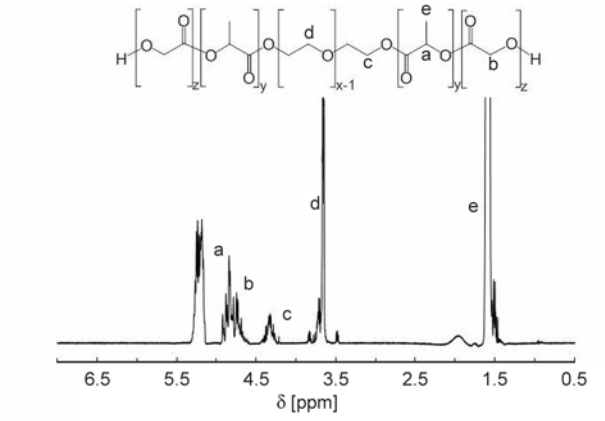

Figure 2. Proton NMR spectrum of PLGA-PEG-PLGA Sample ABA-2.5/3

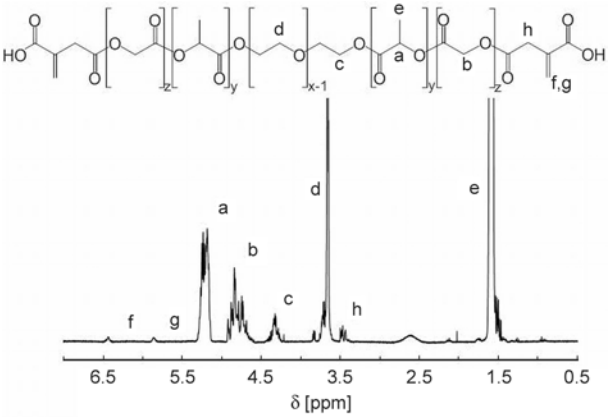

Figure 3. Proton NMR spectrum of ITA/PLGA–PEG–PLGA/ITA Sample ABA-ITA-2/3

mers are shown in Figure 2 and in Figure 3. From integrals of characteristic proton intensities of itaconic acid double bond ($OC(CH_2)CCH_2COOH$) at δ = 5.7–5.8 ppm (g), δ = 6.35–6.5 ppm (f), itaconic acid backbone ($OC\underline{H_2}(C=O)$) at δ = 3.40–3.44 ppm (h), lactic acid ($C–C\underline{H_3}(C=O)$) at δ = 1.5–1.65 ppm (e), glycolic acid ($OC\underline{H_2}O$) at δ = 4.6–4.9 ppm (b) and PEG ($OC\underline{H_2}C\underline{H_2}O$) at δ = 3.55 - 3.75 ppm (d).

3.2. The effect of ITA modification on sol-gel transition of PLGA-PEG-PLGA

Since the tested copolymers are not of commercial origin, first they were initially tested using a test tube inversion method to determine critical gelation temperature (CGT) and critical gelation concentration (CGC). For its use as a drug carries, it is necessary for the PLGA-PEG-PLGA copolymer to form a gel at a body temperature of 37 °C. Copolymers fulfilling this condition were subsequently subjected to degradation at 37 °C in phosphate solution at pH of either 7.4 or 4.2.

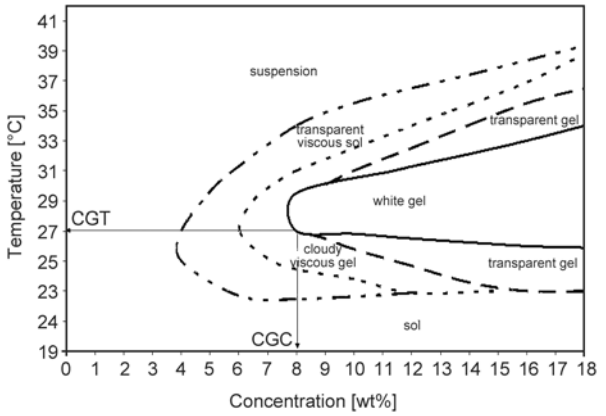

Figure 4. Phase diagram of the ABA-2.5/3

Overview of tested copolymers and their chemical compositions, CGC and CGT are described in Table 2.

The phase diagram of the aqueous solutions of ABA-2.5/3 determined by a test tube inverting method is shown in Figure 4. As it can be seen, several phase transitions and color changes during the gelation process have been observed. The critical gel concentration (CGC) above which white gel phase appears was about 8 wt%. The entire set of concentrations of the copolymer in water formed sol up to room temperature (23 °C). Lower concentrations from 4 to 12 wt% passed the more viscous sol when the temperature gradually increased. However, the solutions of concentration above 15 wt% passed straight to the transparent gel when temperature was higher than 23 °C. The transparent gel became turbid between 27 and 32 °C, indicating higher micelle aggregation. Further increase in temperature resulted in syneresis of the gel, and the system flows by gel-to-sol transition. The upper sol is a two-phase suspension at the temperature above the gel-to-sol transition.

Table 2. Experimental characteristics of tested copolymers

Sample	Type	$M_{n\ NMR}$ [g·mol^{-1}]	$Ratio_{REAL}$. PLGA/PEG [wt/wt]	$Ratio_{REAL}$. LA/GA [mol/mol]	$M_{n\ GPC}$ [g·mol^{-1}]	PDI	CGC [wt%]	CGT [°C]
ABA-2.5/3	ABA	4876	2.25	2.83	5949	1.28	8	27
ABA-2/3	ABA	4758	2.17	3.06	5845	1.26	6	38
ABA-ITA-2/3	ITA-ABA-ITA	4697	2.13	2.96	5557	1.35	6	36
ABA-ITA-2/2.5	ITA-ABA-ITA	4739	2.16	2.41	5209	1.27	18	40

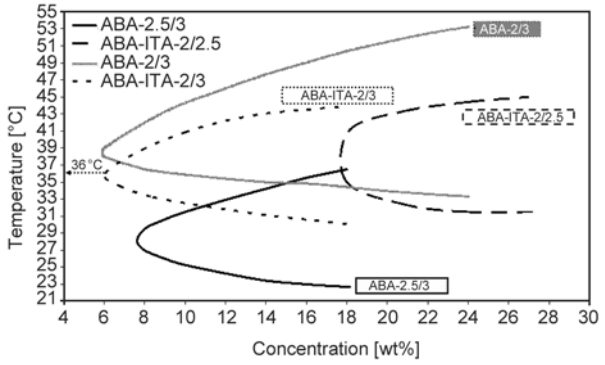

Figure 5. Phase diagrams of all samples

Sol-gel phase diagrams (describing just the area of both transparent and white gel) of all samples are shown in Figure 5.

From Figure 5 it is evident that decreasing the ratio of PLGA/PEG makes the entire copolymer less hydrophobic allowing poor micelles interaction and thus resulting in increasing CGT. By reducing ratio of LA/GA from 3 to 2.5 the CGC significantly increased which might be caused by PLA. PLA is more hydrophobic due to the methyl group than PGA. With decreasing LA/GA ratio the hydrophobicity of the whole copolymer is reduced (see Table 2).

3.3. The effect of ITA modification on hydrolytical degradation of PLGA-PEG-PLGA

The copolymers forming a gel in the temperature range from 36 °C to 38 °C meet our requirements and were selected for the use in the degradation experiment. Therefore, ABA-2.5/3 and ABA-2/3 (both type of PLGA-PEG-PLGA) and ABA-ITA-2/3 – copolymer (modified with itaconic acid) were selected for the degradation experiment. These samples safely fulfill the condition of gel formation – form a gel at a temperature of 36–38 °C. As for ABA-2.5/3 solution of 16 wt% was prepared. Dealing the ABA-2/3 and ABA-ITA-2/3 solutions of 16, 20 and 24 wt% were prepared for degradation study. Stock solutions of the copolymers were prepared in deionized water. Degradation was carried out in an incubator at 37 °C. Degradation media of both phosphate solution of pH value equal to 4.2 and phosphate buffer solution of pH value of 7.4 were used. The pH value of 7.4 was chosen as it is the pH of human blood. But all human organs do not have the same pH as the bloodstream. For example human vagina exhibits a slightly acidic pH (4±0.2). Linear polyesters degradation however is still pH dependent. It was tempting to try degradation of such copolymers in the mildly acidic and neutral environment and after that compared degradation of origin copolymer and modified copolymer.

3.3.1. Change in polymer length

Degradation of chains of the copolymer is proportional to the number average molecular weight (M_n) decrease. Gel permeation chromatography with a refractive index detector was used to determine the change in molecular weight and polydispersity index of the copolymer after its degradation.

Figure 6 shows the change in number molecular weight measured from 1st up to 10th day of degradation in pH 7.4 for 16 wt% water solution of ABA-ITA-2/3 at 37 °C. The measurement was provided until the gels were destroyed (11th day).

Figure 8 shows the change in number molecular weight measured from 1st up to 10th day of degradation in pH 7.4 for 16 wt% water solution of ABA-2/3 at 37 °C. The measurement was provided until the gels were destroyed (11th day) too.

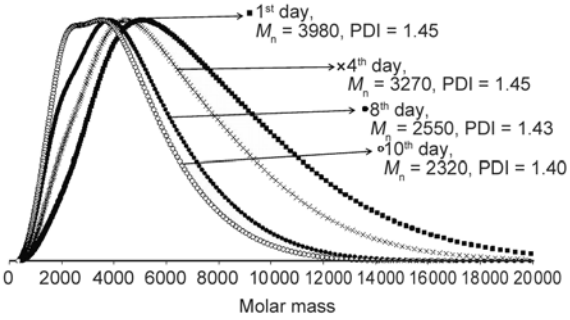

Figure 6. Molecular weight shift in the hydrolytic degradation in phosphate buffer solution pH value 7.4 for 16 wt% ABA-ITA-2/3

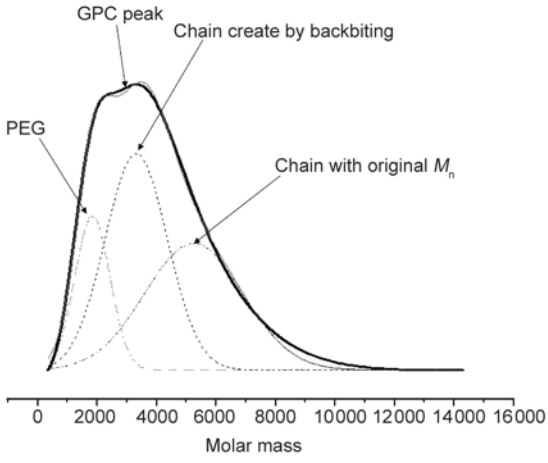

Figure 7. ABA-ITA-2/3 peak deconvolution for 10th day of degradation

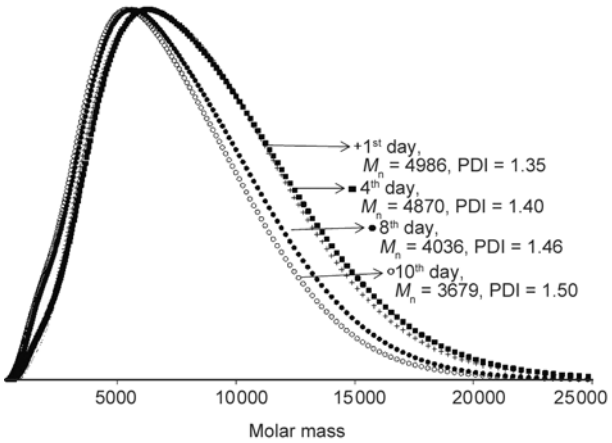

Figure 8. Molecular weight shift in the hydrolytic degradation in phosphate buffer solution pH value 7.4 for 16 wt% ABA-2/3

Decrease of number average molecular weight is evident in Figure 6. There is shown a noticeable shift peak top from right side (higher molecular weight) to left side (lower molecular weight). Formation of two maxima is possible to observe in 8th day although total M_n still decreases but PDI is still almost same. Degradation-mediated increase of acidic chain-ends causes the ester bond-scission to be faster in the chain-ends than in the internal bonds copolymer chain. Such a phenomenon is due to the short distance between the carbonyl and the alkoxy groups in the main chain making the cleavage of the ester bonds non-random under acidic conditions. Chain-end responsible for this backbiting mechanism is the hydroxyl-terminated chain-end within oligomers based on lactic acid. If all copolymer chains are cleaved by backbiting mechanism thus number average molecular weight of system is decreasing but chain distribution is still same (same PDI). Deconvolution of the peak for 8th day was performed using the software OriginPro 7.5. This deconvolution demonstrated that the peak contains three different long chains. This peak includes original copolymer chain and chain created by backbiting and polyethylene glycol chain. Two maxima are very perceptible in 10th degradation day. 10th day of degradation confirms this assertation (Figure 7).

M_n decrease is evident for ABA-2/3 in Figure 8. M_n decrease of ABA-2/3 is minimal for the first 4 days. ABA copolymer is more hydrophobic at pH 7.4 than ITA-ABA-ITA. The higher hydrophobicity of ABA decreases copolymer hydrolysis for the first days of degradation experiments.

3.3.2. The effect of degradation media pH

Influence of degradation media pH on the degradation progress of the copolymers was observed as a decrease of number average molecular weight M_n of the copolymer with time of degradation. Degradation time was evaluated in 5th and 10th day for all samples. For objective assessment of the overall course of the degradation most appropriate was to calculate the percent decrease in M_n because the initial molecular weight of the dissolved copolymer has never been the same at the start of experiments. The percentage decrease in copolymer molecular weight was interspersed as linear regression line. The percentage decrease of copolymer molecular weight for the selected time of degradation was calculated from the regression equation.

M_n decrease of ABA-2/3 in phosphate buffer solution having pH value 7.4 is shown in Figure 9. Influence the time on copolymer degradation was evaluated for each tested copolymer concentration as shows Figure 9. Time influence on copolymer degradation was confirmed for pH value 4.2 as well as. Further it is evident from Figure 9, that all tested sample concentrations are degraded in range of 16–18% until 5th day. This difference is almost insignificant. Degradation was found to be from 29 to 36% until 10th day in PBS (pH 7.4). Decrease in M_n behaved similar for medium pH value 4.2, where until 5th day the M_n degreased of about 10–15% and until 10th day in a range between 31–43%. It follows that there is no significant influence of copolymer weight concentration on hydrolytic degradation. Figure 9 shows too 5th degradation day for ABA-2/3 for incubation media pH value 4.2 and for all tested weight concentrations. It is evident that pH influence has not been con-

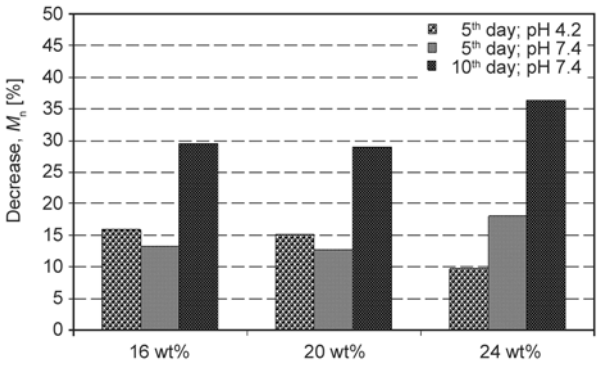

Figure 9. The effect of time, copolymer concentration of ABA-2/3 and pH of incubation media on the decrease of M_n during the degradation until 5th and 10th day

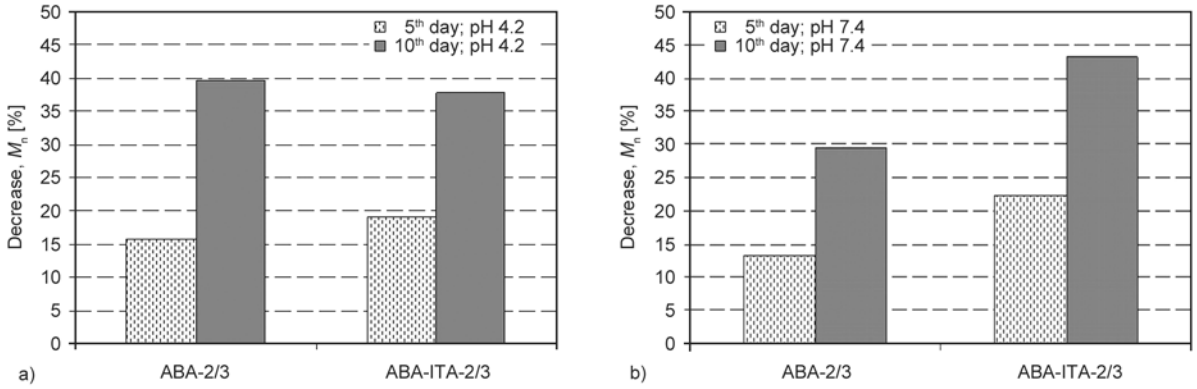

Figure 10. (a) Comparative degradation of 16 wt% ABA-2/3 versus 16 wt% ABA-ITA-2/3 at pH 4.2, (b) comparative degradation of 16 wt% ABA-2/3 versus 16 wt% ABA-ITA-2/3 at pH 7.4

firmed for unmodified PLGA-PEG-PLGA copolymer degradation.

The influence of the ratio of PLGA/PEG on decrease number average molecular weight of copolymer for samples ABA-2.5/3 (PLGA/PEG = 2.5) and ABA-2/3 (PLGA/PEG = 2.0) has not been confirmed. This low difference in degradation of both samples might be caused by little difference in PLGA/PEG ratio where for ABA-2.5/3 the real ratio is 2.25 and for ABA-2/3 the real ratio is 2.17.

Further influence of copolymer modification by itaconic acid is seen in Figure 10 where 16 wt% ABA-2/3 and 16 wt% ABA-ITA-2/3 are compared. It is evident that ABA-ITA-2/3 degraded faster at pH 7.4 (Figure 10b). Dissociation of carboxyl groups reduces the whole copolymer hydrophobicity in the aqueous environment at pH 7.4 and thus it leads to hydrophobic bonds decomposition. This causes more rapid degradation of the copolymer at pH 7.4. Conversely, carboxyl groups are not ionized at low pH. These carboxyl end groups are able of forming hydrogen bonds and thus the whole copolymer behaves more hydrophobic. Therefore, samples of the ABA-2/3 and ABA-ITA-2/3 degrade almost equally at pH 4.2 (Figure 10a).

3.3.3. Lactic and glycolic acid release

The release of lactic and glycolic acids into the incubation medium within the degradation process was quantitatively determined by High Performance Liquid Chromatography (HPLC) with UV-VIS detection of diode-array type (DAD). Increasing the concentration of lactic acid and glycolic acid in the solution was monitored during degradation. Individual analytes were evaluated using the calibration dependence of peak areas to concentrations of individual acids. The calibration solutions were prepared as a mixed standard of glycolic acid and lactic acid. Standards concentrations in calibration solution was ranged between 0.01–7.0 mg·mL^{-1}. For the standard curves, good linearity was observed with correlation factors typically above 0.99.

The limit of detection (LOD) and limit of quantification (LOQ) was calculated from the noise of the baseline. Limit of detection is the concentration the response of the detector will have a signal to noise ratio greater than 3. LOD was calculated according to the Equation (1). Limit of quantification is the concentration the response of the detector will have a signal to noise ratio greater than 10. LOQ was calculated according to the Equation (2). The limit of detection was determined 0.0044 mg·mL^{-1} of glycolic acid the limit of quantification was determined 0.0146 mg·mL^{-1} of glycolic acid. *LOD* was determined 0.0048 mg·mL^{-1} of lactic acid. *LOQ* was determined 0.0162 mg·mL^{-1} of lactic acid (Equations (1) and (2)):

$$LOD\,[\mathrm{mg{\cdot}mL^{-1}}] = 3\left(\frac{c[\mathrm{mg{\cdot}mL^{-1}}]}{\frac{S}{N}}\right) \quad (1)$$

$$LOQ\,[\mathrm{mg{\cdot}mL^{-1}}] = 10\left(\frac{c[\mathrm{mg{\cdot}mL^{-1}}]}{\frac{S}{N}}\right) \quad (2)$$

Glycolic acid is not detected during the first days of degradation especially in samples with low weight concentration. This is due to the actual ratio of glycolic acid and lactic in copolymer structure. The theoretical ratio of PLA/PGA was 3.0 for tested the samples. Lactic acid was nearly always detected after the first day of degradation in contrast to glycolic acid. This is probably due to the beginning of the copolymer degradation during preparation of samples –

xerogel dissolution in de-ionized water. Glycolic acid probably should be released in this way, but due to its low ratio in the copolymer, its concentration was below the limit of detection. In order to be compared release of both acids.

Acids release is controlled by first-order kinetics. Acid release kinetics is described by Equations (3)–(6). Rate constant (k) was calculated from the linear regressions. Example for 16 wt% sample ABA-2/3 and releasing for lactic acid at pH 4.2 shows Figure 11.

$$-\frac{\mathrm{d}C_{\mathrm{acid}}}{\mathrm{d}t} = k \cdot C_{\mathrm{acid}} \tag{3}$$

$$-\frac{\mathrm{d}C_{\mathrm{acid}}}{\mathrm{d}t} = k \cdot (C_0 - C_{\mathrm{release}}) \tag{4}$$

$$\frac{\mathrm{d}C_{\mathrm{acid}}}{(C_0 - C_{\mathrm{release}})} = k \cdot \mathrm{d}t \tag{5}$$

$$\ln\frac{\mathrm{d}C_0}{(C_0 - C_{\mathrm{release}})} = -k \cdot t \tag{6}$$

where the following notation was used (Equations (7)–(11)):

$$C_0 = \frac{n_{\mathrm{acid}}}{V_{\mathrm{copolymer\ solution}}} [\mathrm{mol \cdot L^{-1}}] \tag{7}$$

$$n_{\mathrm{acid}} = \frac{C_{\mathrm{max}}\mathrm{Acid}}{M_{\mathrm{acid}}} [\mathrm{mol}] \tag{8}$$

$$C_{\mathrm{max}}Acid = \frac{m_{\mathrm{mer}}}{M_{\mathrm{mer}}} \cdot M_{\mathrm{acid}} [\mathrm{g}] \tag{9}$$

$$m_{\mathrm{mer}} = \frac{m_{\mathrm{PLGA}} \cdot M_{\mathrm{mer}}}{\frac{M_{\mathrm{lactide}} + M_{\mathrm{glycolide}}}{\mathrm{ratio\ LA/GA}}} [\mathrm{g}] \tag{10}$$

$$m_{\mathrm{PLGA}} = \frac{m_{\mathrm{copolymer\ in\ 300}\mu\mathrm{L}}}{\mathrm{ratio\ LA/GA}} \cdot \mathrm{ratio\ PLGA/PEG\ [g]} \tag{11}$$

where C_{acid} lactic or glycolic acid concentration, k rate constant [h^{-1}], t time [h], C_0 acid initial concentration in copolymer, C_{release} acid actual molar concentration in phosphate solution, n_{acid} acid molar amount, M_{acid} acid molar mass, C_{max}Acid maximal acid concentration when copolymer fully degraded, m_{mer} amount of lactide or glycolide, M_{mer} lactide or glycolide molar mass, m_{PLGA} PLGA amount.

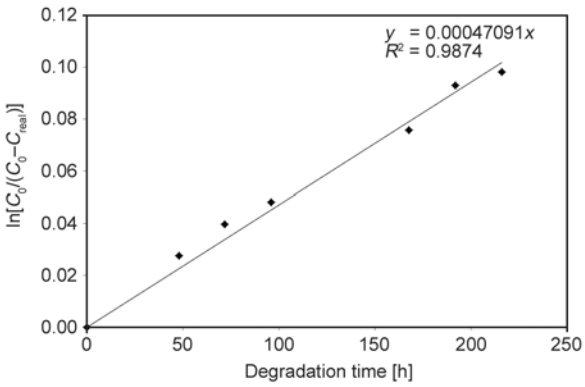

Figure 11. Linear regression and rate constant for lactic acid, sample 16 wt% ABA-2/3, pH 4.2

Figure 12 shows ABA-2/3 and its released acids. It is obvious that influence of copolymer weight concentration on released acids has not been confirmed.

Rate of release is faster for glycolic acid compared to lactic acid both tested pH. Major reason for faster releasing of glycolic acid that glycolic acid is more hydrophilic than lactic acid. Further lactic acid required more time for releasing 5% acid at buffer solution pH value 4.2. This was not confirmed with regard to the calculated rate constants k, R^2 linear regressions for glycolic acid were 0.8. The release of glycolic acid does not take place first-order reaction (ideal model). The acidic hydrolysis takes place at pH 4.2 but low pH environment causes that the cleaved acids create quite stable dimers. Therefore, the kinetics of acids release is slower than at pH 7.4 which take place by backbiting mechanism.

Figure 13 shows ABA-2/3 and glycolic acid releasing. The data within the interval from 100 to 160 hours were not recorded but 3 points are enough for linear regression. Glycolic acid is released steeper for phosphate buffer solution pH value 7.4. Glycolic acid is released within the range 40–48 % for 264 hours in

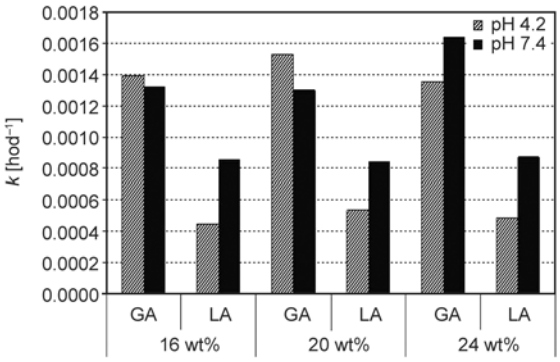

Figure 12. The effect of weight concentration ABA-2/3 and pH influence to acids release

phosphate buffer solution pH value 7.4. Opposite glycolic acid is released within the range 20–22 % only for the same time in phosphate solution pH value 4.2.

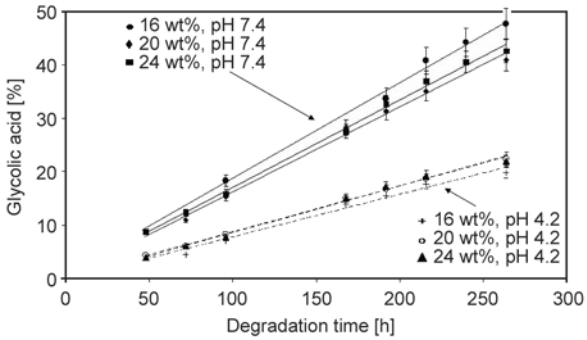

Figure 13. The influence pH value on releasing glycolic acid for ABA-2/3

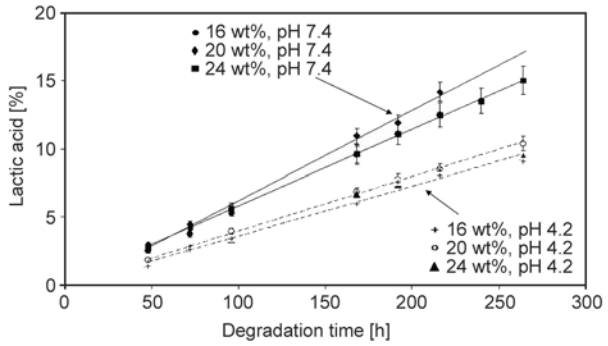

Figure 14. The influence pH value on releasing lactic acid for ABA-2/3

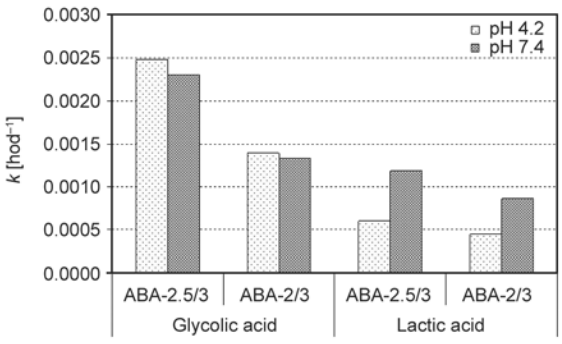

Figure 15. The influence ratio PLGA/PEG for 16 wt% ABA-2.5/3 (PLGA/PEG = 2.5) and 16 wt% ABA-2/3 (PLGA/PEG = 2.0)

Figure 14 shows ABA-2/3 and lactic acid releasing. Lactic acid is released steeper for phosphate buffer solution pH value 7.4. Lactic acid is released 15% for 264 hours in phosphate buffer solution at pH 7.4. Opposite lactic acid is released 9% only for the same time in phosphate solution at pH 4.2.

Figure 15 shows 16 wt% ABA-2.5/3 in compared 16 wt% ABA-2/3. At first sight copolymers are degraded 'worse' in the environment of phosphate solution at pH value 4.2 for lactic acid again. The release kinetics of acids is again influenced by the formation of oligomers at pH 4.2. However assumption that more hydrophobic ABA-2.5/3 will require more time for releasing acids, it wasn't confirm. It could be caused that acids are released during samples preparing and create a strongly acidic interior to the copolymer which can auto-catalyze degradation.

Figures 16 show ABA-2/3 and ABA-ITA-2/3 in environment at pH 4.2. The influence of modification by itaconic acid is observed on released glycolic acid and lactic acid. It is evident that ABA-ITA-2/3 needs more time for release of acids than unmodified ABA-2/3. ABA-ITA-2/3 contains carboxyl end groups are not ionized at low pH (3±1). The unionized carboxyl groups may create hydrogen bonding

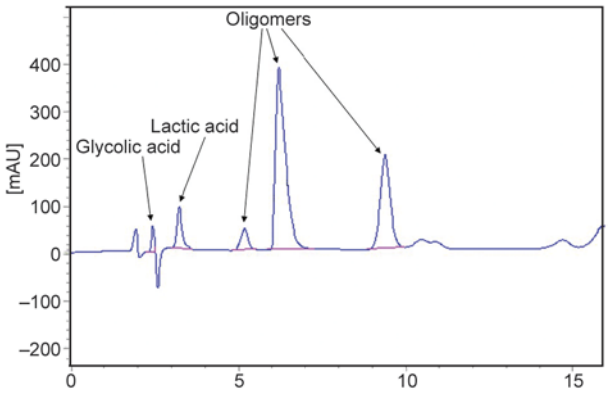

Figure 17. HPLC chromatogram of sample taken at degradation of the 24 wt% ABA-ITA-2/3 at pH 4.2

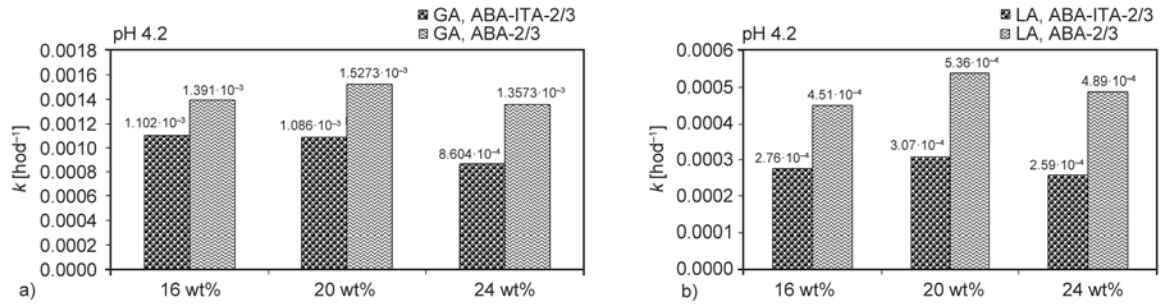

Figure 16. (a) The comparison of ABA-ITA-2/3 and ABA-2/3 for glycolic acid kinetics at pH 4.2 (b) the comparison of ABA-ITA-2/3 and ABA-2/3 for lactic acid kinetics at pH 4.2

and thus the whole copolymer behaves more hydrophobic. ABA-ITA-2/3 degradation and acids release are slower. Degradation occurs by acidic hydrolysis. The low pH environment supports the formation of oligomers, of course. This is shown in Figure 17. At pH 7.4 the release of acids is fast and very similar for both types of samples.

4. Conclusions

Functionalization of PLGA-PEG-PLGA copolymer by both carboxyl groups and double bonds coming from itaconic acid for bioactivity enhancement maintains reversible sol-gel transition behaviors and at certain composition keeps gelation at 37 °C. Their hydrolytical degradation at 37 °C was affected by the incubation medium. In phosphate solution at physiological pH equal to 7.4 the modified copolymer degraded significantly faster than its unmodified copolymer. This is due to the presence of carboxyl end groups, which are ionized at this pH thus increasing the hydrophilic nature. Conversely, at more acidic pH 4.2 carboxyl end groups are not ionized but create hydrogen bonding and thus the whole copolymer behaves more hydrophobic and the ITA-ABA-ITA degradation proceeded a bit slower than that of ABA. Anyhow, the hydrolytical stability of all samples has not exceeded 11 days.

The overall release of glycolic acid from the copolymer hydrogels was higher than the release of lactic acid due to the more hydrophilic character; however at pH 4.2 the acid release was slower since low pH supports the formation of oligomers (dimers, etc.).

Prepared ITA functionalized copolymers having carboxyl groups for bioactive molecules grafting and double bonds supporting chemical crosslinking are proved to be suitable materials for injectable drug delivery carriers, cells and gene scaffolds for tissue engineering as well as biodegradable hydrogels for tissue regeneration.

Acknowledgements

This work was supported by the Ministry of Education, Youth and Sports of the Czech Republic, specific research, No. FCH-S-15_2869 and project 'CEITEC – Central European Institute of Technology' (CZ.1.05/1.1.00/02.0068) from European Regional Development Fund.

References

[1] Zenter G. M., Rathi R., Shih C., McRea J. C., Seo M-H., Oh H., Rhee B. G., Mestecky J., Moldoveanu Z., Morgan M., Weitman S.: Biodegradable block copolymers for delivery of proteins and water-insoluble drugs. Journal of Controlled Release, **72**, 203–215 (2001). DOI: 10.1016/S0168-3659(01)00276-0

[2] Rizzarelli P., Carroccio S.: Modern mass spectrometry in the characterization and degradation of biodegradable polymers. Analytica Chimica Acta, **808**, 18–43 (2014). DOI: 10.1016/j.aca.2013.11.001

[3] Vadgama P.: Surface and interfaces for biomaterials. Woodhead, Cambridge (2005).

[4] Shim M. S., Lee H. T., Shim W. S., Park I., Lee H., Chang T., Kim S. W., Lee D. S.: Poly(D,L-lactic acid-*co*-glycolic acid)-*b*-poly(ethylene glycol)-*b*-poly(D,L-lactic acid-*co*-glycolic acid) triblock copolymer and thermoreversible phase transition in water. Journal of Biomedical Materials Research, **61**, 188–196 (2002). DOI: 10.1002/jbm.10164

[5] Jeong J. H., Lim D. W., Han D. K., Park T. G.: Synthesis, characterization and protein adsorption behaviors of PLGA/PEG di-block *co*-polymer blend films. Colloids and Surfaces B: Biointerfaces, **18**, 371–379 (2000). DOI: 10.1016/S0927-7765(99)00162-9

[6] Jeong B., Bae Y. H., Kim S. W.: Thermoreversible gelation of PEG-PLGA-PEG triblock copolymer aqueous solutions. Macromolecules, **32**, 7064–7069 (1999). DOI: 10.1021/ma9908999

[7] Qiao M., Chen D., Ma X., Liu Y.: Injectable biodegradable temperature-responsive PLGA-PEG-PLGA copolymers: Synthesis and effect of copolymer composition on the drug release from the copolymer-based hydrogels. International Journal of Pharmaceutics, **294**, 103–112 (2005). DOI: 10.1016/j.ijpharm.2005.01.017

[8] Gong C., Shi S., Wu L., Gou M., Yin Q., Gou Q., Dong P., Zhang F., Luo F., Zhao X., Wei Y., Qian Z.: Biodegradable *in situ* gel-forming controlled drug delivery system based on thermosensitive PCL-PEG-PCL hydrogel. Part 2: Sol-gel-sol transition and drug delivery behavior. Acta Biomaterialia, **5**, 3358–3370 (2009). DOI: 10.1016/j.actbio.2009.05.025

[9] Gao Y., Sun Y., Ren F., Gao S.: PLGA-PEG-PLGA hydrogel for ocular drug delivery of dexamethasone acetate. Drug Development and Industrial Pharmacy, **36**, 1131–1138 (2010). DOI: 10.3109/03639041003680826

[10] Yu L., Chang G., Zhang H., Ding J.: Temperature-induced spontaneous sol-gel transitions of poly(D, L-lactic-*co*-glycolic acid)-*b*-poly(ethylene glycol)-*b*-poly (D, L-lactic-*co*-glycolic acid) triblock copolymers and their end-capped derivatives in water. Journal of Polymer Science Part A: Polymer Chemistry, **45**, 1122–1133 (2007). DOI: 10.1002/pola.21876

[11] Yu L., Zhang Z., Ding J.: Influence of LA and GA sequence in the PLGA block on the properties of thermogelling PLGA-PEG-PLGA block copolymers. Biomacromolecules, **12**, 1290–1297 (2011).
DOI: 10.1021/bm101572j

[12] Yu L., Ci T., Zhou S., Zeng W., Ding J.: The thermogelling PLGA-PEG-PLGA block copolymer as a sustained release matrix of doxorubicin. Biomaterials Science, **1**, 411–420 (2013).
DOI: 10.1039/C2BM00159D

[13] Chang G., Yu L., Yang Z., Ding J.: A delicate ionizable-group effect on self-assembly and thermogelling of amphiphilic block copolymers in water. Polymer, **50**, 6111–6120 (2009).
DOI: 10.1016/j.polymer.2009.10.036

[14] Yu L., Zhang Z., Zhang H., Ding J.: Mixing a sol and a precipitate of block copolymers with different block ratios leads to an injectable hydrogel. Biomacromolecules, **10**, 1547–1553 (2009).
DOI: 10.1021/bm900145g

[15] Willke T., Vorlop K-D.: Biotechnological production of itaconic acid. Applied Microbiology and Biotechnology, **56**, 289–295 (2001).
DOI: 10.1007/s002530100685

[16] Chen K-S., Ku Y-A., Lin H-R., Yan T-R., Sheu D-C., Chen T-M., Lin F-H.: Preparation and characterization of pH sensitive poly(*N*-vinyl-2-pyrrolidone/itaconic acid) copolymer hydrogels. Materials Chemistry and Physics, **91**, 484–489 (2005).
DOI: 10.1016/j.matchemphys.2004.12.037

[17] Tomić S. L., Mićić M. M., Dobić S. N., Filipović J. M., Suljovrujić E. H: Smart poly(2-hydroxyethyl methacrylate/itaconic acid) hydrogels for biomedical application. Radiation Physics and Chemistry, **79**, 643, 649 (2010).
DOI: 10.1016/j.radphyschem.2009.11.015

[18] Michlovská L., Vojtová L., Mravcová L., Hermanová S., Kučerík J., Jančář J.: Functionalization conditions of PLGA-PEG-PLGA copolymer with itaconic anhydride. Macromolecular Symposia, **295**, 119–124 (2010).
DOI: 10.1002/masy.200900071

[19] Adler J., Wang S. F., Lardy H. A.: The metabolism of itaconic acid by liver mitochondria. Journal of Biological Chemistry, **229**, 865–879 (1957).

[20] de Jong S. J., Arias E. R., Rijkers D. T. S., van Nostrum C. F., Kettenes-van den Bosch J. J., Hennink W. E.: New insights into the hydrolytic degradation of poly (lactic acid): Participation of the alcohol terminus. Polymer, **42**, 2795–2802 (2001).
DOI: 10.1016/S0032-3861(00)00646-7

[21] Šnejdrová E., Dittrich M.: Poly(α-hydroxy acid) as drug carriers (in Czech). Chemické Listy, **105**, 27–33 (2011).

[22] Park T. G.: Degradation of poly(D,L-lactic acid) microspheres: Effect of molecular weight. Journal of Controlled Release, **30**, 161–173 (1994).
DOI: 10.1016/0168-3659(94)90263-1

eXPRESS Polymer Letters Vol.10, No.5 (2016) 373–380
Available online at www.expresspolymlett.com
DOI: 10.3144/expresspolymlett.2016.35

Thermal conductivity of plasma modified polyethylene terephthalate and polyamide-6 layers

G. Kalácska[1], R. Keresztes[1], L. Földi[1], Sz. Klébert[2], Z. Károly[2], L. Zsidai[1]*

[1]Institute for Mechanical Engineering Technology, Szent István University, Páter Károly u.1, H-2100 Gödöllő, Hungary
[2]AKI, Research Centre for Natural Sciences, Magyar tudósok krt. 2., H-1117, Budapest, Hungary

Received 23 September 2015; accepted in revised form 2 December 2015

Abstract. Tribological performance of the materials greatly depends on the temperature of the contacting zones and surfaces and hence on the heat conducting behaviour of the materials. Heat conduction of polymers is, however, greatly affected even by a very narrow (few tens of nm) modified layer formed on the surface after subjecting the polymer to plasma treatment. In this article the heat flow inhibiting properties of plasma modified surface layers were investigated on polyethylene terephthalate (PET) and polyamide-6 (PA6) engineering polymers. Nitrogen Plasma Immersion Ion Implantation gave rise to compositional and structural changes of the polymers in a depth of 110 nm. It was found that even this thin layer exhibited significant heat flow inhibiting effect. The modified layer considerably decreased the thermal conductivity coefficient of the treated polymer and resulted in a reduced heat transmission for PET and PA6 by 33 and 28%, respectively. This new information supports and is in accordance with the former tribological results about extra friction heat generation experienced under NPIII surface layer of PA6 and PET during dry sliding.

Keywords: *thermal properties, surfaces, adhesion, ion implantation, tribology*

1. Introduction

There is an increasing tendency to replace metal components by various kinds of engineering plastics [1]. The application of polymers for sliding parts is beneficial due to their corrosion resistance, damping characteristics and self-lubricating abilities [2]. Their use can reduce the maintenance costs, too. Several studies on the tribological behaviour of the most common engineering plastics [polyamides (PA) [3], polyoxymethylene (POM) [4] and polyethylene terephtalate with polytetrafluoroethylene (PET/PTFE) [5] in contact with steel have been published and compared by, e.g., Tanaka [6], Evans and Senior [7], Guezmil *et al*. [8] and Kalácska [1].

Polymers as viscoelastic materials are greatly sensitive to the heat of friction. During sliding ca. 90–95% of the mechanical energy is transformed to heat [9]. The velocity of sliding affects wear and friction through the temperature of the contacting surfaces. At high sliding velocities the increased surface roughness increases the friction coefficient and consequently the interface temperature, too [10, 11]. The thermal state of contact points is often decisive on the evaluation of frictional materials. Control of temperature at the polymer contact zone is of the highest importance to ensure beneficial wear and friction behaviour, because any increase in temperature may induce changes in the material bulk properties [12, 13] and polymer transfer processes. The thermal behaviour of the counter-surface could be also crucial for the temperature and tribological performance of the contact surfaces. Frictional metallic surfaces commonly possess good thermal conductivity and thus they can promote elimination of excessive heat. Metal surfaces, however, are commonly coated with metallic or ceramic layers or high hardness

*Corresponding author, e-mail: klebert.szilvia@ttk.mta.hu
© BME-PT

thin films [14–17], to increase their wear resistance. It was found that dry adhesion sliding can significantly increase the surface temperature because of the heat inhibiting effect of the surface layer. Not only metal parts are coated but surfaces of various polymers are also commonly modified [18, 19] to obtain an enhanced wear resistant outer surface layer having elevated hardness. Large number of papers have been published on plasma immersion ion implantation (PIII) modified polymers over the last decade and the results are summarized in a few review articles [20–23]. The research in this area focused mainly on the chemical, mechanical and morphological properties of PIII-modified polymer surfaces [24], but properties including wettability, electrical resistance and medical applicability were also investigated [25]. Surface treatment induce compositional and structural changes in the polymer in quite a limited depth (usually 20–100 nm) only, but even this thin modified layer exhibits more favourable – mechanical – properties. There is very limited information available, if any, about the thermal behaviour of this layer even though it can play a crucial role on the contact temperature of the plasma treated polymers and ultimately on the tribological properties, as well. This was confirmed by our former studies [26, 27], in which we investigated the tribological characters of plasma treated polymers (PET and PA6) by pin-on-disc method. We proved that under water- and oil lubricated conditions the NPIII layer formed on PA6 can be advantageous in enhancing the lubricating effects [26]. Similar phenomenon was discovered in hip-joint application having synovial lubricating liquid on NPIII treated UHMW-PE surfaces [28, 29] and transferred to engineering practice (coated joints are produced). Under dry sliding the tribological results of NPIII layer formed on PA6 and PET were not so convincing [26, 27].We showed for both polymer types that under dry sliding conditions at higher '*pv*' values (>0.1 MPa·ms^{-1}) there was substantial difference in the sample temperature between the surface treated and untreated polymers, although the changes of the frictional coefficient did not imply such temperature difference. We attributed the finding to the heat inhibiting effect of the modified surface layer. In the present paper we report about a special experiment to confirm our previous hypothesis. Tests were performed on PET and PA6 engineering polymers, the tribological properties of which are of greater significance and were the objects in our former investigations, too.

2. Experimental

Heat flow inhibiting effect of thin layers was investigated by comparing the surface treated and untreated polyethylene terepthalate (PET) and polyamide 6 (PA6) using updated shielding test method already introduced elsewhere [30]. Commercial extruded PA6 and PET rods with diameter of 15 mm manufactured by Ensinger GmbH, supplied by Quattroplast Ltd (Hungary) were used. The disc-shaped sample with a diameter of 10 mm were machined with a thickness of 2 mm. Before the NPIII treatment the samples were polished on wet SiC papers (grit numbers P1200 and P4000) and on felt sheet and were subsequently cleaned in ultrasonic bath of distilled water and of 96% ethanol. The samples were dried in pure nitrogen flow then treated by nitrogen plasma immersion ion implantation (N PIII) in a single run. The base pressure in the chamber was $4 \cdot 10^{-4}$ Pa. A 27.13 MHz RF plasma generator was applied (Dressler, Germany). High purity (4.5) N_2 was used with a flow rate of 25 cm^3·min^{-1} (STP), radiofrequency power of 75 W. The PIII treatment of the samples was performed by a high voltage pulser (ANSTO, Australia) with an accelerating voltage of 30 kV, ion fluence of $3 \cdot 10^{-17}$ cm^{-2} and fluence rate of $5 \cdot 10^{13}$ cm^{-2}·s^{-}1.

Surface composition of the modified layer was determined by XPS (X-ray photoelectron spectroscopy) analysis by a Kratos XSAM800 spectrometer using MgK$\alpha_{1,2}$ radiation and fixed analyser-transmission mode (using 80 and 40 eV pass energies for survey and detailed spectra, respectively). The thickness of plasma modified layer was estimated by the commonly used SRIM program [26].

Experimental set-up of heat flow tests is presented on Figure 1. Both the treated and untreated samples were heated by heat jet of 100 °C initial temperatures through the bore of a POM-C heat insulating plate having a diameter of 9 mm and thickness of 10 mm. The two sets of heating distance (L_2 = 8 mm and L_3 = 20 mm from the upper level of the insulating plate) resulted in different T_s temperatures (Figure 1b). The nozzle of the heat jet was fixed on the precision stand of a Mitutoyo bench, whereas the sample along with the POM C insulator plate were mounted on a 15 mm thick PA66-GF30 insulator that was laid on

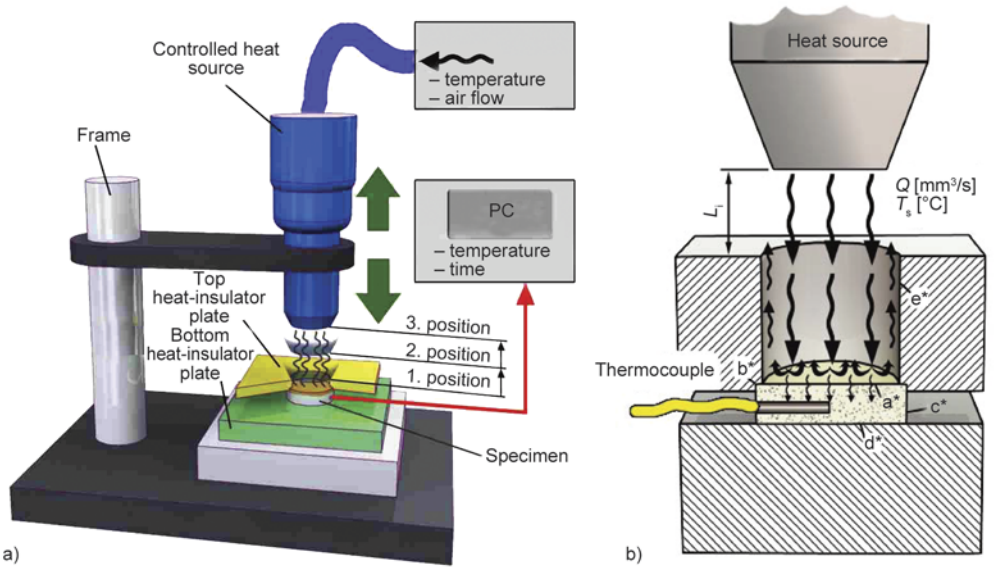

Figure 1. (a–b) Experimental set-up for the measurement of heat inhibiting effect of the PIII layer

a granite base. The 2 mm thick sample discs were centred at the bottom of the upper heat insulator plate in a 0.3 mm depth seat. A K type thermocouple was inserted into the sample in a 0.8 mm bore at middle height to record the temperature as a function of time. The obtained values were a good approximation of the actual average temperature of the sample. The sample temperature values were recorded three times repeated at set heights of L_2 (2 position) and L_3 (3 position), respectively. The heat flow tests were carried out with PIII layers facing to the heat jet (curves hereinafter denoted as 'c') and with opposite side of the heat jet (curves hereinafter denoted as 'a'). Reference measurements were also performed using untreated samples (curves hereinafter denoted as 'b').

3. Results and discussion

3.1. Surface characterization

According to the XPS analysis both the surface composition and the bond structures of the components are changed as a result of N PIII treatment for both polymers. Surface chemical compositions before and after treatments are given in Table 1. The compositional changes can be attributed to nitrogen incorporation into the surface layers from the plasma. It was found in earlier works that N PIII treatment resulted in the degradation of amide groups and the formation of imine, protonated amine as well as urethane-like structures [31]. A detailed discussion of XPS analysis of the modified layers including the XPS spectra has been reported elsewhere [23].

Table 1. Surface composition of the un-treated and N PIII treated PET and PA6 samples determined by XPS analysis

Sample	O [%]	N [%[	C [%]	Reference
Un-treated PET	28	0	72	[20]
N PIII treated	18	15	67	[20]
Un-treated PA6	10	7	82	[23]
N PIII treated	8	15	77	[23]

3.2. Heating tests results

Typical temperature plots are illustrated in Figure 2 (at L_3 = 20 mm, slow heating) and Figures 3 and 4 (at L_2 = 8 mm, intensive heating). During slow heating (L_3) the temperature of the sample follows a theoretical saturation curve up to ca. 60–70 seconds, i.e. section I. In this section environmental effects can be neglected. Later on time in section II heat exchange commences at the contacting interface of the insulator mask and the seat where the sample is placed, which results in an additional quasi linear temperature increase from the 'saturated' level. Temperature of curve 'a' exceed that of the reference sample even in section I (around 20–25 s on Figure 2.) due to the heat inhibiting effect of the PIII treated layer since transmission of the accumulated heat in the sample is hindered at the bottom surface. The test reveals that the heat inhibiting effect of the PIII treated layer is significant especially for setting 'c'. The role of the PIII treated layer in the heat transport can be studied with greater accuracy during rapid heating, i.e. under conditions that can be considered as quasi adiabatic. Heating tests therefore were continued for additional 60 seconds in unvar-

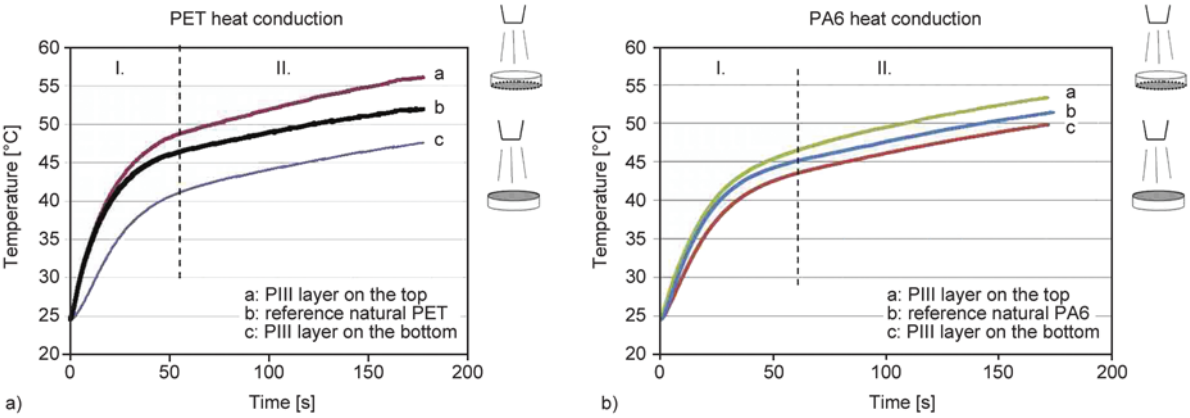

Figures 2. Temperature of sample PET (a) and PA6 (b) in the middle in slow heating conditions (L_3)

ied thermal and heat blowing conditions from distance L_2 (i.e. closer to the sample surface) (Figure 1a). The heat inhibiting effect of the PIII treated layer is even more obvious on Figure 3. that shows the intensively heated samples. When the modified layer is on top position the sample becomes warm (curve 'c') in less extent as compared to reference curve 'b' (pristine PET sample) that can be attributed to the inferior thermal conducting and reflecting properties of the modified thin layer.

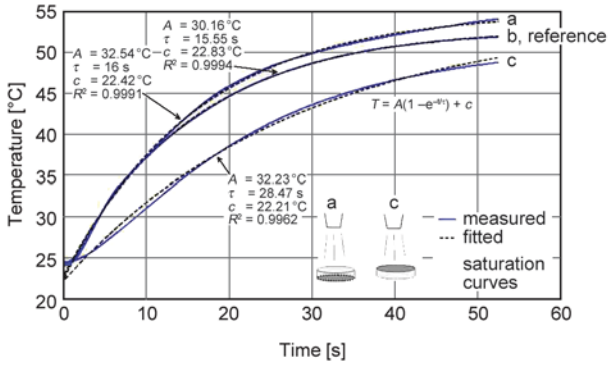

Figure 3. Temperature of sample PET in the middle under rapid heating conditions (a – distance L_1, b – distance L_2)

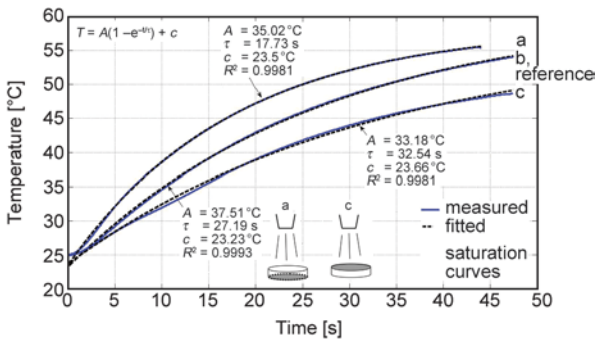

Figure 4. Temperature of sample PA6 in the middle under intensive heating conditions (from L_2 according to Figure 1b)

Comparing Figures 3 and 4 it can be concluded that intensive heating resulted in similar, although not identical, differences in the temperature history of PET and PA6. During less intensive heating with prolonged time (Figure 2a, 2b) the PIII modified thin layer on PET exhibited a higher heat inhibiting effect than that of PA6.

Heat flow induces three mechanisms in the sample: reflection, transmission and absorption. Assuming quasi adiabatic conditions transmission can be neglected, whereas the reflection being unknown is treated together with the absorption of heat hereinafter. Thus, the correct heat flow inhibiting effect of the layer can be quantified with an 'apparent thermal conductivity coefficient' that also includes reflection. There is an extensive literature on the reflection of modified polymers for solar and reflective glass technique, optics, wrapping and safety films, etc. [32]. Its proper determination, however, is rather complex and complicated as it depends on lots of parameters including the radiation spectrum, the chemical and structural composition, the substrate material, the layer thickness, etc. [33]. We used the energy and heat equations of absorption phenomena to quantify the heat flow inhibiting effect of the PIII modified layer. However, we note that heat reflection also contributes to the heat flow inhibiting effect of the PIII modified layer to a certain extent, thus heat absorption equations define an apparent linear thermal conducting coefficient.

Heat flow inhibiting phenomenon can be observed in two aspects in Figure 3. If PIII layer is at the bottom, the heat transmitted through within the polymer matrix encounters an insulating effect at the bottom that leads to temperature increase within the sample as compared to the non-treated (reference) one. The heat flow inhibiting phenomenon occurs 10–12 sec-

onds after curve 'a' exceeds reference curve 'b'. The three measurements follow the theoretical saturation function with fair correlation (Equation (1)). They differ only in their coefficient (Figure 3):

$$y = A\left(1 - \mathrm{e}^{\frac{-\mathrm{t}}{\tau}}\right) + c \tag{1}$$

where where τ is a time constant. In addition to the knowledge of the absolute temperature curves it is also vital to know the exact rate of temperature rise, the intensity of that at a given time with regard to the PIII modified and non-modified layers, which can help to judge its influence on the tribology. Derivation of fit curves on Figure 3 (Figure 5) results in the rate of temperature rise in the function of time for (Equation (2)) particular settings (a, b, c) in the form of:

$$y' = \frac{A}{\tau \mathrm{e}^{\frac{\mathrm{t}}{\tau}}} \tag{2}$$

When the heat flow reaches the surface of the matrix the rate of temperature difference is almost identical (Figure 5 reference sample 'b' and curve 'a' PIII modified layer at bottom position). Due to the inhibiting effect of the PIII modified layer at bottom position curve 'a' has a higher initial value but after 40–45 seconds the rate of difference becomes identical at the value of 0.25 °C/s. Curve 'c' clearly shows the slower warming of the sample if inhibiting layer is at top position. Temperature difference starts at a value of 60% of the reference curve 'b' but attain a little bit higher value at the end of the measurement due to the prolonged process. The figure also suggests that the heat flow inhibiting effect is more obvious for short intensive heating than for slow heating that result in more homogenous thermal conditions.

The measurements allowed the more accurate thermal analysis of the model. The temperature rise functions (Figure 3) obtained under rapid heating

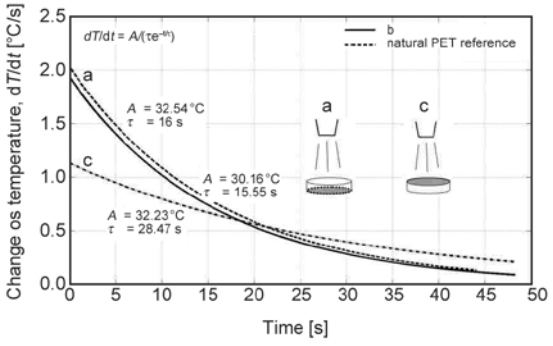

Figure 5. Rate of the temperature rise in sample PET

are the result of the heat transmission occurring at surfaces *a**, *c** and *d** on Figure 1b, whereas the effect of the surfaces *b** and *e** can be neglected. The energy-balance differential equation of the system is written as [34]:

$$\dot{E}_{\mathrm{i}}(t) - \dot{E}_0(t) = \frac{\mathrm{d}E_{\mathrm{t}}}{\mathrm{d}t} \text{ further}$$

$$c \cdot m \cdot \dot{T}(t) = Q_{\mathrm{a}*}(t) - Q_{\mathrm{c}*}(t) - Q_{\mathrm{d}*}(t) \tag{3}$$

where E_{i} stands for energy input, E_0 for energy output, E_{t} for stored energy and Q_{x} for heat (Equation (3)).

On surfaces *a** and *c** convection predominates, whereas on surface *d** conduction takes place. Differential form of Equation (3), which expresses the temperature at the middle of the sample can be written as Equation (4):

$$c \cdot m \cdot \frac{\mathrm{d}T}{\mathrm{d}t} = \kappa_{\mathrm{a}} \cdot A_{\mathrm{a}}(T_{\mathrm{S}} - T) - \kappa_{\mathrm{c}} \cdot A_{\mathrm{c}}(T - T_0) - \\ - \frac{\lambda_{\mathrm{d}}}{\delta_{\mathrm{d}}} \cdot \kappa_{\mathrm{a}} \cdot A_{\mathrm{d}}(T - T_0) \tag{4}$$

where κ_{x} – represents heat transmission of the given surface, A_{x} – represents the surface area, c – specific heat, m – mass.

With numerical integration of the equation both heat transmission of particular sample disc and the apparent linear thermal conductivity coefficient of PIII modified layer can be determined. Model calculations were carried out using code Matlab. Model identification was performed at first to non-modified PET samples. The last term at the right side of Equation (4) that represents heat transmission toward the insulating plate under the sample disc was calculated using the values of λ_{d} = 0,24 W/(m^2·K), δ_{d} = 15 mm, A_{d} = 78,5 mm^2 T_0 = 23 °C, all of which are identical to every known PA66-GF30 insulating materials. The middle term of the right side represents the free convection at the sample-air interface. The commonly used value of free convection is 20 W/(m^2·K). The surface area is A_{c} = 53.38 mm^2.

Regarding the non-treated reference sample with a virtual surface layer composed of its own substance in a thickness identical to PIII modified layer the κa heat transmission can be expressed as Equation (5):

$$\kappa_{\mathrm{a}} = \frac{1}{\frac{1}{\alpha_{\mathrm{a}}} + \frac{\delta}{\lambda_{\mathrm{PET}}}} \tag{5}$$

The virtual layer thickness of the non-treated PET (δ) is 103.6 nm (similar to PIII modified layer), whereas the linear thermal conducting coefficient (λ_{PETP}) is 0.28 W/(m·K) and the measured temperature (T_s) is 61.2 °C.

By substituting Equation (5) to Equation (4) the forced convection coefficient (α_a) as the single unknown is left that is characteristic of the surface of the sample in the experimental system. Having performed the model identification it can be concluded that the temperature rise curve of the reference PET sample (curve 'b' on Figure 3) and the calculated curve of the model show good correlation (Figure 6).

For PIII treated sample using the as-calculated convection coefficient (α_a) and the given value of κ_a (150.0665 and 150,0582 W/(m^2·K), respectively) only the apparent linear conducting coefficient of the surface layer (λ_{PIII}) is left as unknown. Performing the model calculation we obtained Figure 7 for the treated PET sample. Calculations were made in a similar manner for PA6 samples. The obtained results of the thermal model calculations are summarized in Table 2 for both polymers.

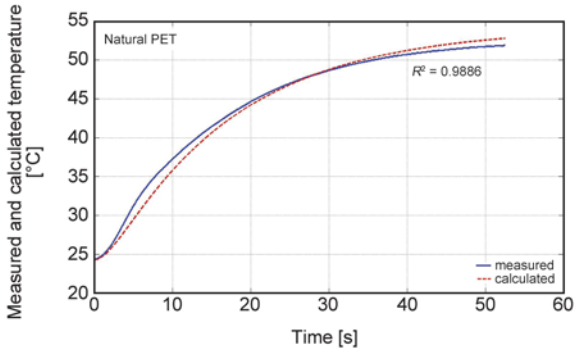

Figure 6. Measured and the calculated values of the temperature for un-treated PET sample, model identification

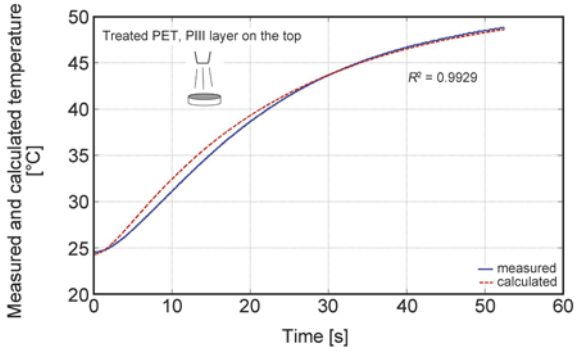

Figure 7. Measured and the calculated values of the temperature for treated PET sample

Table 2. Measured heat parameters in the model

	Heat transmission, κ [W/(m^2·K)]	Apparent linear thermal conducting coefficient, λ [W/(m·K)]
Un-treated PET	150.058	0.28
PIII treated PET Layer closer to heat jet	99.408	$3.0508 \cdot 10^{-5}$*
Un-treated PA6	160.672	0.23
PIII treated PA6 Layer closer to heat jet	115.0255	$4.4902 \cdot 10^{-5}$*

*regarding to the treated PIII layer

It can be concluded from Table 2 that the PIII modified layers reduced heat transmission by ca. 30%. We attributed this result to the several orders of magnitude lower (at least four orders in the model system) apparent linear thermal conducting coefficient of the modified layer than that of the pristine polymers. The heat flow inhibiting effect of the PIII treated surface layer occurred in both arrangements of the sample discs. On heating the sample discs, the temperature under the modified layer was lower than that in the untreated sample. In the opposite arrangement (i.e. the treated layer is at the bottom) the modified layer represented an obstacle for heat transmission toward the insulating plate.

4. Conclusions

In the present paper heat flow inhibiting properties of plasma surface modified thin layers were investigated on PET and PA6 engineering polymers. Nitrogen Plasma Immersion Ion Implantation induced considerable compositional and the microstructural changes in a depth of 110 nm of the polymers. We found that even this thin layer exhibited a significant heat flow inhibition. The modified layer resulted in a reduced heat transmission for PET and PA6 by 33 and 28%, respectively. We attribute this result to the much smaller apparent linear thermal conducting coefficient of the treated polymer. The heat flow inhibiting effect of the PIII modified surface layer prevails regardless of the position of the treated side.

Sample temperature was lower as compared to reference one if heating occurred through the modified layer, whereas in opposite arrangement, the layer hindered the heat transmission toward the contacting plate holding the heat inside the polymer. The results can be of great significance to understand the tribological performance of plasma treated polymers.

Acknowledgements
This work was supported by OTKA K 113039

References
[1] Kalácska G.: An engineering approach to dry friction behaviour of numerous engineering plastics with respect to the mechanical properties. Express Polymer Letters, **7**, 199–210 (2013).
DOI: 10.3144/expresspolymlett.2013.18
[2] Fusaro R. L.: Self-lubricating polymer composites and polymer transfer film lubrication for space applications. Tribology International, **23**, 105–122 (1990).
DOI: 10.1016/0301-679X(90)90043-O
[3] Byett J. H., Allen C.: Dry sliding wear behaviour of polyamide 66 and polycarbonate composites. Tribology International, **25**, 237–246 (1992).
DOI: 10.1016/0301-679X(92)90061-Q
[4] Kar M. K., Bahadur S.: The wear equation for unfilled and filled polyoxymethylene. Wear, **30**, 337–348 (1974).
DOI: 10.1016/0043-1648(74)90148-3
[5] Gong D., Xue Q., Wang H.: Physical models of adhesive wear of polytetrafluoroethylene and its composites. Wear, **147**, 9–24 (1991).
DOI: 10.1016/0043-1648(91)90115-B
[6] Tanaka K.: Transfer of semicrystalline polymers sliding against a smooth steel surface. Wear, **75**, 183–199 (1982).
DOI: 10.1016/0043-1648(82)90147-8
[7] Evans D. C., Senior G. S.: Self-lubricating materials for plain bearings. Tribology International, **15**, 243–248 (1982).
DOI: 10.1016/0301-679X(82)90077-9
[8] Guezmil M., Bensalah W., Mezlini S.: Effect of biolubrication on the tribological behavior of UHMWPE against M30NW stainless steel. Tribology International, **94**, 550–559 (2016).
DOI: 10.1016/j.triboint.2015.10.022
[9] Myshkin N. K., Petrokovets M. I., Kovalev A. V.: Tribology of polymers: Adhesion, friction, wear, and mass-transfer. Tribology International, **38**, 910–921 (2005).
DOI: 10.1016/j.triboint.2005.07.016
[10] Zhang S. W.: State-of-the-art of polymer tribology. Tribology International, **31**, 49–60 (1998).
DOI: 10.1016/S0301-679X(98)00007-3
[11] Nosko O., Nagamine T., Nosko A. L., Romashko A. M., Mori H., Sato Y.: Measurement of temperature at sliding polymer surface by grindable thermocouples. Tribology International, **88**, 100–106 (2015).
DOI: 10.1016/j.triboint.2015.03.015
[12] Samyn P., De Baets P., Schoukens G., Quintelier J.: Wear transitions and stability of polyoxymethylene homopolymer in highly loaded applications compared to small-scale testing. Tribology International, **40**, 819–833 (2007).
DOI: 10.1016/j.triboint.2006.08.003
[13] Samyn P., De Baets P., Schoukens G., Van Peteghem A. P.: Large-scale tests on friction and wear of engineering polymers for material selection in highly loaded sliding systems. Materials and Design, **27**, 535–555 (2006).
DOI: 10.1016/j.matdes.2004.12.021
[14] Zsidai L., Samyn P., Vercammen K., Van Acker K., Kozma M., Kalácska G., De Baets P.: Friction and thermal effects of engineering plastics sliding against steel and DLN-coated counterfaces. Tribology Letters, **17**, 269–288 (2004).
DOI: 10.1023/B:TRIL.0000032453.09366.d4
[15] Rafaja D., Wüstefeld C., Motylenko M., Schimpf C., Barsukova T., Schwarz M. R., Kroke E.: Interface phenomena in (super)hard nitride nanocomposites: From coatings to bulk materials. Chemical Society Reviews, **41**, 5081–5101 (2012).
DOI: 10.1039/C2CS15351C
[16] Pogrebnjak A. D., Pshyk A. V., Beresnev V. M., Zhollybekov B. R.: Protection of specimens against friction and wear using titanium-based multicomponent nanocomposite coatings: A review. Journal of Friction and Wear, **35**, 55–66 (2014)
DOI: 10.3103/S1068366614010073
[17] Sahasrabudhe H., Soderlind J., Bandyopadhyay A.: Laser processing of *in situ* TiN/Ti composite coating on titanium. Journal of the Mechanical Behavior of Biomedical Materials, **53**, 239–249 (2016).
DOI: 10.1016/j.jmbbm.2015.08.013
[18] Slepička P., Neděla O., Siegel J., Krajcar R., Kolská Z., Švorčik V.: Ripple polystyrene nano-pattern induced by KrF laser. Express Polymer Letters, **8**, 459–466 (2014).
DOI: 10.3144/expresspolymlett.2014.50
[19] Slepička P., Michaljaničová I., Švorčik V.: Controlled biopolymer roughness induced by plasma and excimer laser treatment. Express Polymer Letters, **7**, 950–958 (2013).
DOI: 10.3144/expresspolymlett.2013.92
[20] Sridharan K., Anders S., Nastasi M., Walter K. C., Anders A., Monteiro O. R., Ensinger W.: Nonsemiconductor applications of PIII&D. in 'Handbook of plasma immersion ion implantation and deposition' (ed.: Anders A.) Wiley-VCH, Weinheim, 553–636 (2004).
[21] Fink D.: Fundamental sof ion-irradiated polymers. Springer, Berlin (2004).
[22] Kondyurin, A., Bilek M.: Ion beamtreatment of polymers, application aspects from medicine to space. Elsevier, Amsterdam (2008).
[23] Tóth A., Kereszturi K., Mohai M., Bertóti I.: Plasma based ion implantation of engineering polymers. Surface and Coatings Technology, **204**, 2898–2908 (2010).
DOI: 10.1016/j.surfcoat.2009.12.004
[24] Kereszturi K., Tóth A., Mohai M., Bertóti I.: Surface chemical and nanomechanical alterations in plasma immersion ion implanted PET. Surface and Interface Analysis, **40**, 664–667 (2008).
DOI: 10.1002/sia.2643

[25] Kereszturi K., Tóth A., Mohai M., Bertóti I., Szépvölgyi J.: Nitrogen plasma-based ion implantation of poly (tetrafluoroethylene): Effect of the main parameters on the surface properties. Applied Surface Science, **256**, 6385–6389 (2010).
DOI: 10.1016/j.apsusc.2010.04.021

[26] Kalácska G., Zsidai L., Keresztes R., Tóth A., Mohai M., Szépvölgyi J.: Effect of nitrogen plasma immersion ion implantation of polyamide-6 on its sliding properties against steel surface. Wear, **290–291**, 66–73 (2012).
DOI: 10.1016/j.wear.2012.05.011

[27] Kalácska G., Zsidai L., Kereszturi K., Mohai M., Tóth A.: Sliding tribological properties of untreated and PIII-treated PETP. Applied Surface Science, **255**, 5847–5850 (2009).
DOI: 10.1016/j.apsusc.2009.01.017

[28] Tóth A., Bertóti I., Mohai M., Ujvári T.: Surface modification of polyethylene by nitrogen PIII: Surface chemical and nanomechanical properties. Materials Science Forum, **537–538**, 255–262 (2007).
DOI: 10.4028/www.scientific.net/MSF.537-538.255

[29] Bertóti I., Mohai M., Tóth A., Ujvári T.: Nitrogen-PBII modification of ultra-high molecular weight polyethylene: Composition, structure and nanomechanical properties. Surface and Coatings Technology, **201**, 6839–6842 (2007).
DOI: 10.1016/j.surfcoat.2006.09.022

[30] Zsidai L., Samyn P., Vercammen K., Van Acker K., Kozma M., Kalácska G., De Baets P.: Friction and thermal effects of engineering plastics sliding against steel and DLN-coated counterfaces. Tribology Letters, **17**, 269–288 (2004).
DOI: 10.1023/B:TRIL.0000032453.09366.d4

[31] Tóth A., Bertóti I., Szilágyi E., Dong H., Bell T., Juhász A., Nagy P. M.: Surface characterization of ultra-high molecular weight polyethylene after nitrogen ion implantation. Surface and Interface Analysis, **30**, 434–438 (2000).
DOI: 10.1002/1096-9918(200008)30:1<434::AID-SIA788>3.0.CO;2-W

[32] Fraidenraich N., Vilela O. C.: Exact solutions for multilayer optical structures.: Application to PV modules. Solar Energy, **69**, 357–362 (2000).
DOI: 10.1016/S0038-092X(00)00109-2

[33] Haber I. E., Farkas I.: Combining CFD simulations with blockoriented heatflow-network model for prediction of photovoltaic energy-production. Journal of Physics: Conference Series, **268**, 012008/1–012008/7 (2011).
DOI: 10.1088/1742-6596/268/1/012008

[34] Iserrmann R.: Mechatronic systems fundamentals. Springer-Verlag, London (2005).

eXPRESS Polymer Letters Vol.10, No.5 (2016) 381–393
Available online at www.expresspolymlett.com
DOI: 10.3144/expresspolymlett.2016.36

Effect of halloysite on structure and properties of melt-drawn PCL/PLA microfibrillar composites

I. Kelnar[1], J. Kratochvíl[1], I. Fortelný[1], L. Kaprálková[1], A. Zhigunov[1], V. Khunová[2], M. Nevoralová[1]*

[1]Institute of Macromolecular Chemistry, Academy of Sciences of the Czech Republic, Heyrovského nám. 2, 162 06 Praha, Czech Republic
[2]The Slovak University of Technology, Faculty of Chemical and Food Technology, Radlinského 9, 812 37 Bratislava, Slovakia

Received 30 September 2015; accepted in revised form 7 December 2015

Abstract. The study deals with the modification of mechanical properties of poly (ε-caprolactone) (PCL)/poly(lactic acid) (PLA) system using the microfibrillar composite (MFC) concept. As the *in-situ* formation of PLA fibrils by melt drawing was impossible due to flow instability during extrusion, the system was modified by adding halloysite nanotubes (HNT) using different mixing protocols. The resulting favourable effect on the rheological parameters of the components allowed successful melt drawing. Consequently, PLA fibrils formation combined with the reinforcement of components by HNT and increased PLA crystallinity lead to a biocompatible and biodegradable material with good performance suitable for a broad range of applications. The best results, comparable with analogous MFC modified with layered silicate (oMMT), have been achieved at a relatively low content of HNT of 3%, in spite of its lower reinforcing ability in a single nanocomposite. This indicates that modifying MFC by HNT, including fibrils and interface parameters, is more complex in comparison with the undrawn system.

Keywords: *mechanical properties, poly(ε-caprolactone), poly(lactic acid), microfibrillar composites, halloysite nanotubes*

1. Introduction

PCL is an important biodegradable polymer with favourable functional parameters for biomedical, packaging, and other applications [1]. In spite of its semicrystalline character and relatively high content of crystalline phase, mostly over 50%, its poorly organized crystalline structure in combination with low glass transition temperature (T_g) are the main reasons of relatively poor mechanical performance. As a result, low yield stress, stiffness, and high ductile deformation under ambient conditions limit the range of PCL applications. The purpose of numerous modifications is, in particular, higher yield stress and modulus [1]; advantageous modifications are those preserving biodegradability, for instance blending with more rigid polyesters, mostly PLA [2–5]. As a consequence, a broad range of materials with balanced and tailored mechanical performance can be obtained. The mostly applied PLLA containing 2–4% D-isomer has low compatibility with PCL [5]; therefore, various compatibilizing techniques [6, 7] must be applied. In this area, application of various nanofillers (NF) leading to simultaneous reinforcement, compatibilization, and improvement of other material parameters may also be beneficial [8–12]. Recently, halloysite nanotubes have been successfully applied to modification of PLA [13, 14] and PCL [15, 16]; their advantage is dispersion even without organophilization in these polar polymers. In some cases, suitable modifications can enhance HNT efficiency [17, 18]. However, the evaluation of the structure-directing potential of HNT in polymer

*Corresponding author, e-mail: kelnar@imc.cas.cz
© BME-PT

blends [19–23] is in its infancy stage, especially in comparison with that of oMMT [24–27].

Although the application of PLA and other high performance polyesters in the form of short reinforcing fibres [28, 29] in polymer-polymer composites could be a radical alternative to the use PCL/PLA blends, a significant limitation of this method is the difficult dispersion of compliant fibres in the polymer matrix and their relatively poor adhesion to it [30]. An advantageous method to prepare these polymer fibre-reinforced materials is the formation of microfibrillar composites [31]. This method is based on melt- or cold drawing of a polymer blend with a rigid and strong dispersed phase which should be semicrystalline with a melting point exceeding that of the matrix, e.g. the HDPE/PA6 combination [32]. In this case, subsequent processing below the melting point of the dispersed phase may lead only to isotropization of the matrix with preserved fibrils. An advantage of such short-fibre composite is efficient dispersion and bonding of *in-situ* formed reinforcement [33].

A suitable polymer pair for MFC is a combination of biodegradable linear polyesters, like the PCL/PLA blend. Friedrich *et al*. [34] and Kimble *et al.* [35] prepared PLA/ poly(glycolic acid) melt-drawn MFC for medical application. The recently reported PLA/ poly(butylene succinate) system melt-drawn with *in-situ* formed PLA short fibres could not be processed using thermoplastic processing technique due to the similarity of the components' melting points [36]. The MFC concept was also applied to PLA microfibrils preparation [37]. Some other systems of drawn fibres based on the blend of these polyesters were reported by others [38, 39]. The reason that the attractive PCL/PLA blend-based MFC has not been reported lies probably in the fact that, according to our experiments, the commercial PCL/PLA combinations cannot be successfully drawn due to unfavourable rheological parameters and thus to flow instability during extrusion, i.e. variation in the extrudate cross dimension [40]. We have successfully prepared this MFC in the case of clay addition that favourably affects extrusion stability and thus melt drawing [40]. Moreover, the nanofiller eliminates the main shortcoming of MFC, i.e. the relatively poor mechanical performance and dimensional stability due to the low mechanical parameters of polymer fibrils [41]. Our previous work indicates that the effect of NF on drawn systems is relatively complex, which may lead even to the deterioration of mechanical properties [42]. The present work deals with the modification of PCL/PLA MFC using halloysite, a nanofiller with reported high reinforcing ability and fair dispersion without modifications in polar polymers like polyesters.

2. Experimental

2.1. Materials

Poly(lactic acid) (PLA) Ingeo 2002D (Nature Works, Minnetonka, USA) with the D-isomer content of 4.3%, M_w $2.53 \cdot 10^5$ g·mol^{-1}, melt flow rate 6 g/10 min (190 °C/2.16 kg), and density 1.24 g·cm^{-3}. Poly(ε-caprolactone) (PCL) CAPA 6800 (Perstorp, Sweden) M_n $8 \cdot 10^4$ g·mol^{-1}, density 1.145 g·cm^{-3}. Halloysite nanotubes (HNT) were purchased from Sigma Aldrich (USA).

2.2. MFC preparation

Prior to mixing, PCL, PLA, and HNT were dried at 45, 85, and 70 °C, respectively, in a vacuum oven for 12 h. Mixing was carried out in a co-rotating segmented twin-screw extruder (L/D 40) Brabender TSE 20 (Brabender GmbH, Duisburg, Germany) at 400 rpm, and temperatures of the respective zones (from feeding to die) of 170, 170, 170, 170, 175, and 180 °C. The extruded bristle with the PCL/PLA 80/20 w/w composition was melt-drawn using an adjustable take-up device. The draw ratio (DR) is the ratio between the velocity of the take-up rolls and the initial velocity of the extruded bristle; DR 5 and 6 were mostly used. Besides the one-step addition of all components (with 3 phr HNT), the pre-blends of PCL with 3% HNT and PLA with 3% HNT were also used. The PCL pre-blend was mixed using temperatures 135 °C in all zones, the PLA pre-blend was mixed using temperature profile 185, 190,190, 190, 190, and 190 °C. Dog-bone specimens (gauge length 40 mm) were injected in a laboratory micro-injection moulding machine (DSM). The barrel and mould temperatures were 137 and 30 °C, respectively.

2.3. Testing

Tensile tests were carried out using an Instron 5800 (Instron, UK) apparatus at 22 °C and crosshead speed of 20 mm/min. At least eight specimens were tested for each sample. Young's modulus (E), maximum stress (σ_m), and elongation at break (ε_b) were evaluated; the corresponding variation coefficients did not exceed 10, 2 and 20%, respectively.

Tensile impact strength, a_t, was measured on one-side notched specimens using a CEAST Resil impact junior hammer (CEAST S.p.A., Torino, Italy) with an energy of 4 J (variation coefficient 10–15%). The reported values are averages of twelve individual measurements. Dynamic mechanical analysis (DMA) was performed in single-cantilever mode using a DMA DX04T (RMI, Pardubice, Czech Republic) apparatus at 1 Hz and heating rate of 1 °C/min from –120 to 250 °C.

The differential scanning calorimetry (DSC) analysis was carried out using a Perkin-Elmer 8500 DSC (Perkin Elmer, Waltham, MA, USA) apparatus. Samples of 5–10 mg were heated from 0 to 200 °C at the heating rate of 10 °C/min. The melting temperature T_m was identified as the melting endotherm maximum. The crystallinity was calculated from the respective peak areas using the Perkin-Elmer software and the values 139.5 and 93.1 J/g for the heat of melting of 100%-crystalline PCL and PLA, respectively.

2.4. Characterization of structure

The structure of drawn and undrawn samples was examined using scanning electron microscopy (SEM) with a Quanta 200 FEG (FEI, Czech republic) microscope. The injection-moulded specimens of the undrawn blends were broken under liquid nitrogen. Because of impossibility of the separation of PLA fibrils due to chemical similarity of both polyesters, the drawn bristle samples were broken under liquid nitrogen in parallel direction with respect to their long axis. The PLA phase was etched using 20% NaOH at room temperature for 30 min.The size of the dispersed PLA particles was investigated by a MINI MOP image analyzer (Kontron Co., Germany). At least 200 particles were evaluated in each sample. For the transmission electron microscope Tecnai G2 Spirit (FEI, Czech republic) observations, ultrathin (60 nm) sections were prepared under liquid nitrogen using an Ultracut UCT (Leica Mikrosysteme GmbH, Austria) ultramicrotome.

Wide-angle X-ray Scattering (WAXS) and Small-angle X-ray scattering (SAXS) experiments were performed using a pinhole camera (Molecular Metrology System, Rigaku, Japan) attached to a microfocused X-ray beam generator (Osmic MicroMax 002, Rigaku) operating at 45 kV and 0.66 mA (30 W). The camera was equipped with an interchangeable Imaging Plate 23×25 cm (Fujifilm). For WAXS, the sample-to-detector distance was approximately 24 cm and experimental setup covered the momentum transfer (q) range of 0.4–3.5 Å^{-1}. While $q = (4\pi/\lambda)\sin\theta$, where $\lambda = 1.54$ Å is the wavelength and 2θ is the scattering angle. Calibrations of the centre and sample-to-detector distance were made using Si powder. To cover the SAXS range, the sample-to-detector distance was set to 390 cm. Covered q-range was 0.008–0.26 Å^{-1}. Calibrations of the centre and sample-to-detector distance were made using Ag-behenate. For both WAXS and SAXS, one-dimensional intensity profiles $I(q)$ were circularly averaged from the two-dimensional scattering patterns. The data were deconvoluted into peaks using Fityk (A curve fitting and data analyzing program) [43].

Crystallinity was determined by the division of the area of crystal peaks by the total area. Crystal molecular orientation was determined by azimuthal integration of the strongest (110) reflection.

2.5. Rheological characterization

Rheological characterization was conducted using an ARES apparatus (Rheometric Scientific, Piscataway, NJ) with the parallel-plate geometry at 137 and 170 °C using an oscillatory shear deformation at frequency range 0.1–100 rad/s. The amplitude of oscillation was 3%, i.e. within the range of linear viscoelasticity of all studied materials.

3. Results and discussion

3.1. Effect of HNT on structure of undrawn blend and related MFC

Figure 1 and Table 1 show a slight reduction of the size of PLA inclusions in the PCL/PLA blend from ~0.9 μm in the HNT-free blend to ~0.5 μm with 5% HNT addition. This corresponds to well-known structure-directing effect of nanofillers, but the 'compatibilizing' effect is less marked in comparison with layered silicates [40]; more marked decrease in particle size occurs with relatively high 5% HNT content. In addition to reduced average diameter, the structure is more polydisperse (Figure 1b). Crucial role of HNT consists mainly in the improvement of extrusion stability as a result of a change in the rheological parameters (see below), which allows melt drawing of the extruded bristle and thus *in-situ* formation of the PLA fibrils. The structure and approximate dimensions of fibrils are obvious from Figure 2, the aspect ratio (AR) is ~12. Due to the comparable diameter of fibrils and dispersed particles in

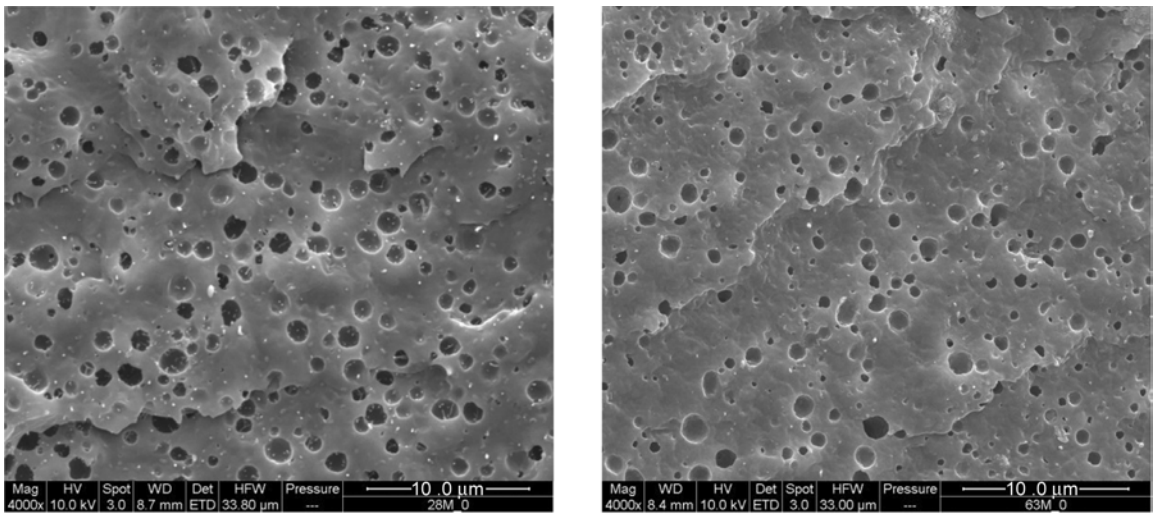

a) b)

Figure 1. SEM images of a) undrawn injection moulded PCL/PLA 80/20 system; b) undrawn injection moulded PCL/PLA/HNT 80/20/3 blend (one-step prepared)

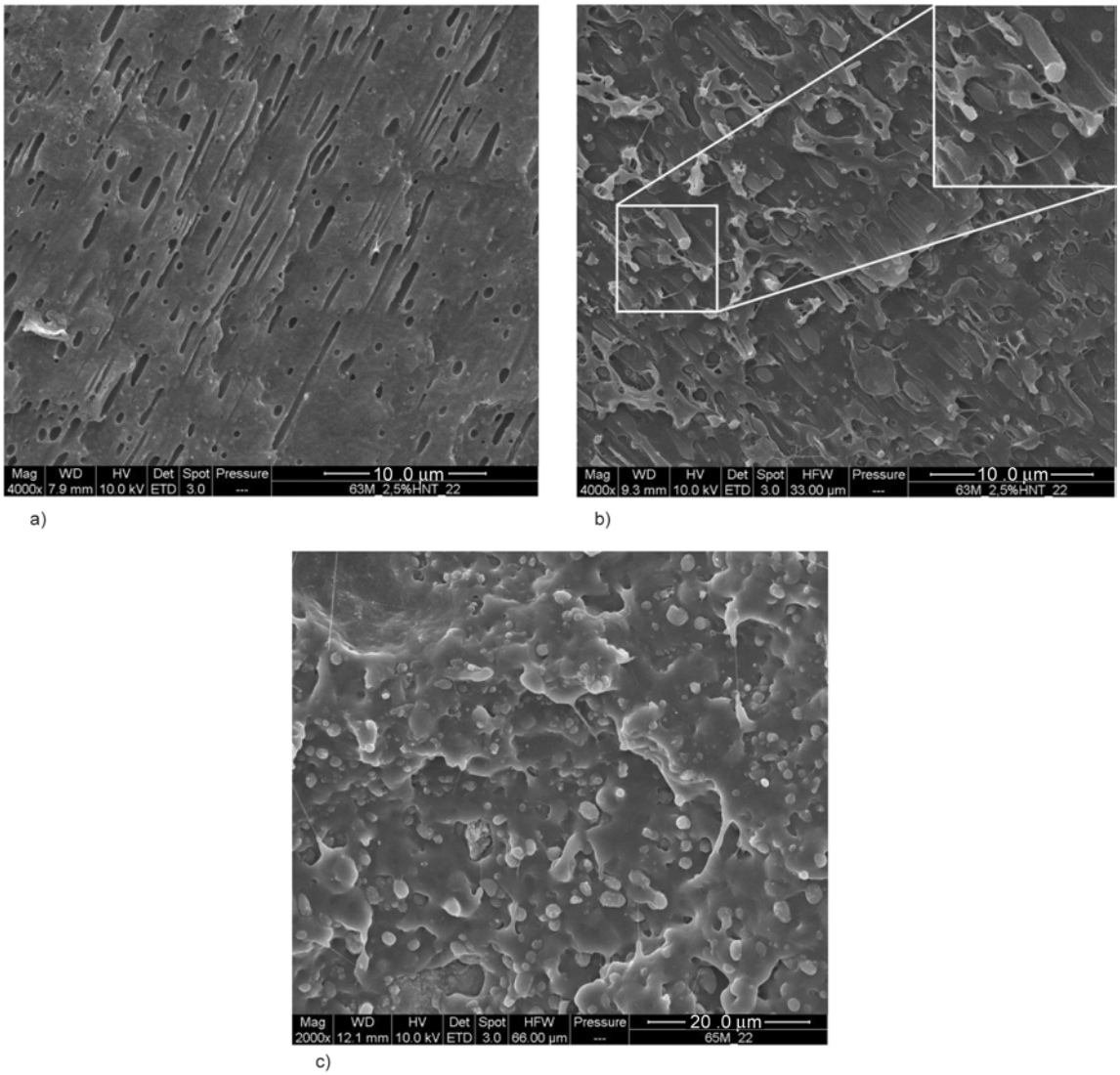

a) b)

c)

Figure 2. SEM images of a) etched and b) unetched melt drawn bristle (sample broken parallel to draw direction) of PCL/PLA/HNT 80/20/3 system (draw ratio = 6); c) fracture surface of the same injection moulded MFC sample

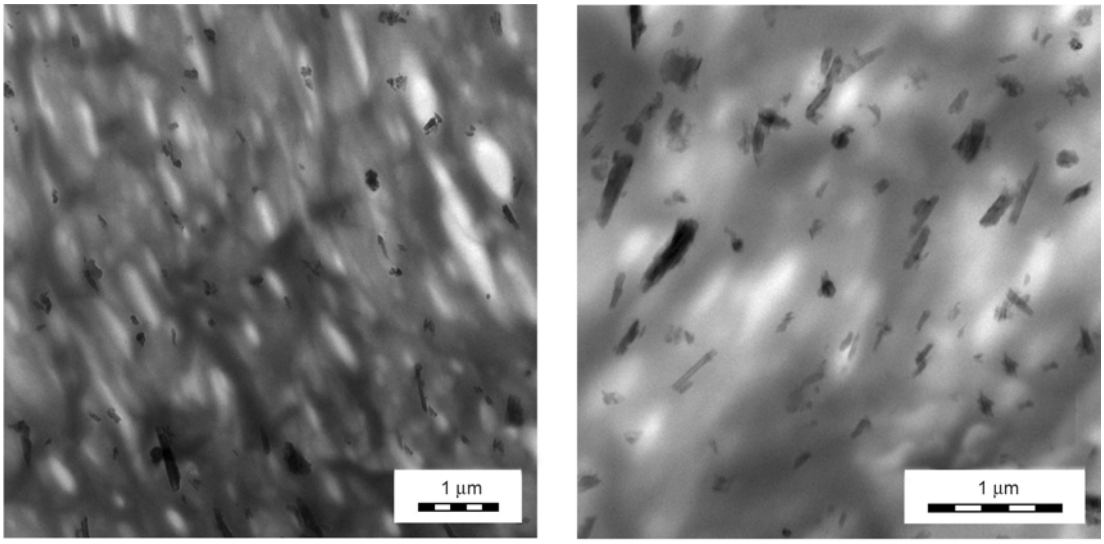

Figure 3. TEM of melt-drawn bristle, sample microtomed parallel to draw direction a) PCL/PLA/HNT 80/20/3, b) another place, higher magnification

Table 1. Effect of HNT on PLA inclusion size, one-step prepared samples

Composition Parts by wt.	Particle diameter [µm] Undrawn sample	Fibril diameter [µm] Draw ratio 6
PCL/PLA 80/20	0.90	–
PCL/PLA/HNT 80/20/3	0.83	0.57
PCL/PLA/HNT 80/20/5	0.50	0.51

the undrawn blend (Table 1) and thus much larger volume of fibrils, significant coalescence of PLA inclusions takes place in the course of melt drawing, in agreement with other works [44, 45]. As it is impossible to prepare HNT-free MFC, we cannot consider the possible effect of the nanofiller on coalescence, as found in clay-containing MFC based on the HDPE/PA6 combination [42]. From Figures 2 it is also apparent that diameters of the PLA fibrils in the drawn bristle and injection moulded sample are comparable. TEM images in Figure 3 show light PLA fibrils in a dark grey PCL matrix. Black HNT and their aggregates are localized predominantly in the PCL matrix and at the interface. This structure was achieved mainly in the case of simultaneous addition of all components, which leads to the most efficient drawing. In the case of other mixing protocols, pre-blending of HNT in the PLA component did not lead to successful drawing, similarly to analogous clay-containing system [40]; whereas only limited drawing is different from clay-modified MFC in the case of pre-blending of HNT with PCL. In both cases, successful drawing is possible with further simultaneous addition of HNT. As final HNT localization is similar in all the mentioned drawn systems, important factor influencing fibrils formation is HNT migration between components in the course of extrusion and drawing [42]. We suppose initial localization in the earlier melting PCL with subsequent migration to later melting PLA. This may lead to higher interfacial HNT localization in the course of drawing, which may affect attractive forces between coalescing particles [46].

3.2. Dynamic mechanical analysis (DMA)

Temperature dependence of loss modulus indicates negligible increase of glass transition temperature (T_g) of single PCL (~1.5 °C, Figure 4a) and PLA (~2 °C, Figure 4b) due to the presence of 3% HNT. This is probably a result of compensation of two effects – usual increase in T_g by added nanofillers, as frequently mentioned in the literature [47], and higher chain mobility caused by increased free volume in the case of anisotropic nanofillers with length exceeding the typical gyration radii of polymer chains [48, 49].

In the PCL/PLA/HNT undrawn blend (Figure 4c), the negligible changes in T_g (~2 °C increase of PCL and ~1 °C decrease for PLA) confirm practically no impact on compatibility in accordance with very low 'compatibilizing' effect of HNT (Figure 1, Table 1) From Figure 4c it is further obvious that drawing practically does not affect T_g of the PCL matrix in the analogous MFC system, whereas slightly higher T_g of PLA fibrils undoubtedly caused by drawing was found [42].

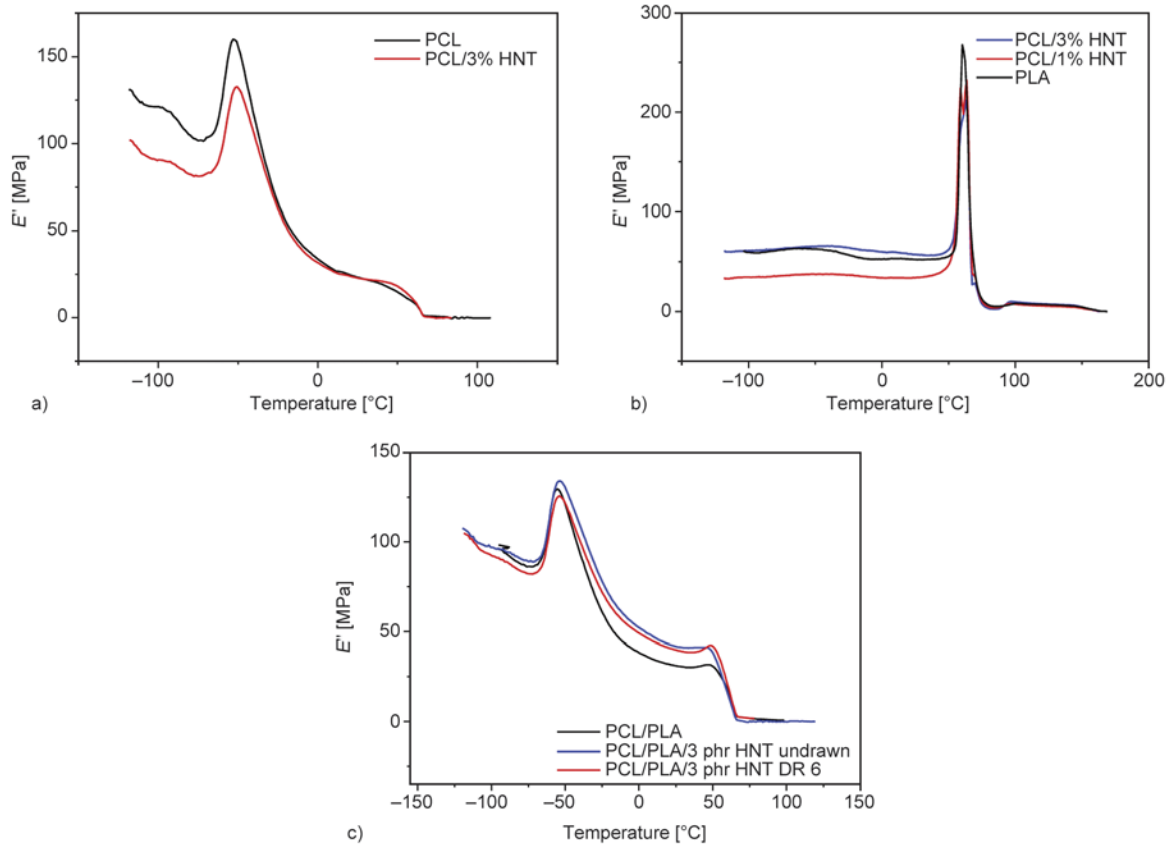

Figure 4. Temperature dependence of loss modulus a) PCL/HNT, b) PLA/HNT, c) PCL/PLA/HNT

3.3. Effect of HNT and drawing on crystallinity

WAXS-SAXS analysis

Figure 5 shows the typical two-dimensional WAXS pattern. The brightest circle corresponds to (110) PCL peak, but the behaviour is anisotropic. In order to check the degree of orientation, azimuthal integration of this peak was made (Figure 6). The peaks widths of normalized intensity are the same, which indicates that certain PCL matrix orientation is similar in all samples. This means that PCL crystalline structure is not affected by the PLA fibrils.

All the diffractograms in Figure 7 are similar with the same peaks positions and intensities. One minor deviation can be observed for the PLA (200) peak. It seems that the incorporation of higher content (5%) of halloysite reduces PLA crystallinity. This makes very small impact on overall crystallinity which is around 51%.

In Figure 8, one can see formed PCL lamellar stacks as a peak at q = 0.04 Å^{-1} [50]. For the scattering

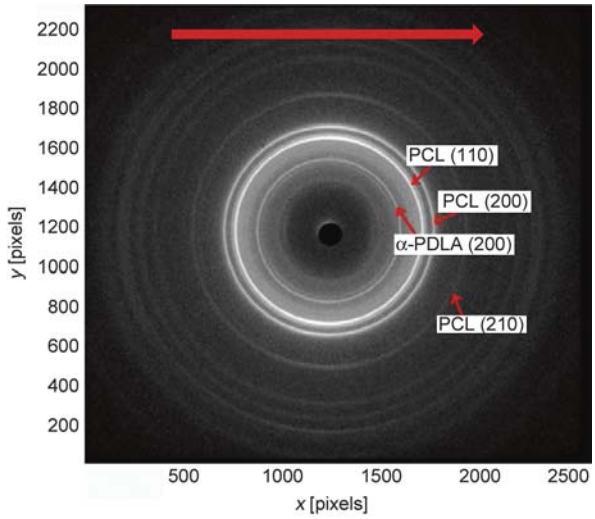

Figure 5. 2D WAXS for the undrawn PCL/PLA sample 80/20. Arrow showing the flow (injection moulding) direction.

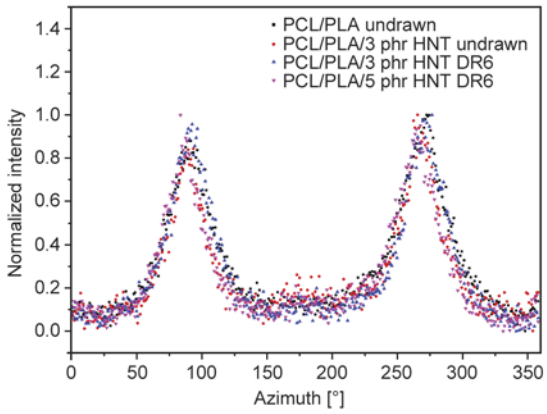

Figure 6. Azimuthal averaging of PCL (110) peak

curves corresponding to PCL/PLA with halloysite, the intensity falls with the slope $q^{-1.8}$ at lower angles. This is in agreement with tubular structure of HNT [51]. For these samples, the lamellar peak is overlapped by strong signal corresponding to halloysite. The presence of small bump at q = 0.021 Å^{-1} is given by the diameter of halloysite (~300 Å^{-1}). Small changes at higher q-values are given by the degree of tubes filling. With higher amount of HNT, the average amount of material inside the tubes is lower, which lowers the overall intensity. For the drawn sample PCL/PLA/HNT 80/20/3, the drawing increases intensity, which indicates possible higher incorporation of polymer into the lumen of halloysite tubes.

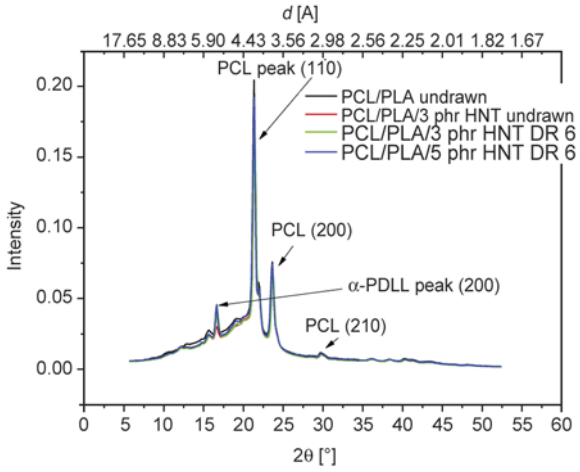

Figure 7. Effect of HNT and drawing on diffractograms

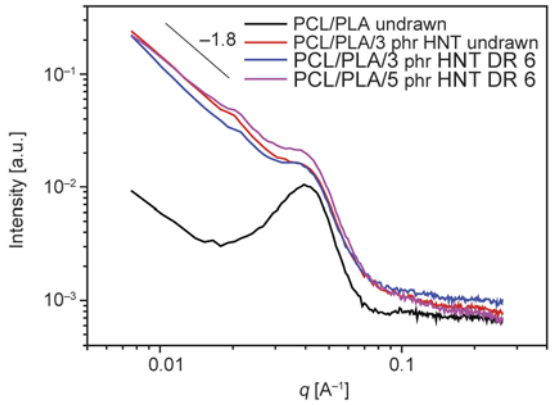

Figure 8. One-dimensional SAXS patterns

Differential scanning calorimetry

Typical DSC thermogram of the studied PCL/PLA/HNT 80/20/3 system is shown in Figure 9. PCL and PLA show maximum of the melting endotherm at about 62 and 151 °C, respectively. The glass transition temperature of PLA (about 61 °C) is hidden under the PCL endotherm. A flat exotherm appears between the two melting endotherms. It belongs to cold crystallization of PLA that crystallizes after crossing T_g. This exotherm provides the value CR_c in Table 2 that should be subtracted from the total crystallinity CR_m to receive PLA crystallinity of the as-prepared samples CR_p.

Table 2 shows that melting temperatures (i.e. measures of crystal perfection) of both PCL and PLA do not show any significant dependence either on added filler, drawing or processing temperature. This finding corresponds to the WAXS observations. Neat

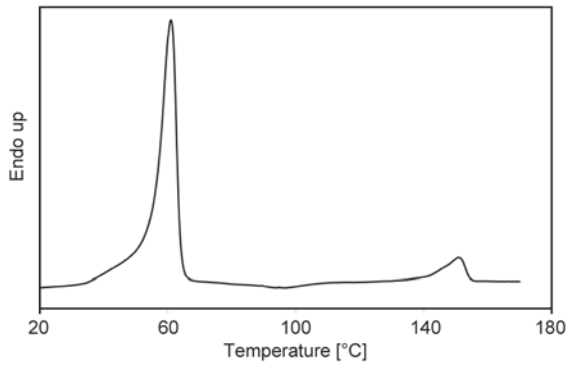

Figure 9. DSC thermogram of PCL/PLA/HNT 80/20/3

Table 2. DSC results of PCL, PLA, their blends (80/20) and microfibrillar composites. Melting temperature T_m, crystallinity CR. For CR of PLA the subscripts mean: c – cold crystallization, m – final melting, p – as-prepared

Sample	DR	Process temperature [°C]	PCL		PLA			
			T_m [°C]	CR [%]	CR_c [%]	T_m [°C]	CR_m [%]	CR_p [%]
PCL	1	137	63.2	53.6	–	–	–	–
PLA	1	190	–	–	6.5	151.1	8.1	1.6
PLA, 70°C, 60 min	1	190	–	–	0.5	151.7	29.3	28.8
PLA 1% HNT, 70 °C, 60 min	1	190	–	–	0.5	154.4	32.7	32.2
PCL/PLA 80/20	1	137	62.8	52.0	5.8	150.7	32.6	26.8
PCL/PLA/HNT 80/20/3	1	137	63.5	48.8	9.1	152.3	40.7	31.6
PCL/PLA/HNT 80/20/3	6	137	62.8	51.3	5.6	151.3	40.2	35.9
PCL/PLA/HNT 80/20/5	6	137	61.5	48.2	1.5	149.5	20.3	18.8
PCL/PLA/HNT 80/20/3	1	200	61.0	51.4	18.9	150.9	34.9	16.0
PCL/PLA/HNT 80/20/3	6	200	60.6	47.9	20.0	151.6	34.0	14.0

PLA is almost amorphous as demonstrated by the very low value (1.6 phr) of CR_p. However, its crystallinity dramatically increases on blending with PCL [4] and subsequent annealing of the samples during the process of injection moulding at 137 °C for ~4 min accompanied by PLA cold crystallization. Optimum filler concentration seems to be 3 phr. Another increase in PLA crystallinity to ~36% is achieved by MFC formation by drawing, probably as a consequence of chain orientation in the fibrils. Higher filler concentration (5 phr) leads to lower crystallinity in accordance with the WAXS results. It seems that in this case hindering effect of the filler takes place, which leads to limited growth of spherulites. At high processing temperature (200 °C), the PLA phase including fibrils melts, which has a negative effect on PLA crystallinity. This documents the importance of PLA annealing below its melting point. This effect is particularly apparent for the samples of neat PLA and the PLA/HNT composite annealed at 70 °C. In both cases, the as-prepared samples show high crystallinity CR_p of about 30% and negligible cold crystallization.

3.4. Effect of HNT and drawing on mechanical properties

The data are summarized in Table 3. Blending (PCL/PLA 80/20) results in increased yield stress σ_y and modulus E in comparison with the PCL matrix. On the other hand, unchanged σ_m and significantly reduced ε_b and at indicate reduced ductility of PCL by addition of rigid PLA. These trends are more intensive on addition of HNT – small increase in yield stress and modulus is accompanied by significantly reduced strain hardening, as also shown in Figure 10.

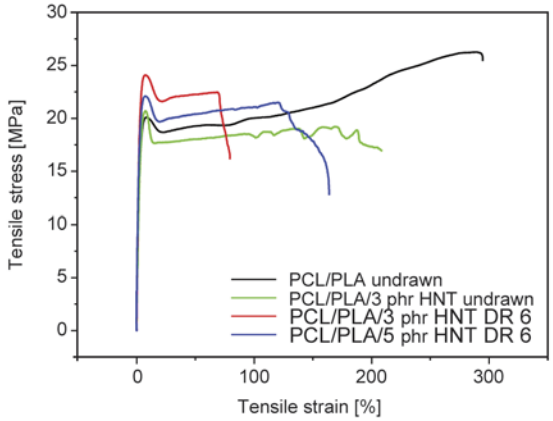

Figure 10. Stress-strain curves of PCL/PLA 80/20 blend and related MFC containing HNT

The best mechanical behaviour, i.e. particularly yield stress and modulus, was found for the one-step prepared PCL/PLA 80/20 sample with 3 phr HNT drawn at DR = 6. This corresponds to the fibril formation only possible after the modification of the PCL/PLA system by HNT (see above). The fair mechanical performance of this biodegradable PCL-based material (MFC) is predominantly a consequence of the dual reinforcement by PLA fibrils of AR ~12 and HNT. In addition, the increase in PLA crystallinity to about 30% as a result of 'annealing' in the course of sample injection moulding at 137°C (see Table 2) leading to improvement of mechanical parameters of the PLA component is also important (Table 3). This was confirmed by testing neat PLA and PLA + 1% HNT prepared by injection mould-

Table 3. Mechanical properties of components, PCL/PLA 80/20 blend, and MFC in dependence on HNT content. Pre-blended components are in brackets.

Sample composition	DR	σ_y [MPa]	σ_m [MPa]	ε_y [%]	ε_b [%]	E [MPa]	[kJ/m^2]
PCL	1	16.10	27.00	9.4	472.00	310	85.4
PCL 3% HNT	1	15.90	31.70	8.6	705.00	420	59.0
PLA	1	68.00	68.00	2.7	4.30	3155	18.9
PLA 1% HNT	1	66.80	58.00	2.3	4.00	3310	–
PLA 3% HNT	1	62.70	53.00	2.0	6.00	3480	24.2
PLA 70 °C[a]	1	69.70	69.70	3.1	4.05	3860	–
PLA 1% HNT 70 °C[a]	1	68.20	54.00	4.6	4.60	4155	–
PCL/PLA 80/20	1	20.20	26.80	7.6	295.00	720	60.8
PCL/PLA/HNT 80/20/3	1	20.80	20.80	7.8	201.00	795	34.0
PCL/PLA/HNT 80/20/3	6	23.85	23.85	7.1	83.00	985	38.6
PCL/PLA/HNT 80/20/5	6	22.00	22.40	7.6	143.00	945	49.7
(PCL+3% HNT)[b]/PLA 80/20	5	21.40	27.00	9.7	374.00	905	–
PCL/(PLA+3% HNT)[c]/HNT 80/20/3	1	20.90	14.00	8.1	548.00	820	35.2
PCL/(PLA+3% HNT)[c]/HNT 80/20/3	5	22.60	12.60	7.6	120.00	935	45.4

[a]annealed 60 min at 70 °C, [b]pre-blend PLA/1% C15, [c]pre-blend PCL/3% C15

ing at 190 °C and subsequent annealing at 70 °C for 1 h. These samples show crystallinities of about 30% (Table 2) and approximate 20% increase in modulus (Table 3).

Surprisingly, increasing the HNT content from 3 to 5 phr in MFC results in reduced yield strength and modulus whereas toughness and elongation are higher, which is quite an unusual result. This can be partially attributed to the lower crystallinity of PLA in MFC with 5 phr HNT (see Table 2), but predominantly to the complex effect of HNT, including changes in the interface [52]. Such effect was also found in the analogous oMMT-modified systems [40].

Table 3 also shows that pre-blending of HNT in PCL is less effective in comparison with the one-step preparation, contrary to the analogous clay–modified system [40]. Reduction in yield stress and modulus is accompanied by more significant strain hardening.

The application of PLA/HNT pre-blend does not lead to MFC formation due to the impossibility of drawing. Drawing is enabled by the simultaneous addition of 3 phr HNT, similarly to the oMMT-modified system [40]. The importance of the mixing protocol also indicates crucial role of the nanofiller transfer between the polymer components in the course of drawing [42]. This may lead to changed HNT arrangement and its localization in the interfacial area. This could change crystallinity and thus parameters of the interface that would result in modified properties of the whole system [52].

Undoubtedly, mechanical properties can also be affected by HNT localization in the respective polymer phases and is related to different degrees of their reinforcement. TEM observations (Figure 3) show relatively low content of HNT inside PLA and its more significant localization in PCL. Unfortunately, exact content of HNT in the respective components cannot be determined as their separation is impossible. Regarding the effect of HNT localization on mechanical behaviour, it is apparent that its increased content in one component at the expense of the other may affect properties due to uneven ratio of the components.

An example is a model PCL/PLA 80/20 system with 1% HNT in the PLA phase and 3% HNT in PCL. For the 0.25% increase of HNT in PCL by transfer of 1% from PLA (and resulting in changes of E, assuming linear dependence of E on HNT content) and the opposite case of similar transfer of 0.25% from PCL to PLA, the Halpin-Tsai model [53] shows difference in E between both cases of ~30 MPa only. This implies that HNT reinforcement of the system is particularly important, whereas its localization in the respective polymer phases has relatively low impact.

The properties of HNT-modified MFCs are comparable and some of their parameters even exceed those of the analogous oMMT-modified system (of similar AR of fibrils) [40]. The fact that such behaviour has been found in spite of the lower reinforcing effect of HNT on the neat components in comparison with oMMT also confirms the complex effect of both nanofillers.

Significant difference from oMMT-modified MFC is very low strain hardening or its practical absence in HNT-containing MFC shown in Table 3 and Figure 10. This tensile behaviour occurs already in the undrawn HNT-containing sample probably as a consequence of the above mentioned increased PLA crystallinity caused by annealing during injection moulding below the melting point of PLA. In the drawn system, the post-yield drawing is suppressed more markedly by the presence of the PLA fibrils. Moreover, this occurs in spite of similar extent of elongation (ε_b) of both MFCs. Such behaviour is also significantly different from that of the PCL/HNT and undrawn PCL/PLA systems (Table 3), where stress at break exceeds the value of 30 and 27 MPa, respectively.

3.5. Effect of HNT on rheology of components and MFC

As mentioned above, TEM (Figure 3) indicates the localization of HNT in the PCL and PLA phases and at the interface, with predominant occurrence in the PCL matrix. The presence of HNT leads to remarkable increase in viscosity of PCL, PLA, and the PCL/PLA blend (see Figure 11). The changed rheological behaviour, including the effect of orientation of anisotropic HNT at higher shear rates, is apparently responsible for increased stability of extrusion rendering the cold drawing possible. The difference in rheological properties of the drawn and undrawn PCL/PLA/HNT nanocomposites (see Figure 12), measured at 137 °C to avoid melting of the PLA fibrils, can be explained as a consequence of presence of the PLA fibrils in the first system in comparison with spherical inclusions in the other. It can be assumed that the orientation of the PLA

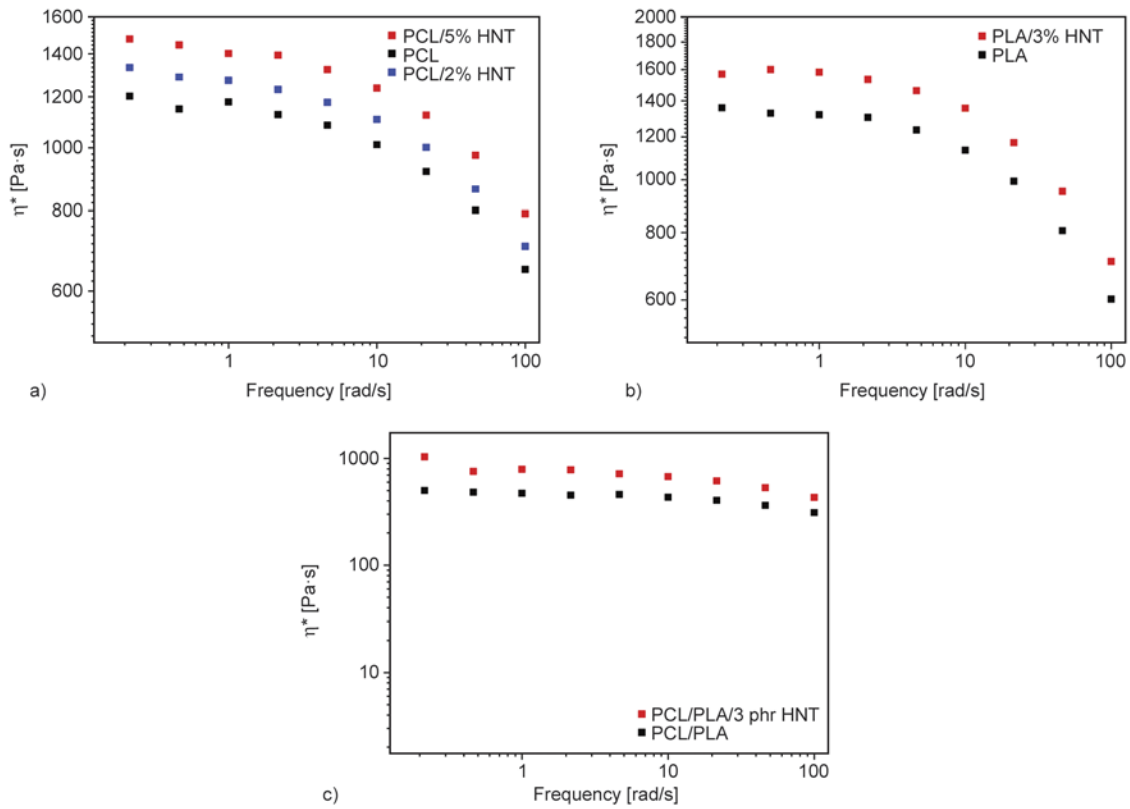

Figure 11. Effect of HNT addition on complex viscosity of a) PCL, b) PLA, c) PCL/PLA 80/20 system at 170 °C

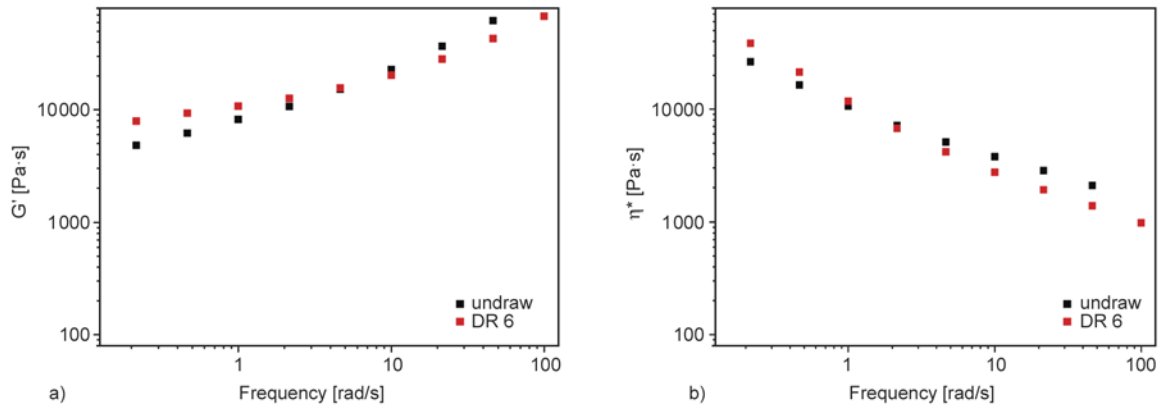

Figure 12. Effect of HNT addition on a) storage modulus and b) complex viscosity of undrawn and melt drawn PCL/PLA/HNT 80/20/3 systems at 137 °C

fibres disappears to a large extent during preparation of the specimens for rheological measurements and melting of the PCL matrix before start of the measurements.

For a certain volume fraction of dispersed particles, percolation threshold in the system and distance between a particle and its nearest neighbour decrease with increasing particle anisometry. Therefore, stronger interactions can be assumed for a system with more anisometric particles which increase viscosity and storage modulus of the system measured at low frequencies. On the other hand, more anisometric particles are more easily oriented in flow, which explains faster decrease in viscosity and storage modulus with increasing angular frequency. In other words, the rheological behaviour of MFC is typical of short fibre composites [54]. At the same time, the rather small difference in η* and *G* between undrawn blend and MFC is a result of certain presence of apparently anisometric PLA particles caused by flow in the extruder die [42].

4. Conclusions

The results obtained indicate a complex effect of HNT on the behaviour of the PCL /PLA microfibrillar composite. This is mainly reflected by the modification of the rheological parameters of the polymer components leading to stable extrusion and thus melt drawing which is impossible in the HNT-free blend. Although further important effect of HNT is reinforcement of the polymer components, the best performance with low 3 phr HNT content indicates important role of HNT-induced effects on, e.g., interface and fibrils parameters affecting deformational behaviour. The final MFC processing below the melting point of PLA leads to favourable increase in crystallinity of nearly amorphous neat PLA and enhanced mechanical performance. As a result, the material with the biodegradable PCL matrix of significantly improved mechanical behaviour is obtained.

Acknowledgements

This work was supported by Czech Science Foundation (Grant No 13-15255S).

References

[1] Woodruff M. A., Hutmacher D. W.: The return of a forgotten polymer – Polycaprolactone in the 21st century. Progress in Polymer Science, **35**, 1217–11256 (2010). DOI: 10.1016/j.progpolymsci.2010.04.002

[2] Simões C. L., Viana J. C., Cunha A. M.: Mechanical properties of poly(ε-caprolactone) and poly(lactic acid) blends. Journal of Applied Polymer Science, **112**, 345–352 (2009). DOI: 10.1002/app.29425

[3] Yeh J-T., Wu C-J., Tsou C-H., Chai W-L., Chow J-D., Huang C-J., Chen K-N., Wu C-S.: Study on the crystallization, miscibility, morphology, properties of poly(lactic acid)/poly(ε-caprolactone) blends. Polymer-Plastics Technology and Engineering, **48**, 571–578 (2009). DOI: 10.1080/03602550902824390

[4] Urquijo J., Guerrica-Echevarría G., Eguiazábal J. I.: Melt processed PLA/PCL blends: Effect of processing method on phase structure, morphology, and mechanical properties. Journal of Applied Polymer Science, **132**, 42641/1–42641/9 (2015). DOI: 10.1002/app.42641

[5] López-Rodríguez N., López-Arraiza A., Meaurio E., Sarasua J. R.: Crystallization, morphology, and mechanical behavior of polylactide/poly(ε-caprolactone) blends. Polymer Engineering and Science, **46**, 1299–1308 (2006). DOI: 10.1002/pen.20609

[6] Na Y-H., He Y., Shuai X., Kikkawa Y., Doi Y., Inoue Y.: Compatibilization effect of poly(ε-caprolactone)-*b*-poly(ethylene glycol) block copolymers and phase morphology analysis in immiscible poly(lactide)/poly (ε-caprolactone) blends. Biomacromolecules, **3**, 1179–1186 (2002). DOI: 10.1021/bm020050r

[7] Tuba F., Oláh L., Nagy P.: Characterization of reactively compatibilized poly(D,L-lactide)/poly(ε-caprolactone) biodegradable blends by essential work of fracture method. Engineering Fracture Mechanics, **78**, 3123–3133 (2011). DOI: 10.1016/j.engfracmech.2011.09.010

[8] Jain S., Reddy M. M., Mohanty A. K., Misra M., Ghosh A. K.: A new biodegradable flexible composite sheet from poly(lactic acid)/poly(ε-caprolactone) blends and micro-talc. Macromolecular Materials and Engineering, **295**, 750–762 (2010). DOI: 10.1002/mame.201000063

[9] Wu D., Lin D., Zhang J., Zhou W., Zhang M., Zhang Y., Wang D., Lin B.: Selective localization of nanofillers: Effect on morphology and crystallization of PLA/PCL blends. Macromolecular Chemistry and Physics, **212**, 613–626 (2011). DOI: 10.1002/macp.201000579

[10] Hasook A., Tanoue S., Iemoto Y., Unryu T.: Characterization and mechanical properties of poly(lactic acid)/poly(ε-caprolactone)/organoclay nanocomposites prepared by melt compounding. Polymer Engineering and Science, **46**, 1001–1007 (2006). DOI: 10.1002/pen.20579

[11] Li Q., Yoon J-S., Chen G-X.: Thermal and biodegradable properties of poly(L-lactide)/poly(ε-caprolactone) compounded with functionalized organoclay. Journal of Polymers and the Environment, **19**, 59–68 (2011). DOI: 10.1007/s10924-010-0256-2

[12] Goffin A-L., Habibi Y., Raquez J-M., Dubois P.: Polyester-grafted cellulose nanowhiskers: A new approach for tuning the microstructure of immiscible polyester blends. ACS Applied Materials and Interfaces, **4**, 3364–3371 (2012). DOI: 10.1021/am3008196

[13] Kaygusuz I., Kaynak C.: Influences of halloysite nanotubes on crystallisation behaviour of polylactide. Plastics, Rubber and Composites, Macromolecular Engineering, **44**, 41–49 (2015). DOI: 10.1179/1743289814Y.0000000116

[14] Liu M., Zhang Y., Zhou C.: Nanocomposites of halloysite and polylactide. Applied Clay Science, **75–76**, 52–59 (2013). DOI: 10.1016/j.clay.2013.02.019

[15] Lee K-S., Chang Y-W.: Thermal, mechanical, and rheological properties of poly(ε-caprolactone)/halloysite nanotube nanocomposites. Journal of Applied Polymer Science, **128**, 2807–2816 (2013). DOI: 10.1002/app.38457

[16] Khunová V., Kelnar I., Kristóf J., Dybal J., Kratochvíl J., Kaprálková L.: The effect of urea and urea-modified halloysite on performance of PCL. Journal of Thermal Analysis and Calorimetry, **120**, 1283–1291 (2015). DOI: 10.1007/s10973-015-4448-9

[17] Pasbakhsh P., Ismail H., Ahmad Fauzi M. N., Abu Bakar A.: EPDM/modified halloysite nanocomposites. Applied Clay Science, **48**, 405–413 (2010). DOI: 10.1016/j.clay.2010.01.015

[18] Khunova V., Kristóf J., Kelnar I., Dybal J.: The effect of halloysite modification combined with *in situ* matrix modifications on the structure and properties of polypropylene/halloysite nanocomposites. Express Polymer Letters, **7**, 471–479 (2013). DOI: 10.3144/expresspolymlett.2013.43

[19] Pal P., Kundu M. K., Kalra S., Das C. K.: Mechanical and crystalline behavior of polymeric nanocomposites in presence of natural clay. Open Journal of Applied Sciences, **2**, 277–282 (2012). DOI: 10.4236/ojapps.2012.24041

[20] Poikelispää M., Das A., Dierkes W., Vuorinen J.: Synergistic effect of plasma-modified halloysite nanotubes and carbon black in natural rubber–butadiene rubber blend. Journal of Applied Polymer Science, **127**, 4688–4696 (2013). DOI: 10.1002/app.38080

[21] Pal P., Kundu M. K., Malas A., Das C.: Compatibilizing effect of halloysite nanotubes in polar–nonpolar hybrid system. Journal of Applied Polymer Science, **131**, 39587/1–39587/7 (2014). DOI: 10.1002/app.39587

[22] Russo P., Vetrano B., Acierno D., Mauro M.: Thermal and structural characterization of biodegradable blends filled with halloysite nanotubes. Polymer Composites, **34**, 1460–1470 (2013). DOI: 10.1002/pc.22419

[23] Tham W. L., Mohd Ishak Z. A., Chow W. S.: Mechanical and thermal properties enhancement of poly(lactic acid)/halloysite nanocomposites by maleic-anhydride functionalized rubber. Journal of Macromolecular Science Part B: Physics, **53**, 371–382 (2014). DOI: 10.1080/00222348.2013.839314

[24] Gelfer M. Y., Song H. H., Liu L., Hsiao B. S., Chu B., Rafailovich M., Si M., Zaitsev V.: Effects of organoclays on morphology and thermal and rheological properties of polystyrene and poly(methyl methacrylate) blends. Journal of Polymer Science Part B: Polymer Physics, **41**, 44–54 (2003). DOI: 10.1002/polb.10360

[25] Rotrekl J., Matějka L., Kaprálková L., Zhigunov A., Hromádková J., Kelnar I.: Epoxy/PCL nanocomposites: Effect of layered silicate on structure and behavior. Express Polymer Letters, **6**, 975–986 (2012). DOI: 10.3144/expresspolymlett.2012.103

[26] Kelnar I., Sukhanov V., Rotrekl J., Kaprálková L.: Toughening of recycled poly(ethylene terephthalate) with clay-compatibilized rubber phase. Journal of Applied Polymer Science, **116**, 3621–3628 (2010). DOI: 10.1002/app.31905

[27] Kelnar I., Rotrekl J., Kaprálková L., Hromádková J., Strachota A.: Effect of amine-terminated butadiene-acrylonitrile/clay combinations on the structure and properties of epoxy nanocomposites. Journal of Applied Polymer Science, **125**, 3477–3483 (2012). DOI: 10.1002/app.36696

[28] Ju D., Han L., Li F., Chen S., Dong L.: Crystallization, mechanical properties, and enzymatic degradation of biodegradable poly(ε-caprolactone) composites with poly(lactic acid) fibers. Polymer Composites, **34**, 1745–1752 (2013). DOI: 10.1002/pc.22578

[29] Neppalli R., Marega C., Marigo A., Bajgai M. P., Kim H. Y., Causin V.: Improvement of tensile properties and tuning of the biodegradation behavior of polycaprolactone by addition of electrospun fibers. Polymer, **52**, 4054–4060 (2011). DOI: 10.1016/j.polymer.2011.06.039

[30] Chen J., Lu L., Wu D., Yuan L., Zhang M., Hua J., Xu J.: Green poly(ε-caprolactone) composites reinforced with electrospun polylactide/poly(ε-caprolactone) blend fiber mats. ACS Sustainable Chemistry and Engineering, **2**, 2102–2110 (2014). DOI: 10.1021/sc500344n

[31] Fakirov S., Bhattacharyya D., Shields R. J.: Nanofibril reinforced composites from polymer blends. Colloids and Surfaces A: Physicochemical and Engineering Aspects, **313**, 2–8 (2008.) DOI: 10.1016/j.colsurfa.2007.05.038

[32] Dencheva N., Oliveira M. J., Carneiro O. S., Pouzada A. S., Denchev Z.: Preparation, structural development, and mechanical properties of microfibrillar composite materials based on polyethylene/polyamide 6 oriented blends. Journal of Applied Polymer Science, **115**, 2918–2932 (2010). DOI: 10.1002/app.31389

[33] Li Z-M., Li L-B., Shen K-Z., Yang W., Huang R., Yang M-B.: Transcrystalline morphology of an *in situ* microfibrillar poly(ethylene terephthalate)/poly(propylene) blend fabricated through a slit extrusion hot stretching-quenching process. Macromolecular Rapid Communications, **25**, 553–558 (2004). DOI: 10.1002/marc.200300086

[34] Friedrich K., Hoffmann J., Evstatiev M., Ye L., Mai Y. W.: Improvements of stiffness and strength of bioresorbable bone nails by the MFC-concept. Key Engineering Materials, **334–335**, 1181–1184 (2007). DOI: 10.4028/www.scientific.net/KEM.334-335.1181

[35] Kimble L. D., Bhattacharyya D., Fakirov S.: Biodegradable microfibrillar polymer-polymer composites from poly(L-lactic acid)/poly(glycolic acid). Express Polymer Letters, **9**, 300–304 (2015).
DOI: 10.3144/expresspolymlett.2015.27

[36] Xie L., Xu H., Niu B., Ji X., Chen J., Li Z-M., Hsiao B. S., Zhong G-J.: Unprecedented access to strong and ductile poly(lactic acid) by introducing *in situ* nanofibrillar poly(butylene succinate) for green packaging. Biomacromolecules, **15**, 4054–5064 (2014).
DOI: 10.1021/bm5010993

[37] Simeonova S., Evstatiev M., Li W., Burkhart T.: Fabrication and characterization of biodegradable polymer scaffolds adapting microfibrillar composite concept. Journal of Polymer Science Part B: Polymer Physics, **51**, 1298–1310 (2013).
DOI: 10.1002/polb.23332

[38] Haroosh H. J., Dong Y., Chaudhary D. S., Ingram G. D., Yusa S-I.: Electrospun PLA: PCL composites embedded with unmodified and 3-aminopropyltriethoxysilane (ASP) modified halloysite nanotubes (HNT). Applied Physics A: Materials Science and Processing, **110**, 433–442 (2013).
DOI: 10.1007/s00339-012-7233-7

[39] Lu L., Wu D., Zhang M., Zhou W.: Fabrication of polylactide/poly(ε-caprolactone) blend fibers by electrospinning: Morphology and orientation. Industrial and Engineering Chemistry Research, **51**, 3682–3691 (2012).
DOI: 10.1021/ie2028969

[40] Kelnar I., Fortelný I., Kaprálková L., Kratochvíl J., Angelov B., Nevoralová M.: Effect of layered silicates on fibril formation and properties of PCL/PLA microfibrillar composites. Journal of Applied Polymer Science, **133**, 43061/1–43061/9 (2015).
DOI: 10.1002/app.43061

[41] Shields R. J., Bhattacharyya D., Fakirov S.: Fibrillar polymer–polymer composites: Morphology, properties and applications. Journal of Materials Science, **43**, 6758–6770 (2008).
DOI: 10.1007/s10853-008-2693-z

[42] Kelnar I., Kaprálková L., Kratochvíl J., Kotek J., Kobera L., Rotrekl J., Hromádková J.: Effect of nanofiller on the behavior of a melt-drawn HDPE/PA6 microfibrillar composite. Journal of Applied Polymer Science, **132**, 41868/1–41868/9 (2015).
DOI: 10.1002/app.41868

[43] Wojdyr M.: Fityk: A general-purpose peak fitting program. Journal of Applied Crystallography, **43**, 1126–1128 (2010).
DOI: 10.1107/S0021889810030499

[44] Fakirov S., Bhattacharyya D., Lin R. J. T., Fuchs C., Friedrich K.: Contribution of coalescence to microfibril formation in polymer blends during cold drawing. Journal of Macromolecular Science Part B: Physics, **46**, 183, 193 (2007).
DOI: 10.1080/00222340601044375

[45] Kelnar I., Fortelný I., Kaprálková L., Hromádková J.: Effect of nanofiller on fibril formation in melt-drawn HDPE/PA6 microfibrillar composite. Polymer Engineering and Science, **55**, 2133–2139 (2015).
DOI: 10.1002/pen.24055

[46] Filippone G., Acierno D.: Clustering of coated droplets in clay-filled polymer blends. Macromolecular Materials and Engineering, **297**, 923–928 (2012).
DOI: 10.1002/mame.201100398

[47] Brus J., Urbanová M., Kelnar I., Kotek J.: A solid-state NMR study of structure and segmental dynamics of semicrystalline elastomer-toughened nanocomposites. Macromolecules, **39**, 5400–5409 (2006).
DOI: 10.1021/ma0604946

[48] Coativy G., Chevigny C., Rolland-Sabaté A., Leroy E., Lourdin D.: Interphase vs confinement in starch-clay bionanocomposites. Carbohydrate Polymers, **117**, 746–752 (2015).
DOI: 10.1016/j.carbpol.2014.10.052

[49] Moll J., Kumar S. K.: Glass transitions in highly attractive highly filled polymer nanocomposites. Macromolecules, **45**, 1131–1135 (2012).
DOI: 10.1021/ma202218x

[50] Chuang W-T., Jeng U-S., Hong P-D., Sheu H-S., Lai Y-H., Shih K-S.: Dynamic interplay between phase separation and crystallization in a poly(ε-caprolactone)/poly(ethylene glycol) oligomer blend. Polymer, **48**, 2919–2927 (2007).
DOI: 10.1016/j.polymer.2007.03.041

[51] Kamble R., Ghag M., Gaikawad S., Panda B. K.: Halloysite nanotubes and applications: A review. Journal of Advanced Scientific Research, **3**, 25–29 (2012).

[52] Kelnar I., Kaprálková L., Kratochvíl J., Padovec Z., Růžička M., Hromádková J.: Effect of layered silicates and reactive compatibilization on structure and properties of melt-drawn HDPE/PA6 microfibrillar composites. Polymer Bulletin, in press (2016).
DOI: 10.1007/s00289-015-1570-6

[53] Halpin J. C., Kardos J. L.: The Halpin-Tsai equations: A review. Polymer Engineering and Science, **16**, 344–352 (1976).
DOI: 10.1002/pen.760160512

[54] Vinogradov G. V., Malkin A. Y.: Rheology of polymers. Mir Publishers, Moscow (1980).

eXPRESS Polymer Letters Vol.10, No.5 (2016) 394–407
Available online at www.expresspolymlett.com
DOI: 10.3144/expresspolymlett.2016.37

Toughening of carbon fibre reinforced polymer composites with rubber nanoparticles for advanced industrial applications

N. G. Ozdemir[1*], *T. Zhang*[1], *I. Aspin*[2], *F. Scarpa*[3], *H. Hadavinia*[1], *Y. Song*[4]

[1]Kingston University London, SW15 3DW, United Kingdom
[2]Cytec Industrial Materials, DE75 7SP, United Kingdom
[3]ACCIS, University of Bristol, BS8 1TR, United Kingdom
[4]School of Energy Science and Engineering, University of Energy School and Technology of China, 611731 Chengdu, China

Received 4 October 2015; accepted in revised form 7 December 2015

Abstract. This study investigates the effects of nano carboxylic acrylonitrile butadiene rubber (CNBR-NP) and nano acrylonitrile butadiene rubber (NBR-NP) on the interlaminar shear strength and fracture toughness of carbon fibre reinforced polymer composites (CFRP) with dicyandiamide-cured epoxy matrix. The results show that nano-size dispersion of rubber significantly improved the Mode I delamination fracture toughness (G_{IC}) of the CFRP by 250% and its Mode II delamination fracture toughness (G_{IIC}) by 80% with the addition of 20 phr of CNBR-NP. For the NBR-NP system, the G_{IC} and G_{IIC} delamination fracture toughness of the CFRP were increased by 200 and 80% respectively with the addition of 20 phr (parts per hundred rubber) of nano rubber to the matrix. Scanning electron microscopy (SEM) images of the fracture surface revealed that the toughening was mainly achieved by debonding of the nano rubber, crack path deflection and fibre bridging.

Keywords: *polymer composites, processing technologies, nanomaterials, mechanical properties, nanocomposites*

1. Introduction

Carbon fibre reinforced polymer composites (CFRP) are widely used in advanced engineering technologies. Epoxy resins are employed as their matrix material, possessing outstanding mechanical performance and good processability. However, epoxy resins are relatively brittle which causes a major problem for the engineering performance of the final structure. To overcome this weakness, scientists have been toughening the formulations with nano and micron-scale particles in the last three decades.

Several research teams have explored the modification of the properties of epoxy resins by introducing various toughening agents such as reactive liquid rubber [1], thermoplastics [2, 3], micron scale rubber particles, nano rubber particles [4, 8], and nanoscale fillers [5, 6]. One of the main objectives behind the modification of the epoxy is to improve the fracture toughness of the resin without sacrificing intrinsic properties like the glass transition temperature (T_g) and its elastic modulus. A significant increase in the fracture toughness of advanced composite laminates can constitute a potential route towards designing composites with an extended lifetime and durability.

Recent studies have demonstrated the benefits of using nanoparticles to improve the mechanical prop-

*Corresponding author, e-mail: gulsine@yahoo.com
© BME-PT

erties of epoxy resins. Tang *et al*. [7] reported a 52% increase in the K_{IC} of epoxy resin with 0.2 wt% highly dispersed thermally reduced graphene sheets addition. Qi *et al*. [8] observed an improvement of the Izod impact strength of epoxy by 80% when dispersing 12 phr of nano acrylonitrile butadiene rubber. Phong *et al*. [9] observed a 70% increase in the mode I interlaminar fracture toughness of CFRP using epoxy matrix modified with 35 nm core-shell nano rubber at crack initiation. Fan *et al*. [10] evaluated the mechanical properties of nano rubber toughened epoxy resin and observed an improvement of 96% in Izod impact strength adding 12 phr of nano carboxylic nitrile butadiene rubber. Tripathi and Srivastava [11] improved the Izod impact strength and toughness of epoxy by 1.5 times with a 20 wt% dispersion of carboxyl terminated butadiene acrylonitrile copolymer (CTBN), however with a resulting slight decrease of the system T_g. In a recent review paper by Tang *et al*. [12], the highest improvements in the fracture toughness of FRP was achieved in hybrid composites, where the tougheners are silica particles and CTBN rubber. Hsieh *et al*. [13] demonstrated that it is possible to improve the interlaminar fracture toughness of CFRP by a factor of 2 with 10 wt% of silica and 9 wt% of CTBN addition to the epoxy matrix. In many of these studies, the drawbacks such as the high cost of the nanoparticles, the complicated processing methods and the inevitable decay in the T_g of the system restricted the large-scale production of these nano composites.

In our previous work, the effect of acrylonitrile-based nanorubbers on the cure kinetics, physical properties and the processing of epoxy resin were studied. We have showed that the acrylonitrile based nanorubber materials do not increase the viscosity of the specific epoxy resin beyond its processing limits; neither do they affect the T_g of the system [14]. Hence, previous work deals with the properties of the nanorubber-toughened matrix resin only, and the current work represents a continuation, studying the mechanical properties of the CFRP composites with the nanorubber toughened epoxy resin matrices. In a recent work we have also shown that nanorubber toughening of the resin can improve the damping capacity of the matrix, leading to an enhanced fatigue life [15].

In general, a significant improvement in the fracture toughness of the composites with the addition of nanorubber to their matrices is usually accompanied by a modification of the glass transition temperature (T_g) [16]. The work proposed in this paper is novel because it presents for the first time – to the best of the Authors' knowledge – a class of composites for which none of the intrinsic properties are deteriorated by the dispersion of nanorubber into their matrices [14]. The composites we present in this work feature a significant improvement in the delamination fracture toughness without any noticeable change in the T_g.

NBR-NP and CNBR-NP, both of which impart excellent compatibility with epoxy resins, are dispersed within dicyandiamide-cured epoxy matrices. To the best of the Authors' knowledge, due to the challenges in nano rubber dispersion within epoxy matrices and the complex structure and cross-linking mechanism of the dicyandiamide (DICY) curing agent, no previous study was reported on the toughening of dicyandiamide-cured epoxy matrix with acrylonitrile-based nano rubber materials. This forms the primary motivation of the current work.

A significant amount of work is available in the literature on the effect of the addition of nano rubber on the mechanical properties of epoxy resin systems [17–19]. However, there is a noticeable lack of work on the mechanical properties of CFRPs with nano rubber-toughened epoxy as matrix, mainly because of the viscosity build-up of the resin upon addition of nano rubber, which makes the penetration of the nano-modified resin through the fibres difficult. In this paper, we describe the analysis on CFRP produced by the hand lay-up technique. The hand lay-up process is not affected by viscosity changes, and – moreover – the relatively high viscosity of nano-modified matrices prevent resin leakage at high processing pressures, resulting therefore in improved interfacial properties.

Epoxy matrices were toughened with nano rubber by using a laboratory-scale triple mill. Narrow particle size and even distribution were maintained in the blends by this technique, resulting in a toughened epoxy network with enhanced mechanical properties.

We report novel CFRP composites with acrylonitrile based nano rubber-modified resin matrices with significantly improved fracture toughness and the ductility. The manufacturing methods used to produce the matrices and the composites could be potentially applied to scale-up processes in industry.

2. Materials and composites manufacturing

Liquid DGEBA (diglycidyl ether of Bisphenol A) (Araldite LY1556) with epoxide equivalent weight of 188 was supplied by Huntsman, UK. Dicyandiamide (DICY, Dyhard D50EP) was employed as the curing agent and a difunctional urone (Dyhard UR500) was used as the accelerator, both from Alz-Chem, UK. Nano carboxylic acrylonitrile butadiene rubber (CNBR-NP) Narpow VP-501 (single particle size distribution 50–100 nm, acrylonitrile content, 26 wt%), and nano acrylonitrile butadiene rubber (NBR-NP) Narpow VP-401 (single particle size distribution 100–150 nm, acrylonitrile content, 26 wt%) were received in powder form from SINOPEC, Beijing Research Institute of Chemical Industry (BRICI), China. For the details on the chemical reactions occurring between the components of the DGEBA resin, the DICY hardener and the difunctional urone accelerator the reader is referred to [20, 21].

Fumed silica (FS) received from Aerosil, UK (D_{50} = 1 μm) was adopted in some of the formulations to modify the rheological behaviour and help the CFRP laminates production. 199 GSM and 2×2 Twill carbon plies from Sigmatex (UK) Ltd. (Torayca T300) were employed to produce the CFRP panels. The matrix formulations used in this research work are given in Table 1.

The nano rubber was dispersed in the DGEBA matrix and the blend was speed-mixed at 3500 rpm for 1 minute. The blend was triple milled for six times at room temperature (RT = 23 °C). After mixing, it was then magnetically stirred at a speed of 320 rpm and degassed at 70 °C inside a glass flask for 16 hours under vacuum. The curing agent and the accelerator were added and the final mixture was speed-mixed at 2100 rpm for 6 minutes. Further details on the manufacturing techniques adopted can be found in [14].

A hand lay-up technique was used to produce the CFRP laminates. Bidirectional dry carbon plies with the nano rubber-toughened matrix were vacuum bagged and cured in an autoclave under a pressure of 6 atm. Twelve and eight layers of carbon plies were used to fabricate samples for double cantilever beam tests and interlaminar shear strength (ILSS) tests, respectively. The composite panels were heated to 120 °C at a heating rate of 0.5 °C/min and held for 1 hour at this temperature before cooling down to RT at the same rate, in an autoclave. The processing techniques are given in Figure 1.

The volume fraction of the carbon fibres in the composites was estimated with the Equation (1):

$$V_f[\%] = \frac{100 W_{FAW} N_p}{B \rho_F} \quad (1)$$

where W_{FAW} is the fibre areal weight, N_p is the number of plies, B is the thickness of the composites and ρ_F is the density of the carbon fibre. The value of W_{FAW} is quoted from the manufacturer's datasheet of the carbon fabrics, (199 g/m^2). The density of the carbon fibre is 1.76 g/cm^3. The carbon fibre volume fraction of the composites was 52±1%.

3. Experimental work

3.1. Short beam shear (SBS) test

Specimens with dimensions 20×6.35×3.2 mm were cut from the CFRP panels using a water jet. The SBS tests were conducted complying with ASTM D2344 at a crosshead speed of 1.3 mm/min using Zwick Z250 universal testing machine at RT (23 ºC). Test samples were placed on two roller supports that allow lateral motion and loaded at mid-span. The span length (S) to specimen thickness (t) ratio was 5. The beam was loaded until failure and the failure load was used to calculate the apparent interlaminar shear strength (APS) of the composites. The maximum load was interpreted as the initial maximum attained on load vs. crosshead displacement graphs. The APS was calculated by Equation (2):

$$APS = \frac{0.75 P_{max}}{wt} \quad (2)$$

where P_{max} represents the maximum load, w the width of the specimen and t the thickness of the specimen. Five samples were tested for each composition.

Table 1. Formulations used within experimental work, in phr (parts per hundred of DGEBA)

CODE	DGEBA	DICY	Diurone	NBR-NP	CNBR-NP	Fumed Silica
R	100	14	6	–	–	–
R/ X FS	100	14	6	–	–	X
X CNBR-NP/ R	100	14	6	–	X	–
X NBR-NP/ R	100	14	6	X	–	–

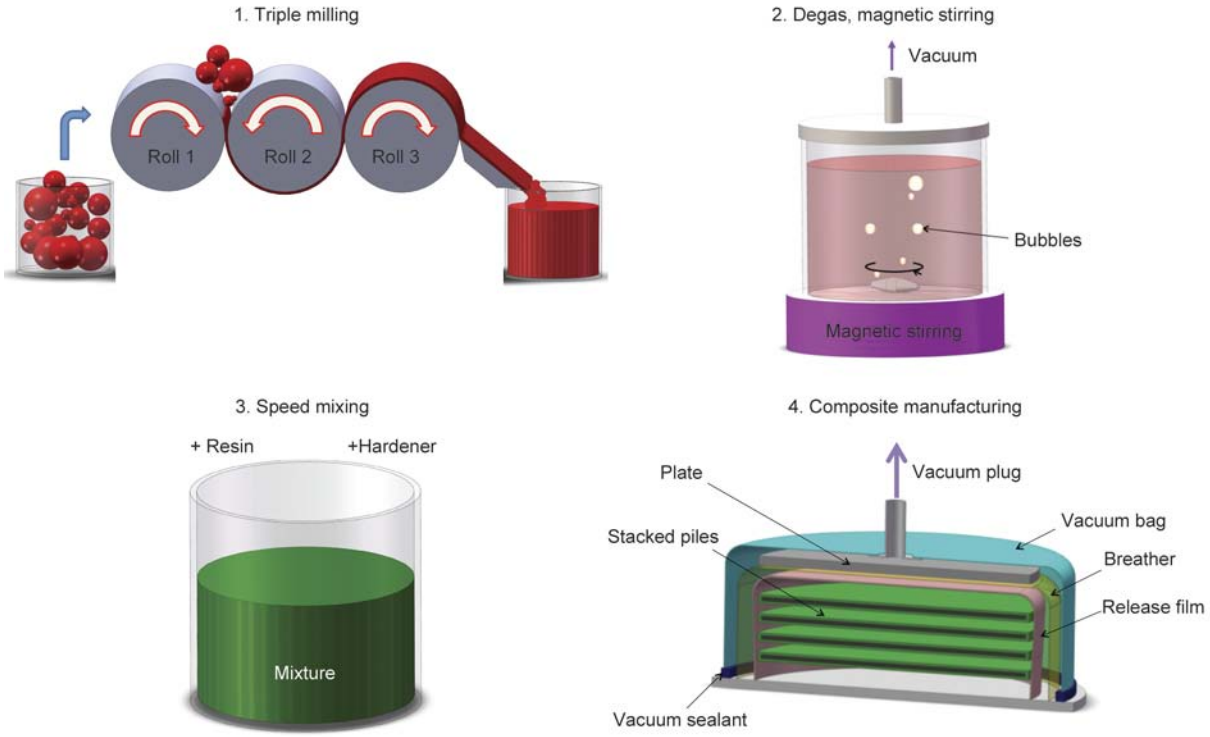

Figure 1. Manufacturing techniques used in this study

3.2. Mode I delamination fracture toughness using DCB specimen

The effect of nano rubber toughening on Mode I delamination toughness G_{1C}, was studied using a double cantilever beam (DCB) test on CFRP samples following the EN6033 standard by using a Zwick Z250 machine at a crosshead speed of 10 mm/min. The samples were loaded perpendicular to the delamination surfaces.

A piece of release film (PTFE film) was placed at the midplane of the stacked plies during the hand lay-up process to create a 30 mm long pre-crack. Five DCB specimens with dimensions of 250×25×3 mm were tested from each formulation. Screw able grips were clamped onto the two faces of the specimen end having the pre-crack. The specimens' edges were coated with white paint and marked for a clear reading of the crack length. The pre-cracked sample was loaded continuously by peel-forces until a total propagated crack length of approximately 100 mm was achieved. The interlaminar fracture toughness energy was calculated from the propagated crack length and the applied energy determined from the load-cross head displacement diagram. Five samples were tested for each composition.

The interlaminar fracture toughness is calculated from the Equation (3):

$$G_{IC} = \frac{A}{aw} \cdot 10^6 \tag{3}$$

where G_{IC} is the fracture toughness, in [J/m^2], A is the required energy to achieve the total propagated crack length, in Joules (integration of the area under the load vs. crosshead displacement diagram), a is the crack length, in [mm] (final crack length minus initial crack length), w is the width of the specimen, [mm].

Scanning electron microscopy (SEM) at secondary electron mode was used to verify the distribution of the nano rubber within the resin matrix and the toughening mechanisms. For this, fracture surfaces of the CFRP laminates were examined. The samples were vacuum coated with gold using a sputter coater. Images were taken using an accelerating voltage of 20–25 keV with a magnification between 90 to 2000 times.

3.3. Mode II interlaminar fracture toughness (end notched flexure test)

Five specimens for each composite configuration were tested following the EN6034 standard with Zwick Z50 machine at a crosshead speed of 1 mm/min. The samples were positioned on a three-point bend fixture with a total span of 100 mm; with an initial crack length of 34–35 mm.

The load and crosshead movement were continuously recorded and the crack length was recorded using a digital video camera. The sample was unloaded when the maximum load is reached. The mode II fracture toughness, G_{IIC}, was calculated using the maximum load sustained by the sample.

The G_{IIC} value was calculated [22, 23] as given by Equation (4):

$$G_{IIC} = \frac{9000Pa^2\delta}{2w\left(\frac{1}{4}L^3 + 3a^3\right)} \quad (4)$$

where G_{IIC} is the Mode II fracture toughness energy in [J/m^2], P is the load [N], δ is the crosshead displacement at the crack growth onset [mm], w the specimen width [mm], a the initial crack length [mm] and L the span length [mm]. Five samples were tested for each composition.

4. Results and discussion

4.1. Morphology

Figure 2 shows fracture surfaces of the CFRP samples. The nano rubber appears to have bonded to the surface of the carbon fibre and debonded from the matrix. In this figure, both CNBR-NP and NBR-NP provide an even dispersion within the composites.

In the NBR-NP modified resins, an interphase formed between the carbon fibre and the matrix that is an indication of a strong fibre-matrix interfacial adhesion (Figure 2b). This suggests that the NBR-NP developed a resistance to fibre-matrix failure. It is possible that the NBR-NP particles act like a sizing agent for the carbon fibres, therefore enhancing the fibre-matrix interfacial strength. It is clear from the inspection of Figure 2b that the NBR-NP particles are attached to the fibre surface, creating a higher contact area between the latter and forming mechanical interlocking sites [24].

In CFRP composites, the difference between the elastic moduli of the carbon fibre and the resin matrix is quite significant and the stress transfer between the two phases is weak, creating residual stresses at the interface. However, the relatively compliant nanorubber toughened matrix can deform plastically, therefore relaxing the stress concentrations [15]. Plastic deformation at the fibre-matrix interface may act as an energy dissipation mechanism that provides an improved interfacial strength. The soft particles resist to fibre-matrix failure due to the creation of an interphase, as shown in Figure 2b. Interestingly, this kind of interphase was not observed in the laminates with the unmodified matrix and the CNBR-NP modified matrices.

Figure 3 shows the SEM images of the matrix fracture surface in between the carbon fibres. It can be seen that the dispersion of CNBR-NP in epoxy resin is better when compared to that of NBR-NP. This is due to the carboxyl group of CNBR-NP, helping with better dispersion in the matrix [25]. Further details on the morphology of these blends can be found in [14].

The toughening mechanisms of both systems were identified as crack front pinning, crack path deflection, crack bridging and nano rubber debonding, the latter followed by plastic void growth of the epoxy (Figure 3). In crack front pinning mechanism, crack growth is prevented by the rigid particles and hence, extra energy is required for crack propagation [26]. In crack path deflection mechanism, nanoparticles

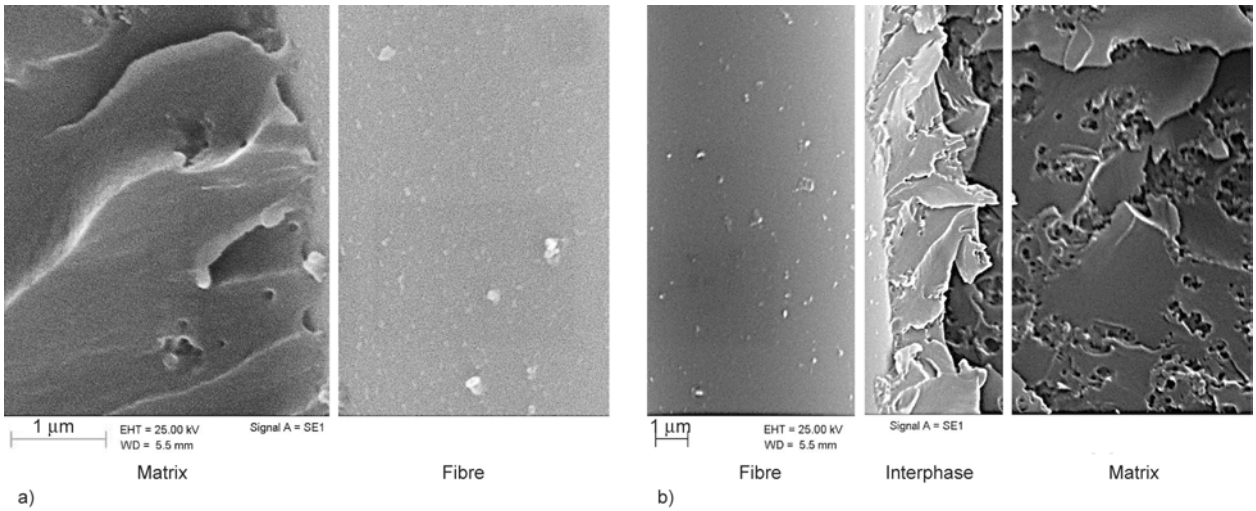

Figure 2. SEM image of the fracture surface of (a) CFRP with 20CNBR-NP/ R matrix, (b) CFRP with 10NBR-NP/ R matrix

deviate the crack from its main plane resulting in an increase in the surface area of the crack and the energy to propagate such a crack. In crack bridging mechanism, the particles link separate crack surfaces to each other and reduce the stress concentration at the crack tips. Presence of holes with larger diameters than the particles within the structures shows that plastic void growth of the epoxy matrix, initiated by debonding of the particles has occurred [27–29]. Matrix-particle debonding is essential in the plastic void growth mechanism, which is a significant part of the plastic deformation in nano rubber modified epoxy samples that reduces the stress at the crack tip [30, 31]. From the observation of the micrographs in Figure 3 it is possible to note the presence of a non-homogeneous void size distribution, with some of the voids larger than the nano-rubber diameter (CNBR-NP, 50-100 nm or NBR-NP, 100–150 nm). This fact proves that the debonding mechanism follows a plastic void growth, which is major energy dissipation and hence a toughening micro mechanism [32]. Rubber nano particle debond-

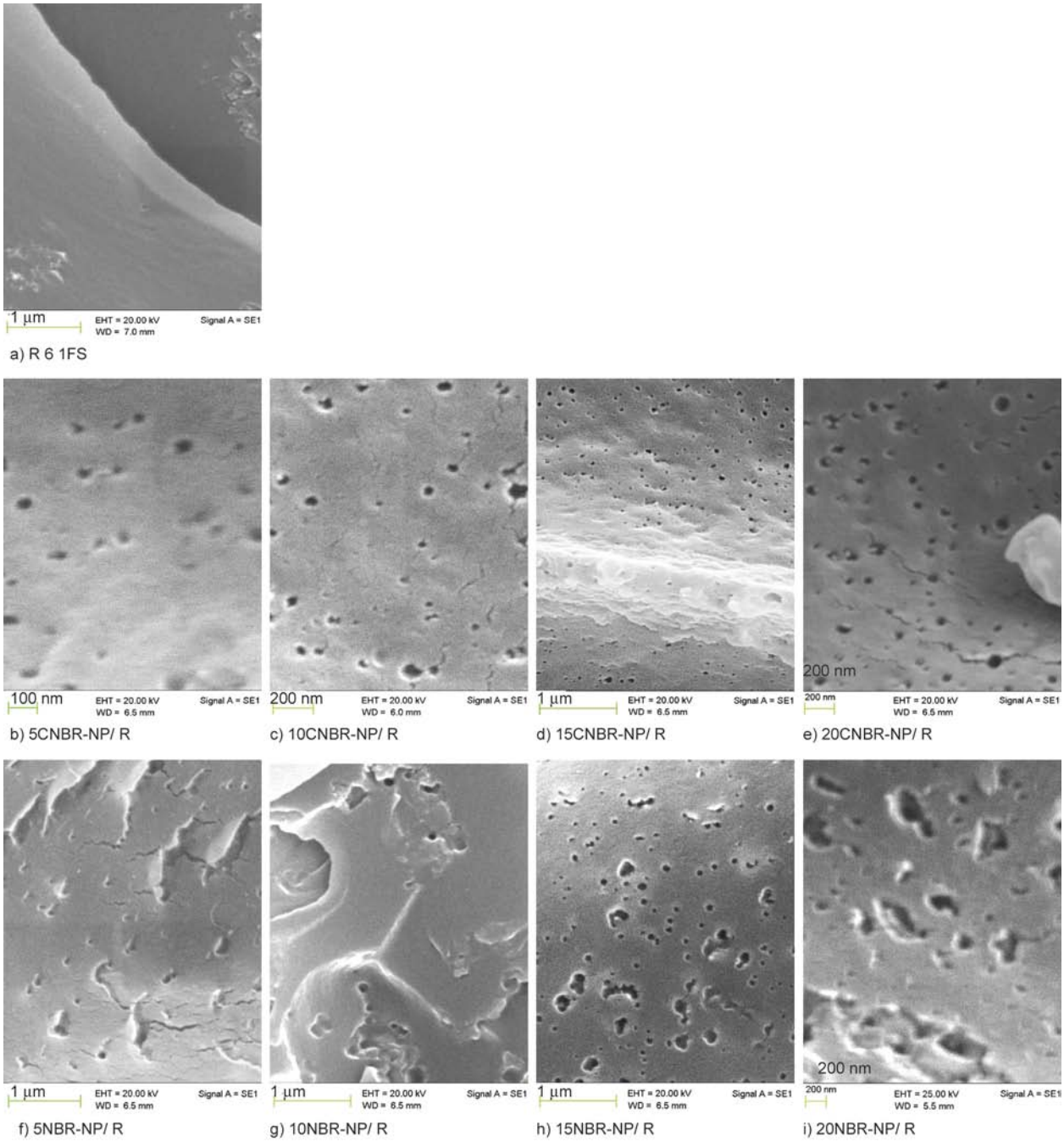

Figure 3. SEM images of the matrices on the DCB fracture surface of R 6 1FS (a), CNBR-NP/ R (b–e), NBR-NP/ R (f–i)

ing from the resin matrix occurs at the particle-matrix interface, therefore reducing the degree of stresses acting in the matrix adjacent to the particles.

4.2. Interlaminar shear behaviour

The apparent interlaminar shear strength and the failure stresses and corresponding strains are given in Table 2. For each laminate tested, a load-displacement curve that represents the average of the five samples is shown Figures 4a and 4b. Figure 4c shows the behaviour of the apparent interlaminar shear strength [MPa] vs. the nanorubber loading [phr] for the CFRP samples.

The response of each laminate shows a nearly linear elastic behaviour at the early stages of loading. This continues until an apparent elastic limit is reached. After this point, each laminate shows a decrease in load. This decrease in load is sudden in brittle composites, like CFRP with a neat resin matrix. However, with an increase in the nano rubber concentration, the decrease in load is ductile and apparently the crosshead displacement till fracture is larger and increases continuously with the rubber content in the samples. This increase in crosshead displacement is due to a decrease in the composite stiffness with rubber concentration, which results in higher deflections at the same load levels. Bai *et al*. [33] previously reported that in the linear part of the load-displacement curve fibre fragmentation was observed

Table 2. Apparent interlaminar shear strength of the CFRP samples, σ – standard deviation, s – displacement at fracture

X (NP phr)	X CNBR-NP/ R			X NBR-NP/ R		
	APS [MPa]	σ [MPa]	s [mm]	*APS* [MPa]	σ [MPa]	s [mm]
0 (0.26 FS)	71.5	1.7	0.6	71.5	1.7	0.6
0 (1 FS)	70.1	1.1	0.6	70.1	1.1	0.6
5	67.8	0.6	0.5	68.8	0.7	0.7
10	62.6	1.2	0.6	62.0	0.6	0.8
15	61.0	0.4	0.7	56.6	0.1	0.7
20	55.6	0.8	0.8	54.0	1.5	0.9

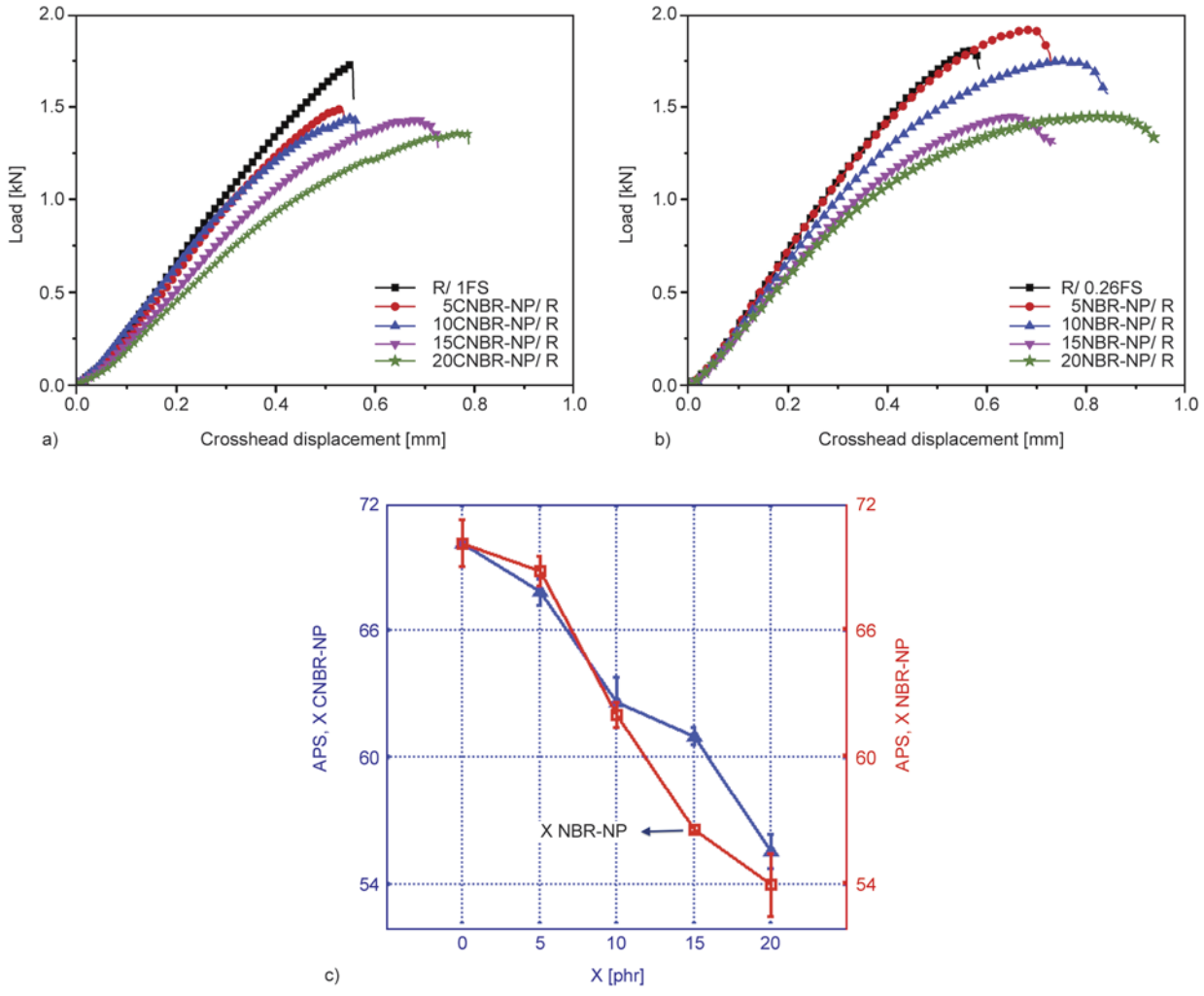

Figure 4. Load vs. crosshead (CH) displacement graph of CFRP in ILSS specimens with (a) X CNBR-NP/ R matrix, (b) X NBR-NP/ R matrix, (c) apparent interlaminar shear strength [MPa] vs. X [phr] of the CFRP samples

in the central part of the beam, and matrix damage was noticed on the shearing section resulting in the non-linearity of load vs. displacement curve. Figure 4 shows that with an increase in nano rubber concentration, the linearity of the curve until failure decreases, indicating higher matrix damage.

The results show that CFRP with neat R/ 1FS matrix reached the highest peak load, and the apparent interlaminar shear strength (*APS*) decreased continuously with an increase in the rubber loading. Fumed silica did not show a noticeable effect on the results. The decrease in the *APS* values is attributed to the low strength and stiffness of the nano rubber particles decreasing the final strength and stiffness of the laminates, which is an expected phenomenon in nano rubber modified CFRPs.

Failure modes of the short beam shear specimens

The failed short beam specimens were examined with SEM at secondary electron mode to assess the damage in the laminates. In Figures 5a and 5b delamination and fibre buckling is observed in the CFRPs with the neat R/ 1FS matrix. In Figures 5c and 5d it is possible to observe that the tensile stress generated at the bottom of the specimen has caused transverse tensile cracks. Delamination is also observed between the carbon ply and the matrix in Figures 5c–5f, and fibre pull-out due to delamination is present in Figures 5d and 5f. In Figures 5e and 5h cracks at 45° are observed due to the maximum shear stress occurring in ±45° directions under uniaxial loading. Failure did not occur at the mid-plane in any of the specimens. Instead, interfacial shear failure occurred above and below the mid-plane.

From the analysis of the SEM images (Figure 3) it is clear that the level of porosity in the structure increases with the nanorubber loading. Voids cause a reduction in the apparent shear strength by decreasing the net cross sectional area and by creating stress concentrations [34]. Another factor affecting the *APS* value is the thickness of the interlaminar layers. Previous studies have shown that an increase of the interply resin thickness enhances the interlaminar mechanical properties [35]. Small thickness variations arising from differences in resin content of the composites may result in different interlaminar properties. A most important factor is also the degree of crosslinking [36]. The morphology and the change in stoichiometry of the matrix with the nanorubber dispersion can affect the interlaminar shear stiffness and strength properties. However, we have proved with dynamic mechanical analysis that the change in the degree of crosslinking with the nanorubber modification is insignificant [14].

To summarise, the consistent decrease of the *APS* value with the nanorubber concentration may be explained by the lower quality of the laminates with high void content, and by the low stiffness of the nanorubber particles that cause a reduction in the stiffness of the resin.

4.3. Mode I fracture toughness using double cantilever beam (DCB)

The Mode I fracture toughness of the CFRP laminates based on an average of 5 samples are summarised in Table 3. One can observe a 250 and 200% increase in G_{IC} with 20 phr CNBR-NP and NBR-NP addition to the matrix, respectively.

Figures 6 shows the load vs. displacement curves of the CFRP samples with the CNBR-NP and NBR-NP modified matrices respectively. This figure shows that the maximum load and crosshead displacement attained before fracture increases consistently with increasing the nano rubber concentration. Figure 6 also indicates that the force linearly increases until it reaches the maximum force value, and then gradually decreases with zigzag shape in the propagation stages. This could be due to the variations of resin-rich regions or fibre-rich regions along the longitudinal directions [37, 38].

The fracture process was recorded by a video camera to analyse the crack initiation and propagation. In Figure 7a, the crack propagation is rather brittle and no microcrack formation is observed in the CFRP panel with R/ 1FS matrix. However, in the laminate with 20CNBR-NP/ R matrix, high amount of microcrack formation was observed and the crack often deviated from its path (Figure 7b). Such crack propagation in zig-zag manners showing meandering paths required a higher driving force and created a larger fracture area, resulting in higher frac-

Table 3. G_{IC} test data, σ – standard deviation

X [phr]	X CNBR-NP/ R			X NBR-NP/ R		
	G_{IC} [J/m^2]	σ [J/m^2]	Increase [%]	G_{IC} [J/m^2]	σ [J/m^2]	Increase [%]
0 (1 FS)	372	32	–	–	–	–
5	517	24	39	510	20	37
10	840	15	126	803	29	116
15	950	102	155	926	56	149
20	1305	105	251	1127	89	203

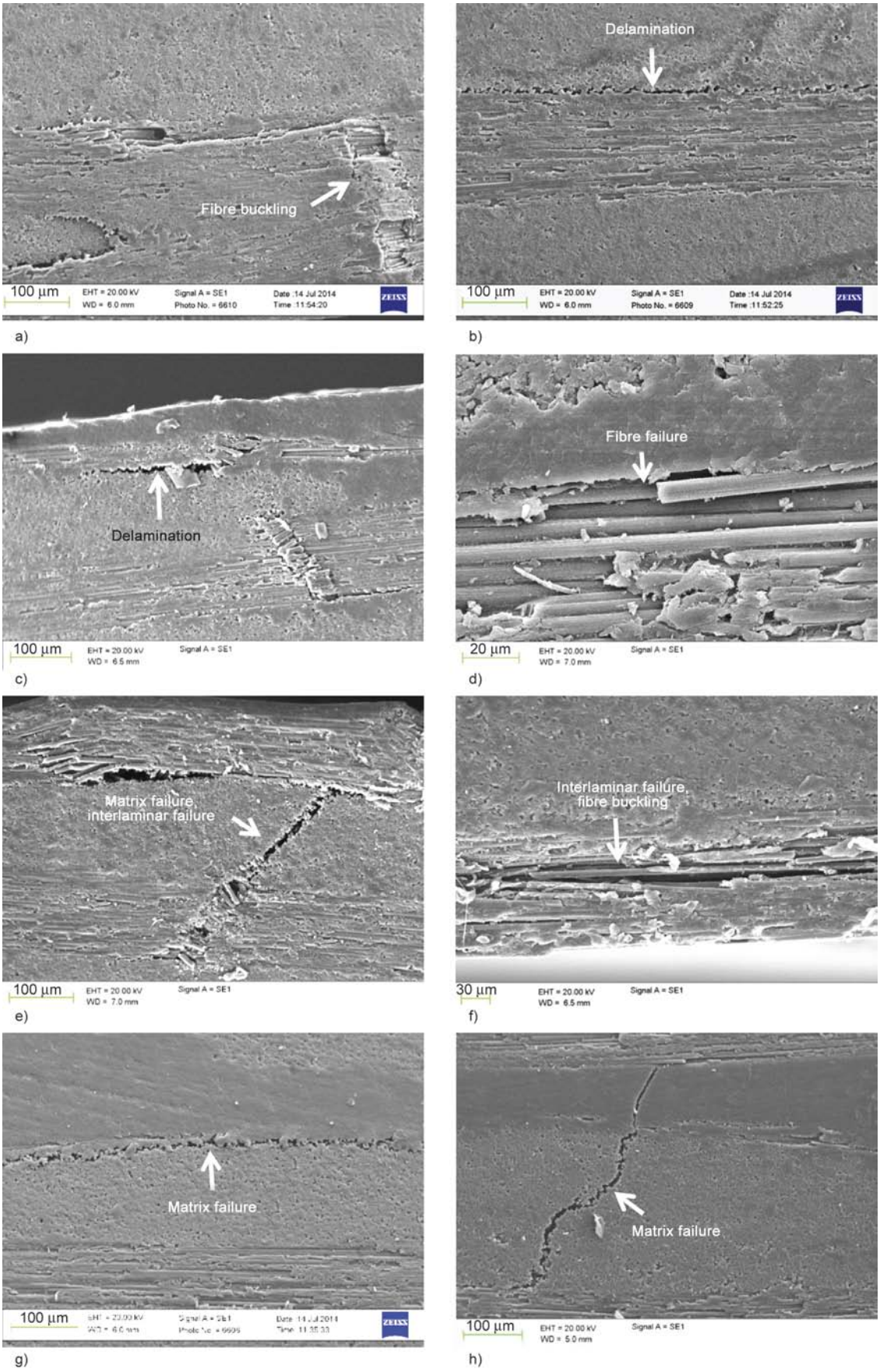

Figure 5. (a, b) Edge view of CFRP with R/ 1FS matrix, (c, d) edge view of CFRP with 10CNBR-NP/ R matrix, (e, f) edge view of CFRP with 15CNBR-NP/ R matrix, (g, h) edge view of 20CNBR-NP/ R matrix

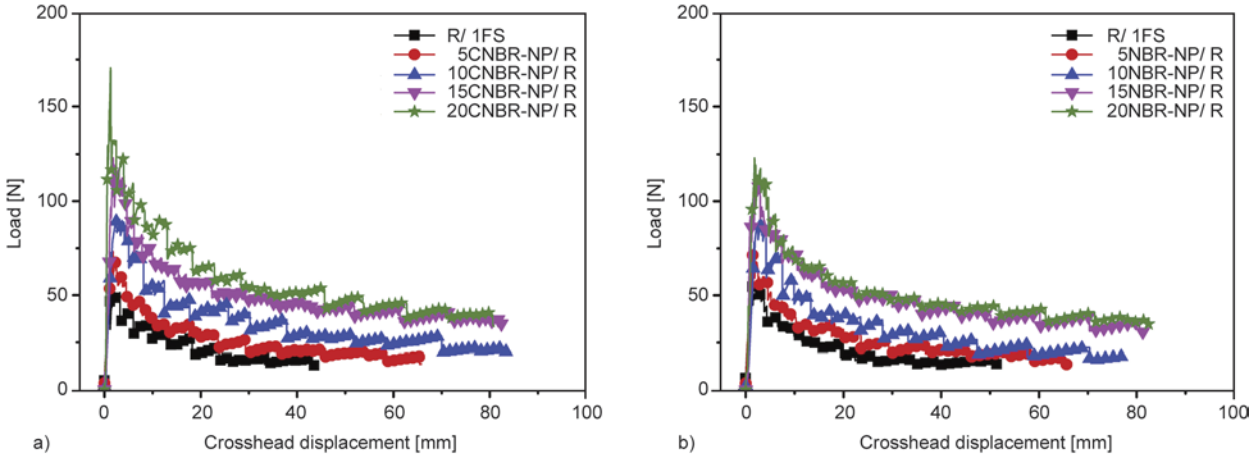

Figure 6. Load vs. crosshead displacement graph of DCB samples with (a) X CNBR-NP/ R matrix, (b) X NBR-NP/ R matrix

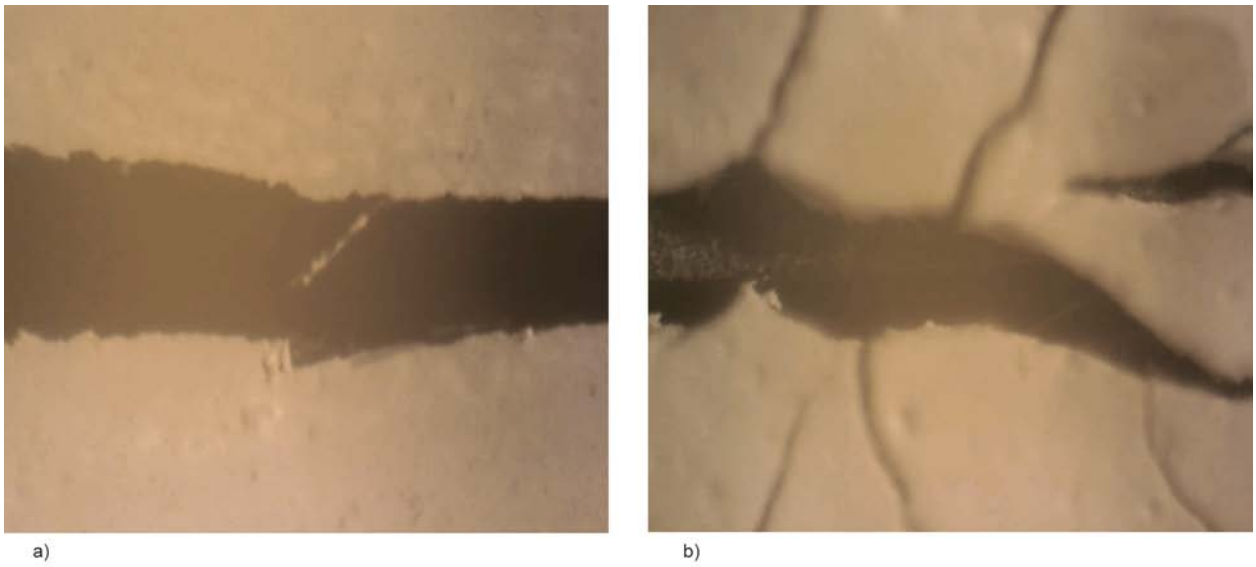

Figure 7. Crack propagation in DCB test, (a) CFRP with R/ 1FS matrix, (b) CFRP with 20CNBR-NP/ R matrix

ture toughness. Hence, the enhanced interlaminar fracture toughness of CFRP panels with nano-toughened matrices is mainly attributed to the increased fracture surface area due to the microcracking and crack deflection [39].

The fracture surfaces of the DCB samples were further examined with SEM, and fibre breakage, interface debonding and delamination were observed in all of the composites configurations.

In Figures 8a) and 8b, the fracture surface of the CFRP with the unmodified epoxy matrix shows a typical brittle fracture with no plastic deformation. Slight fibre bridging can be observed in these images. Figures 8c and 8d are the micrographs of the fracture surface of the sample with 20CNBR-NP/ R matrix that shows fibre bridging in higher aspects. This high amount of fibre bridging within the structures accounts for the high interlaminar fracture toughness values. In Figures 8d and 8f, holes can be observed on the fibre troughs, which may indicate that the nanoparticles have adhered to the carbon fibre surface. In Figures 8e and 8f, an even higher amount of tortuosity is observed due to good bonding of the NBR-NP modified resin matrix to the carbon fibre. Better adherence of the NBR-NP modified resin matrix to the fibres was also proved in Figure 2b.

4.4. Mode II interlaminar fracture toughness (end notched flexure test)

The Mode II fracture toughness data of CFRP samples obtained from ENF specimens are presented in Table 4. Mode II interlaminar fracture energy values are higher than Mode I values because the matrix crack propagation occurs in shear rather than tensile. There is a strong dependency of the Mode II frac-

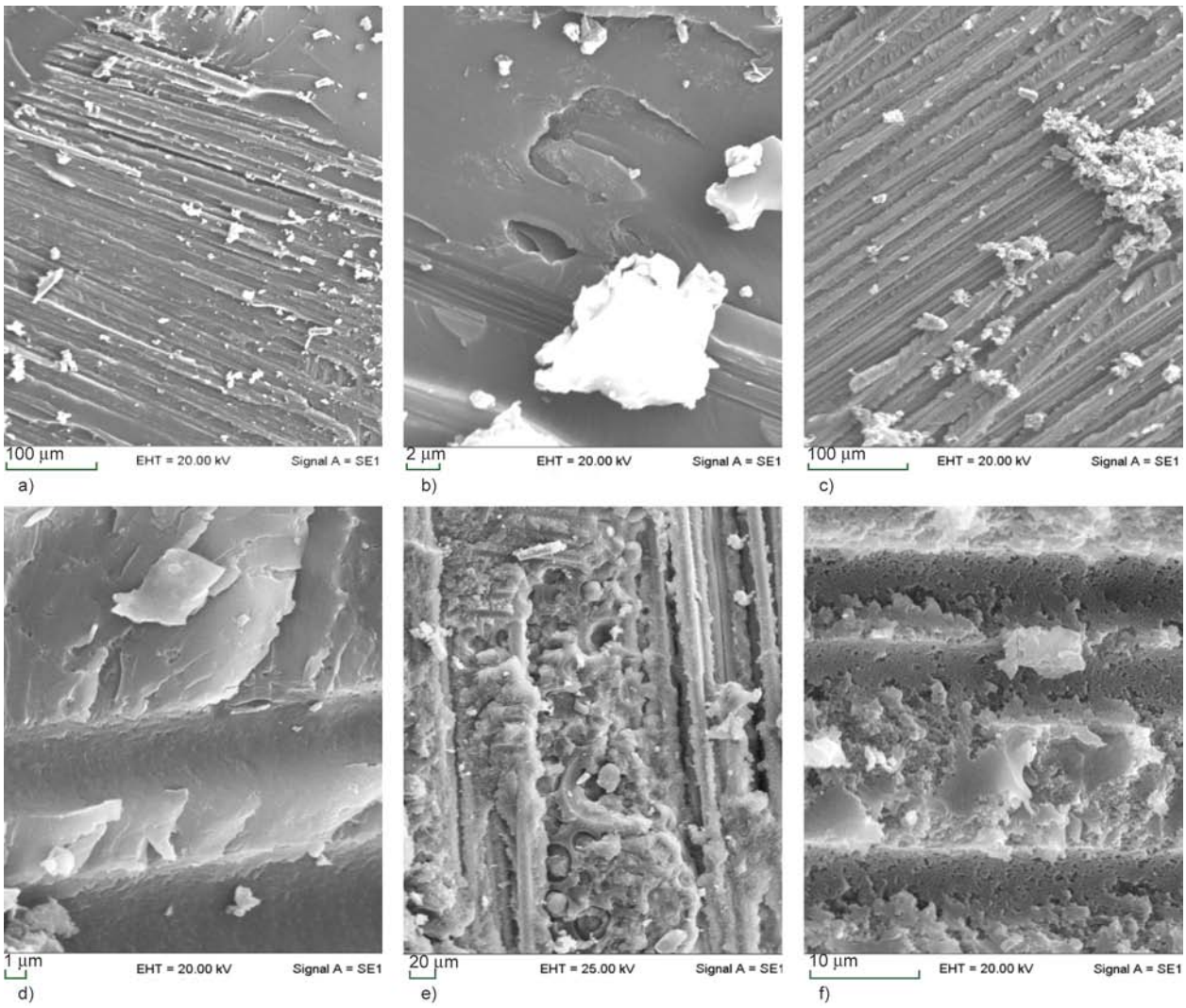

Figure 8. SEM images of the fracture surfaces in DCB samples (a) and (b) laminate with R/ 1FS matrix, (c) and (d) laminate with 20CNBR-NP/ R matrix, (e) and (f) laminate with 20NBR-NP/ R matrix

ture toughness (G_{IIC}) versus the fibre-matrix bonding. The increase in G_{IIC} toughness with nano rubber concentration can be explained by good adhesion of the nano rubber toughened resin matrix to the carbon fibres (see Figure 8). When the fibre-matrix bonding is strong, energy absorbing phenomena such as matrix deformation, matrix cracking, fibre pull-out, and interfacial failure takes place. As a result, the G_{IIC} of the composites shows a significant improvement. Figure 9 shows the corresponding load vs. displacement for the ENF samples. The load increases until the crack initiates and propagates, which then results in a decrease in load. Once the decrease in load was observed, the test was stopped. It can be seen that with an increase in nano rubber loadings, the maximum load attained before fracture and the displacement to failure increases.

Table 4. G_{IIC} test data, σ – standard deviation

X [phr]	X CNBR-NP/ R			X NBR-NP/ R		
	G_{IC} [J/m^2]	σ [J/m^2]	Increase [%]	G_{IC} [J/m^2]	σ [J/m^2]	Increase [%]
0 (1 FS)	1090	103	–	1090	103	–
5	1156	56	6	–	–	–
10	1489	89	37	1739	69	60
15	1823	122	67	–	–	–
20	1976	46	81	2000	58	83

5. Conclusions

In the present study, nano-sized CNBR and NBR rubber particles were used to improve the toughness of CFRP composites. Special emphasis was placed on the fracture toughness of two nano-acrylonitrile butadiene rubber toughened epoxy composites under mode I and mode II loading conditions. The most efficient dispersion technique was identified the nano rubber systems and the mechanical and morphological properties of carbon fibre laminate produced with these nano-modified matrices were studied in detail.

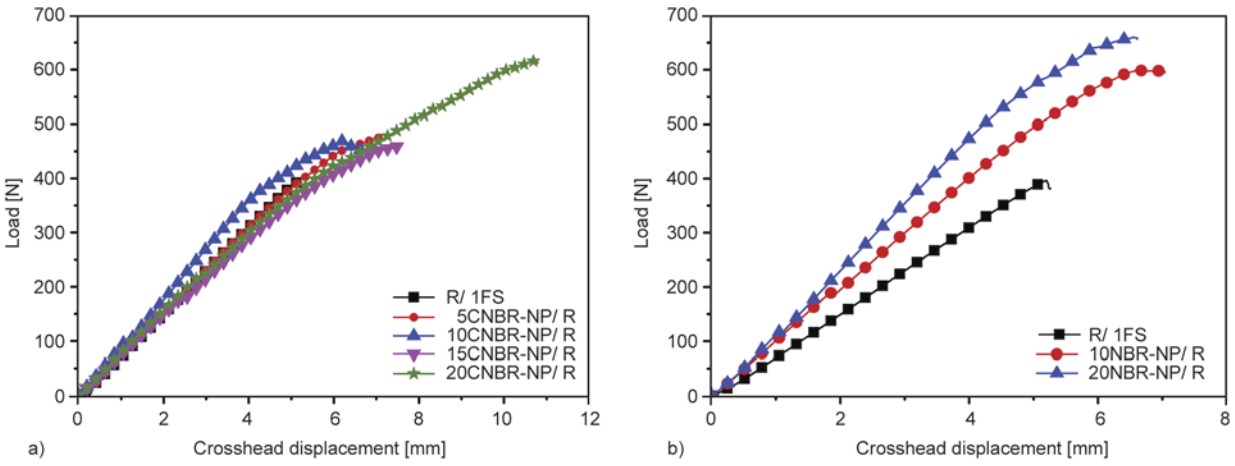

Figure 9. Load vs. crosshead displacement of the ENF samples with (a) X CNBR-NP/ R matrix, (b) X NBR-NP/ R matrix

The fracture toughness of the CFRP laminates improved significantly with the nano rubber modification of the matrix, which was justified by the changed morphology of the resins. G_{IC} and G_{IIC} toughness of CFRP panels were increased by 250 and 80% with rubber loading in both systems. The toughening mechanisms were identified as crack path deflection, debonding and micro-cracking of the rubber particles. The elastomeric nature of the nano rubbers caused a reduction in the interlaminar shear strength, indicating an enhancement of the flexibility of the CFRP composites with the dispersion of the nano rubber.

Acknowledgements

The research leading to these results has received funding from the FP7-MC-ITN under grant agreement No. 264710. The authors would like to thank the Directorate-General for Science, Research and Development of the European Commission for financial support of the research. The authors from Kingston University London would like to thank SINOPEC, Beijing Research Institute of Chemical Industry (BRICI), China and Cytec Industrial Materials for their kind supply of chemicals for the study.

References

[1] Shi H-Q., Sun B-G., Liu Q., Yang Z-Y., Yi K., Zhang Y., Fu S-Y.: A high ductility RTM epoxy resin with relatively high modulus and T_g. Journal of Polymer Research, **22**, 134/1–134/9 (2015).
DOI: 10.1007/s10965-015-0774-7

[2] Nash N. H., Young T. M., McGrail P. T., Stanley W. F.: Inclusion of a thermoplastic phase to improve impact and post-impact performances of carbon fibre reinforced thermosetting composites – A review. Materials and Design, **85**, 582–597 (2015).
DOI: 10.1016/j.matdes.2015.07.001

[3] Zhou H., Xu S.: A new method to prepare rubber toughened epoxy with high modulus and high impact strength. Materials Letters, **121**, 238–240 (2014).
DOI: 10.1016/j.matlet.2014.01.160

[4] Thomas S.: Micro and nano structured epoxy rubber blends. Wiley, Weinheim (2014).

[5] Meng Q., Wang C. H., Saber N., Kuan H-C., Dai J., Friedrich K., Ma J.: Nanosilica-toughened polymer adhesives. Materials and Design, **61**, 75–86 (2014).
DOI: 10.1016/j.matdes.2014.04.042

[6] Sprenger S., Kothmann M. H., Altstaedt V.: Carbon fiber-reinforced composites using an epoxy resin matrix modified with reactive liquid rubber and silica nanoparticles. Composites Science and Technology, **105**, 86–95 (2014).
DOI: 10.1016/j.compscitech.2014.10.003

[7] Tang L-C., Wan Y-J., Yan D., Pei Y-B., Zhao L., Li Y-B., Wu L-B., Jiang J-X., Lai G-Q.: The effect of graphene dispersion on the mechanical properties of graphene/epoxy composites. Carbon, **60**, 16–27 (2013).
DOI: 10.1016/j.carbon.2013.03.050

[8] Qi G., Zhang X., Li B., Song Z., Qiao J.: The study of rubber-modified plastics with higher heat resistance and higher toughness and its application. Polymer Chemistry, **2**, 1271–1274 (2011).
DOI: 10.1039/C0PY00413H

[9] Phong N. T., Gabr M. H., Anh L. H., Duc V. M., Betti A., Okubo K., Chuong B., Fujii T.: Improved fracture toughness and fatigue life of carbon fiber reinforced epoxy composite due to incorporation of rubber nanoparticles. Journal of Materials Science, **48**, 6039–6047 (2013).
DOI: 10.1007/s10853-013-7400-z

[10] Fan H., Liu Y., Zhang X., Gao J., Song Z., Tang B., Wei G., Qiao J.: Interface and properties of epoxy resin modified by elastomeric nano-particles. Science in China Series B: Chemistry, **48**, 148–155 (2005).
DOI: 10.1360/04yb0022

[11] Tripathi G., Srivastava D.: Effect of carboxyl-terminated poly(butadiene-*co*-acrylonitrile) (CTBN) concentration on thermal and mechanical properties of binary blends of diglycidyl ether of bisphenol-A (DGEBA) epoxy resin. Materials Science and Engineering: A, **443**, 262–269 (2007).
DOI: 10.1016/j.msea.2006.09.031

[12] Tang Y., Ye L., Zhang Z., Friedrich K.: Interlaminar fracture toughness and CAI strength of fibre-reinforced composites with nanoparticles – A review. Composites Science and Technology, **86**, 26–37 (2013).
DOI: 10.1016/j.compscitech.2013.06.021

[13] Hsieh T. H., Kinloch A. J., Masania K., Lee J. S., Taylor A. C., Sprenger S.: The toughness of epoxy polymers and fibre composites modified with rubber microparticles and silica nanoparticles. Journal of Materials Science, **45**, 1193–1210 (2010).
DOI: 10.1007/s10853-009-4064-9

[14] Ozdemir N. G., Zhang T., Hadavinia H., Aspin I., Wang J.: Rheological properties, cure characteristics, and morphology of acrylonitrile-based nanorubber modified epoxy. Journal of Applied Polymer Science, **132**, 41911/1–41911/13 (2015).
DOI: 10.1002/app.41911

[15] Ozdemir N. G., Zhang T., Hadavinia H., Aspin I., Scarpa F.: Influence of nanorubber toughening on the tensile deformation and tensile fatigue behaviour of a carbon fibre-reinforced epoxy composite. Journal of Composite Materials, in press (2015).
DOI: 10.1177/0021998315609976

[16] Acebo C., Alorda M., Ferrando F., Fernández-Francos X., Serra A., Morancho J. M., Salla J. M., Ramis X.: Epoxy/anhydride thermosets modified with end-capped star polymers with poly(ethyleneimine) cores of different molecular weight and poly(ε-caprolactone) arms. Express Polymer Letters, **9**, 809–823 (2015).
DOI: 10.3144/expresspolymlett.2015.76

[17] Quan D., Ivankovic A.: Effect of core–shell rubber (CSR) nano-particles on mechanical properties and fracture toughness of an epoxy polymer. Polymer, **66**, 16–28 (2015).
DOI: 10.1016/j.polymer.2015.04.002

[18] Hsieh T. H., Kinloch A. J., Taylor A. C., Kinloch I. A.: The effect of carbon nanotubes on the fracture toughness and fatigue performance of a thermosetting epoxy polymer. Journal of Materials Science, **46**, 7525–7535 (2011).
DOI: 10.1007/s10853-011-5724-0

[19] Wu S., Ladani R. B., Zhang J., Bafekrpour E., Ghorbani K., Mouritz A. P., Kinloch A. J., Wang C. H.: Aligning multilayer graphene flakes with an external electric field to improve multifunctional properties of epoxy nanocomposites. Carbon, **94**, 607–618 (2015).
DOI: 10.1016/j.carbon.2015.07.026

[20] Poisson N., Maazouz A., Sautereau H., Taha M., Gambert X.: Curing of dicyandiamide epoxy resins accelerated with substituted ureas. Journal of Applied Polymer Science, **69**, 2487–2497 (1998).
DOI: 10.1002/(SICI)1097-4628(19980919)69:12<2487::AID-APP20>3.0.CO;2-T

[21] Lee Y-D., Wang S-K., Chin W-K.: Liquid-rubber-modified epoxy adhesives cured with dicyandiamide. I. Preparation and characterization. Journal of Applied Polymer Science, **32**, 6317–6327 (1986).
DOI: 10.1002/app.1986.070320813

[22] Pegorin F., Pingkarawat K., Daynes S., Mouritz A. P.: Influence of z-pin length on the delamination fracture toughness and fatigue resistance of pinned composites. Composites Part B, **78**, 298–307 (2015).
DOI: 10.1016/j.compositesb.2015.03.093

[23] Gibson R. F.: Principles of composite materials mechanics. McGraw Hill, New York (1994).

[24] Drescher P., Thomas M., Borris J., Riedel U., Arlt C.: Strengthening fibre/matrix interphase by fibre surface modification and nanoparticle incorporation into the matrix. Composites Science and Technology, **74**, 60–66 (2013).
DOI: 10.1016/j.compscitech.2012.10.004

[25] Sae-oui P., Sirisinha C., Intiya W., Thaptong P.: Properties of natural rubber filled with ultrafine carboxylic acrylonitrile butadiene rubber powder. Advances in Polymer Technology, **30**, 183–190 (2011).
DOI: 10.1002/adv.20215

[26] Kinloch A. J., Maxwell D. L., Young R. J.: The fracture of hybrid-particulate composites. Journal of Materials Science, **20**, 4169–4184 (1985).
DOI: 10.1007/BF00552413

[27] Lee J., Yee A. F.: Role of inherent matrix toughness on fracture of glass bead filled epoxies. Polymer, **41**, 8375–8385 (2000).
DOI: 10.1016/S0032-3861(00)00186-5

[28] Williams J. G.: Particle toughening of polymers by plastic void growth. Composites science and technology, **70**, 885–891 (2010).
DOI: 10.1016/j.compscitech 2009.12.024

[29] Kawaguchi T., Pearson R. A.: The effect of particle–matrix adhesion on the mechanical behavior of glass filled epoxies. Part 2. A study on fracture toughness. Polymer, **44**, 4239–4247 (2003).
DOI: 10.1016/S0032-3861(03)00372-0

[30] Zamanian M., Mortezaei M., Salehnia B., Jam J. E.: Fracture toughness of epoxy polymer modified with nanosilica particles: Particle size effect. Engineering Fracture Mechanics, **97**, 193–206 (2013).
DOI: 10.1016/j.engfracmech.2012.10.027

[31] Norman D. A., Robertson R. E.: Rigid-particle toughening of glassy polymers. Polymer, **44**, 2351–2362 (2003).
DOI: 10.1016/S0032-3861(03)00084-3

[32] Huang Y., Kinloch A. J.: The role of plastic void growth in the fracture of rubber-toughened epoxy polymers. Journal of Materials Science Letters, **11**, 484–487 (1992).
DOI: 10.1007/BF00731112

[33] Bai S. L., Djafari V., Andréani M., François D.: *In situ* study of short-beam shear tests for composite materials. Composites Science and Technology, **55**, 343–348 (1995).
DOI: 10.1016/0266-3538(95)00077-1

[34] Wisnom M. R., Reynolds T., Gwilliam N.: Reduction in interlaminar shear strength by discrete and distributed voids. Composites Science and Technology, **56**, 93–101 (1996).
DOI: 10.1016/0266-3538(95)00128-X

[35] Singh S., Partridge I. K.: Mixed-mode fracture in an interleaved carbon-fibre/epoxy composite. Composites Science and Technology, **55**, 319–327 (1995).
DOI: 10.1016/0266-3538(95)00062-3

[36] Díez-Pascual A. M., Naffakh M., Gonzalez-Domínguez J. M., Ansón A., Martínez-Rubi Y., Martínez M. T., Simard B., Gómez M. A.: High performance PEEK/carbon nanotube composites compatibilized with polysulfones-I. Structure and thermal properties. Carbon, **48**, 3485–3499 (2010).
DOI: 10.1016/j.carbon.2010.05.046

[37] Siddiqui N. A., Woo R. S., Kim J-K., Leung C. C., Arshad M.: Mode I interlaminar fracture behavior and mechanical properties of CFRPs with nanoclay-filled epoxy matrix. Composites Part A: Applied Science and Manufacturing, **38**, 449–460 (2007).
DOI: 10.1016/j.compositesa.2006.03.001

[38] Grabr H. M., Abd Elrahamn M., Okubo K., Fujii T.: Interfacial adhesion improvement of plain woven carbon fiber reinforced epoxy filled with micro-fibrillated cellulose by addition liquid rubber. Journal of materials science, **45**, 3841–3850 (2010).
DOI: 10.1007/s10853-010-4439-y

[39] Ozdemir N. G., Zhang T., Hadavinia H., Aspin I., Scarpa F.: Glass fibre reinforced polymer composites toughened with acrylonitrile butadiene nanorubber. Composites Part B: Engineering, **88**, 182–188 (2015).
DOI: 10.1016/j.compositesb.2015.09.004

eXPRESS Polymer Letters Vol.10, No.5 (2016) 408–419
Available online at www.expresspolymlett.com
DOI: 10.3144/expresspolymlett.2016.38

Characterisation of macrogel composition from industrial natural rubber samples: Influence of proteins on the macrogel crosslink density

S. Rolere[1], *C. Bottier*[2], *L. Vaysse*[2], *J. Sainte-Beuve*[1], *F. Bonfils*[1*]

[1]CIRAD, UMR IATE, F-34060 Montpellier, France
[2]CIRAD, UMR IATE, Kasetsart University, Bangkok, Thailand

Received 13 October 2015; accepted in revised form 7 December 2015

Abstract. The insoluble (macrogel) and soluble fractions of 11 commercial natural rubber (NR) samples (Technically specified rubber) were separated. Nitrogen titrations and lipid extractions enabled a quantitative assessment of the proteins and extractable lipids in each fraction. Swelling was measured in tetrahydrofuran in order to evaluate the crosslink density (M_c^{-1}) of each macrogel. While the soluble fraction had a high lipid concentration, the majority of non-isoprene compounds of the macrogel were found to be proteins, which accounted for 4.6 to 50.8% (w/w) of the macrogel. Indeed, the macrogels contained less than 0.5% (w/w) extractable lipids. However, our results showed that the soluble fraction contained large quantities of proteins (16–66% of the nitrogen content of the raw NR sample), probably structuring microaggregates. An exponential correlation ($R^2 > 0.96$) was found between the crosslink density and the protein concentration of macrogel, suggesting that proteins are involved in the majority of crosslinks in macrogel.

Keywords: *polymer gels, natural rubber, macrogel, proteins, crosslink density*

1. Introduction

Natural rubber (NR) is made from the latex of *Hevea brasiliensis*, and accounts for 42% of global elastomer consumption [1]. Most of global NR production (70% of 12.1 million tons) is used by the tyre industry. Depending on the applications, several commercial grades can be used including technically specified rubbers (TSR, >60% of global production), ribbed-smoked sheets (RSS, ~20%) and concentrated latex (~12%). The green side of this biopolymer is disadvantaged by the variability (or non-consistency) of its properties, which generates losses of materials and energy during the various stages of industrial processes [2]. In this article, our main objective was to gain a better understanding of variability in the composition and structure of macrogel fractions from very diverse industrial samples.

NR is composed of about 94% (w/w) *cis*-1,4-polyisoprene [3, 4] and displays some outstanding mechanical properties, compared to synthetic rubbers [2, 5]. Its exceptional properties are attributed to the stereoregularity of the polyisoprene chain (high *cis*-1,4 content), high polyisoprene molar masses [6–8], but also to the presence of a gel phase [9, 10]. This gel phase is composed of an insoluble fraction called 'macrogel' [11, 12], and of microaggregates dispersed in the soluble fraction, called 'microgel' [13, 14] (Figure 1). Some non-isoprene compounds of NR, such as lipids (1.5–4% w/w) [4, 15–17], proteins (1–3.5% w/w) [4, 17–19], and minerals (0.2% w/w) [4, 20], are assumed to be responsible for the existence of this gel phase. For example, macrogel can be eliminated by transesterification or deproteinization of NR. Consequently, Tanaka and cowork-

*Corresponding author, e-mail: frederic.bonfils@cirad.fr
© BME-PT

ers [21, 22] suggested the presence of esterified compounds, such as phospholipids, covalently bonded to the α-terminal group of the macromolecule. The authors also suggested physical interactions between proteins and the ω-terminal group of the polymer [21]. Nevertheless, the role of each non-isoprene compound, as well as the nature of the terminal groups of the *cis*-1,4-polyisoprene chains of NR, is still unclear.

The amounts of gel present in NR samples are usually quantified after dissolution in organic solvents, such as toluene or tetrahydrofuran [23–25] (Figure 1). After dissolution, macrogel is eliminated by centrifugation. Filtration of the soluble fraction can then be used to quantify the microgel either directly by weighing the recovered microgel [25], or indirectly using SEC-MALS (size exclusion chromatography, multiple angle light scattering) analyses [12, 26]. Several studies showed that proteins are concentrated in the macrogel of NR [27–29]. Proteins are known to be insoluble in the organic solvents used for NR dissolution. Consequently, proteins not involved in the structure of macrogel could also precipitate with the macrogel during the centrifugation step (Figure 1). Thus, the high protein contents of macrogel cannot be directly used to study the role of those non-isoprene compounds in macrogel structuring. Indeed, earlier work showed that washing macrogel with water, helped to eliminate non-structuring minerals and proteins [30].

In order to gain a better understanding of variability in the composition and structure of macrogel fractions from very diverse industrial samples, macrogels extracted from 11 different NR industrial samples were characterized. The protein content and lipid composition of the respective washed macrogels and soluble fractions were investigated, using chemical analyses and FT-IR (Fourier transform infrared) spectroscopy. The crosslink density of each macrogel sample was also estimated by swelling measurements. Lastly, the effect of non-isoprene compound concentrations on macrogel structure was investigated.

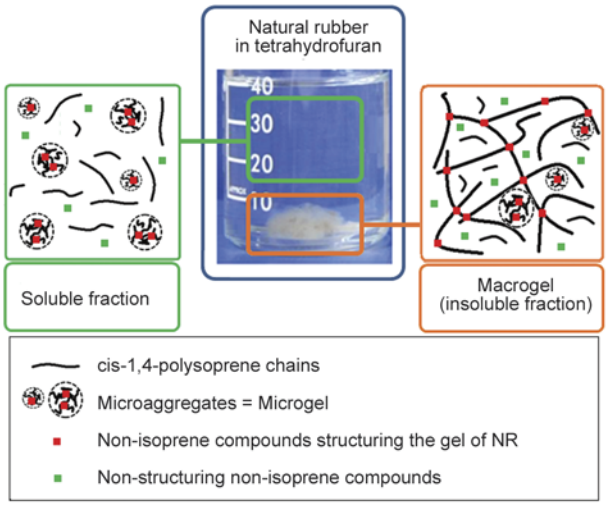

Figure 1. Diagram of the insoluble (macrogel) and soluble fractions present in a solution of natural rubber dissolved at 0.1% (w/v) in tetrahydrofuran

2. Experimental section

2.1. Materials

Eleven commercial NR samples of TSR10, TSR10CV and TSR3CV grades were produced in Côte d'Ivoire, Thailand and Vietnam, under controlled conditions (Table 1). TSR (Technically specified rubber) grades account for more than 60% of global NR production. Usually, commercial NRs are made with a mixture of fresh latex (TSR3CV grade), or coagula

Table 1. Characteristics of the 11 natural rubber samples

Sample	Grade	Clone	Country	Age [months] of sample before analysis*	Macrogel [% w/w]
A	TSR10	GT1	Côte d'Ivoire	26	14.0
B	TSR10	GT1	Côte d'Ivoire	22	15.4
C	TSR10	RRIM600	Thailand	14	25.7
D	TSR10	RRIM600	Thailand	14	20.8
E	TSR10	GT1	Côte d'Ivoire	26	5.2
F	TSR10CV	GT1	Côte d'Ivoire	30	4.7
G	TSR10CV	GT1	Côte d'Ivoire	30	2.1
H	TSR10	PB235	Côte d'Ivoire	30	1.3
I	TSR10	GT1	Côte d'Ivoire	30	2.8
J	TSR3CV	GT1	Vietnam	32	3.6
K	TSR3CV	GT1	Vietnam	32	1.6

*To work on stable sample, as several papers showed storage hardening reachs a plateau after about 10–14 months, most of the samples were used after at least 14 months of storage.

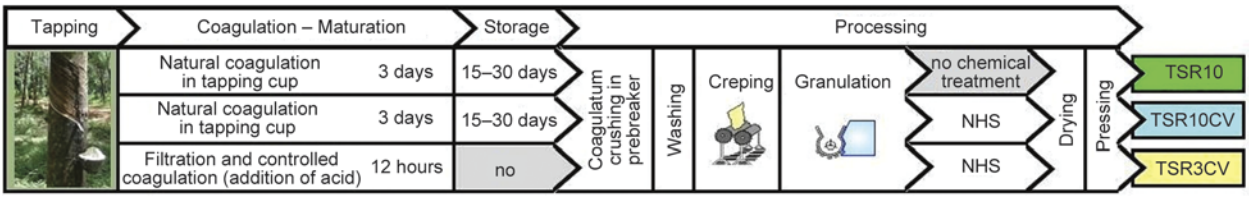

Figure 2. Diagram of the processing conditions used to prepare TSR10, TSR10CV and TSR3CV grades (reprinted from [17], by courtesy of Elsevier)

(TSR10 and TSR10CV grades), from different *Hevea brasiliensis* genotypes or clones (Figure 2). However, in our study, each NR sample was made from the latex of a single clone (GT1, RRIM600 or PB235) in order to remove variability linked to the clonal origin of the latex [11, 12, 31]. The properties of the TSR3CV and TSR10CV samples were stabilized with a neutral hydroxylamine sulfate solution (NHS; Figure 2).

All samples were analysed at least 14 months after their production. Indeed, NR samples harden during storage because of the generation of macrogel [32, 33]. It was shown that this phenomenon of storage hardening reached a plateau after about 10 to 14 months of storage according the NR grade [32, 33].

Before analysis, each sample was homogenized according to standards ISO 1795 and ISO 2393, on a BLERE I.F. 50 #1400 two-roll mill (51/64 model) (Paris, France). The roll temperature was maintained at 27 °C and the nip was 1.69 mm. The speeds of the front and back rolls were 24 and 34 rpm, respectively.

2.2. Separation of the soluble fraction and macrogel

Homogenized NR samples were dissolved at 0.5% (w/v) in tetrahydrofuran (THF, HPLC grade) stabilized with 250 mg/L of 2,6-di-tert-butyl-4-methylphenol (BHT) and filtered at 0.2 µm. The solutions were kept at 30 °C in the dark in a thermoregulated water bath. After 5 days, the soluble fraction and macrogel were separated by centrifugation at 30 000 g (Beckman Coulter Avanti J-E centrifuge, Paris, France) for 1 hour at 20 °C. The upper soluble fraction was recovered and the macrogel (bottom fraction) was diluted 4 times in stabilized THF, then kept at 30 °C in the dark for a further 2 days. The solutions were then centrifuged under the same conditions as described above. The macrogel was recovered and washed once with ultrapure water containing 5% (w/v) of sodium dodecyl sulfate (SDS), then washed three times with ultrapure water in order to remove non-structuring compounds precipitated with the macrogel during centrifugation [30]. After solvent evaporation, both the soluble fraction and the macrogel were finally dried at 30 °C under vacuum for 2 hours. The macrogel content was quantified by gravimetry.

2.3. Physico-chemical characterization

2.3.1. FT-IR spectroscopy

Sheets around 1.6 mm thick and with minimum roughness were prepared from homogenized samples on the same two-roll mill used for rubber homogenization. The roll temperature was maintained at 27 °C and the nip was set to the minimum (0.5 mm). The speeds of the front and back rolls were 27.5 and 38.5 rpm, respectively.

FT-IR spectra were recorded on these rubber sheets with OPUS 7.0 software on a Bruker Tensor27 spectrometer (Paris, France), using the Attenuated Total Reflection (ATR) mode, in the range of 4000–400 cm^{-1} with a resolution of 2 cm^{-1} [17]. The background was measured before testing each sample. For each sample, five spectra were recorded on five different random zones of the rubber sheet. Each spectrum was obtained from 16 successive scans. Firstly, H_2O/CO_2 compensation was carried out in order to overcome signals caused by atmospheric conditions in the 2400–1800 cm^{-1} domain. The baseline was subtracted using a rubber band correction method. A mean spectrum was then calculated from the initial five spectra. Normalization of the FT-IR spectra was performed using the maximum absorbance of the **=C–H** out-of-plane bending band (840 cm^{-1}), corresponding to the isoprene monomer, as previously described [17].

2.3.2. Nitrogen contents

Nitrogen titration is usually performed to assess the protein content of NR samples [17, 34]. The Dumas method was used to determine nitrogen contents. About 600 mg of each homogenized sample was

calcined at 1100 °C under oxygen flow. Combustion gases were trapped in order to separate nitrogen oxides from dust, water vapour, halogen compounds and carbon oxides. Nitrogen oxides were reduced to N_2 at 700 °C under helium flow, on a copper column. The nitrogen content was then measured by catharometry, after calibration with well-known molecules such as EDTA, on a LECO Trumac N analyser (Paris, France). Three independent measurements were performed for each sample.

2.3.3. Lipid characterization

Lipid extractions were carried out according to the method given in Liengprayoon *et al*. [35]. Homogenized samples (~2.8 g) were ground in liquid nitrogen and lipids were extracted with a chloroform: methanol mixture (2:1 v/v; 50 mL) for six hours at room temperature. NR residues were removed by filtration and the solutions were evaporated to dryness. Extracts were redissolved in 4 mL of chloroform:methanol mixture (2:1; v/v). Water soluble components were removed by adding 1 mL of a 0.9% NaCl solution. After decantation, the lipid-containing bottom fraction was taken and evaporated to dryness to obtain the lipid extract. The lipid extracts were expressed on a dry rubber basis. Three extraction replications were performed for the raw NR samples and their respective soluble fraction. For the macrogels, a single measurement was carried out because the quantity of the test sample was insufficient.

Neutral lipids were characterized using high performance thin layer chromatography (HPTLC). Ten micrograms of the total lipid extract was deposited on a Merck silica gel 60 F254 TLC plate (100×200 mm) using a CAMAG Automatic TLC Sampler 4 (Muttenz, Switzerland). Elution was performed with an n-Hexane:diethyl ether:acetic acid mixture (80:20:1 v/v/v). Development was carried out using a mixture of 40% orthophosphoric acid with saturated copper acetate aqueous solution in a ratio of 1:1 (v/v), followed by heating at 180 °C for 10 minutes. β-sitosterol, oleic acid, γ-tocotrienol, triolein and cholesteryl stearate standards were used for identification.

2.3.4. Swelling measurements

Swelling measurements were carried out for each extracted macrogel, in order to estimate its crosslink density, using the Flory-Rehner equilibrium swelling equation [36]. Three independent measurements were taken for each sample. About 60 mg of macrogel ($m_{MG,0}$) was placed in 30 mL of stabilized and filtered THF. The solution was kept at 30 °C in the dark. After 8 days, the swollen macrogel was separated from the soluble fraction with a spatula, then weighed ($m_{swollen\ MG}$). Centrifugation was avoided to not modify the swelling degree of the sample. After THF evaporation, the recovered macrogel was finally dried at 30 °C under vacuum for 2 hours, then weighed ($m_{dry\ MG}$).

3. Results and discussion

3.1. Macrogel contents

The macrogel was separated by centrifugation from the soluble fraction for 11 NR samples, and then washed in order to eliminate non-structuring non-isoprene compounds [30]. The final recovered quantities of washed macrogel are given in Table 1. Macrogel was found to range from 1.3% (w/w; sample H: TSR10 from PB235 latex) to 25.7% (w/w; sample C: TSR10, RRIM600) depending on the NR sample. An influence of the grade was highlighted. Indeed, samples with high macrogel contents (14.0-25.7% w/w) were all from TSR10 samples [37]. On the other hand, stabilized rubbers with controlled viscosity (CV: TSR3CV and TSR10CV grades) were found to have low macrogel contents (1.6–4.7% w/w). These results illustrate the influence of the neutral hydroxylamine sulfate (NHS) used for stabilizing these grades (Figure 2). Stabilized rubbers are less susceptible to storage hardening, unlike TSR10 samples. Storage hardening is known to increase the gel content of NR samples [6, 38]. Nevertheless, it is worth mentioning that 3 TSR10 samples (E, H and I; Table 1) were found to have low macrogel contents (1.3–5.2% w/w), comparable to values of CV grades.

3.2. Protein quantification

The nitrogen atoms of NR samples mainly come from proteins and polypeptides. The nitrogen content of each sample was measured by the Dumas method, in order to estimate its protein content (Table 2). Firstly, the soluble fractions were found to have lower nitrogen contents (0.05–0.19% w/w) than the corresponding raw NR samples (0.21–0.50% w/w). On the other hand, the washed macrogels were much more concentrated in nitrogen atoms than the raw NR samples. Indeed, the nitrogen con-

Table 2. Nitrogen content of the 11 selected NR samples and their respective soluble fraction and macrogel, measured with the Dumas method (Sol – Soluble fraction; MG – Macrogel. Values in brackets are the standard deviations obtained from 3 independent measurements. Material balances were calculated from the macrogel amounts. Sol [%] = 100 – MG [%]. The protein concentrations (W_P) of the macrogel samples were calculated considering that nitrogen accounts for 16% (w/w) of the proteins.)

Sample	Grade – Clone	Macrogel amount [% w/w]	Nitrogen content [% w/w]			Nitrogen balance			Protein concentration (W_P) in MG [% w/w]
			Raw NR	Sol	MG	Sol	MG	Lost nitrogen	
A	TSR10 – GT1	14.0	0.296 (0.002)	0.122 (0.002)	1.181 (0.019)	35.4%	55.8%	–8.8%	7.38 (0.12)
B	TSR10 – GT1	15.4	0.278 (0.006)	0.057 (0.002)	0.909 (0.029)	17.3%	50.3%	–32.4%	5.68 (0.18)
C	TSR10 – RRIM600	25.7	0.254 (0.006)	0.055 (0.003)	0.743 (0.014)	16.2%	75.2%	–8.6%	4.64 (0.09)
D	TSR10 – RRIM600	20.8	0.298 (0.007)	0.062 (0.014)	1.170 (0.025)	16.4%	81.7%	–1.9%	7.31 (0.16)
E	TSR10 – GT1	5.2	0.293 (0.002)	0.165 (0.013)	2.216 (0.177)	53.3%	39.3%	–7.4%	13.9 (1.1)
F	TSR10CV – GT1	4.7	0.269 (0.011)	0.118 (0.021)	2.191 (0.071)	41.8%	38.2%	–20.0%	13.7 (0.44)
G	TSR10CV – GT1	2.1	0.336 (0.009)	0.194 (0.012)	4.391 (0.204)	56.6%	27.4%	–16.0%	27.4 (1.3)
H	TSR10 – PB235	1.3	0.208 (0.002)	0.139 (0.041)	3.717 (0.196)	65.9%	23.3%	–10.8%	23.2 (1.2)
I	TSR10 – GT1	2.8	0.332 (0.008)	0.180 (0.011)	5.228 (0.185)	52.6%	44.1%	–3.3%	32.7 (1.2)
J	TSR3CV – GT1	3.6	0.436 (0.004)	0.128 (0.003)	5.935 (0.040)	28.3%	49.0%	–22.7%	37.1 (0.25)
K	TSR3CV – GT1	1.6	0.496 (0.008)	0.129 (0.001)	8.121 (0.152)	25.6%	26.2%	–48.2%	50.8 (0.95)

tents of the 11 macrogels were between 0.74% and 8.12% (w/w). These concentrations correspond to protein contents (W_P) of 4.6 to 50.8% (w/w), calculated with a conventional value of 16% (w/w) of nitrogen atoms in proteins (Table 2). It is worth noting that the 2 macrogels with the highest nitrogen contents (Samples J and K: 5.94–8.12% w/w) were extracted from the 2 TSR3CV samples. Otherwise, the 4 macrogels with the lowest nitrogen contents (Samples A-D: 0.74–1.18% w/w) came from the TSR10 samples with high macrogel contents (Table 2).

These results confirmed that proteins are highly concentrated in the macrogel of NR, during the centrifugation step, in accordance with the literature [27–29]. However, it is important to note that most of the proteins in the raw NR sample were not always found in the macrogel (Table 2). In fact, only 4 of the 11 macrogels accounted for more than 50% of the initial nitrogen atoms contained in the raw NR samples. Moreover, the nitrogen concentrations measured for the soluble fractions were far from negligible. For example, in the case of sample H (TSR10, PB235), only 23% of the initial nitrogen atoms were found in the macrogel, while the soluble fraction accounted for 66% of the initial nitrogen atoms. As it is known that microgel remains in the soluble fraction, it can be assumed that the proteins found in the soluble fraction take part in structuring microaggregates. It should be noted that material losses were calculated and accounted for 2 to 48% of the initial nitrogen atoms contained in the raw NR samples (Table 2). Those nitrogen losses were attributed to non-structuring proteins, eliminated during the macrogel washing steps, as reported previously [30]. The remaining proteins contained in the washed macrogels were not eliminated during the washing steps, and were assumed to participate in macrogel structuring. No correlation was found between the macrogel content and the nitrogen content of the raw NR samples.

FT-IR spectroscopy in ATR configuration can be used to quickly characterize NR samples, and to estimate some non-isoprene compound concentrations [17]. Proteins show characteristic vibration bands at 3283 cm^{-1} (ν**N–H**), 1630 cm^{-1} (Amide I: ν-(**C=O**)NH–) and 1541 cm^{-1} (Amide II: β**N–H** + ν**C–N**). Figure 3 shows the normalized FT-IR spectra of a TSR10 sample made from GT1 latex (Sample I) and of its respective soluble fraction and washed macrogel. The maximum normalized absorbances of the amide vibration bands (1630 and 1541 cm^{-1}) were found to be more than 15 times higher for the macrogel sample, compared to the raw NR sample and the soluble fraction. These two amide bands were previously correlated to the nitrogen content of raw NR samples [17]. It is interesting to note that these correlations also existed for the macrogel samples (Figure 4). Indeed, the maximum normalized absorbance of the amide I vibration band (1630 cm^{-1}) increased linearly with the nitrogen content (R^2 = 0.97) of the studied macrogels, except for the one extracted from sample K.

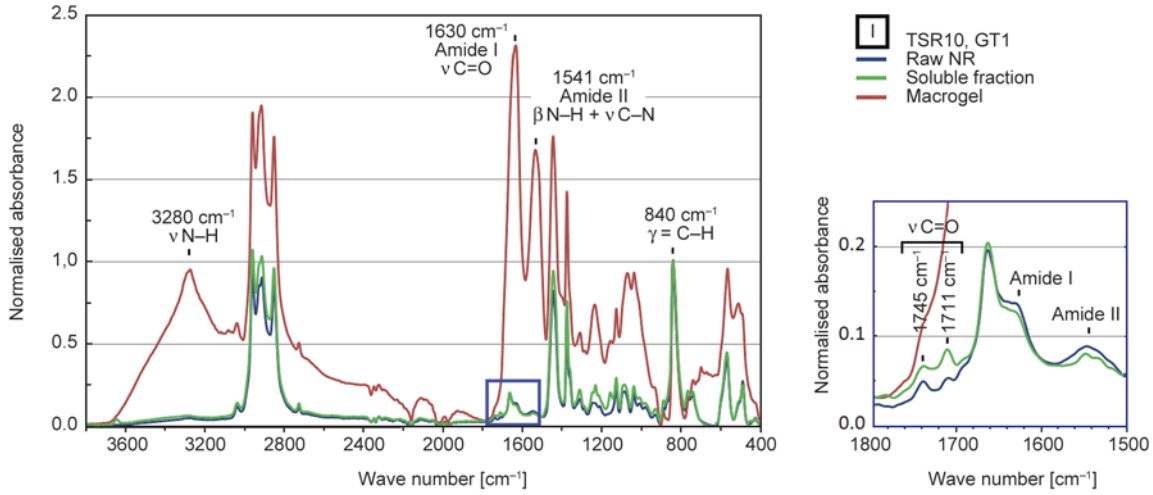

Figure 3. Normalized FT-IR spectra of a TSR10 sample made from the latex of clone GT1 (Sample I) and of its separated soluble fraction and washed macrogel

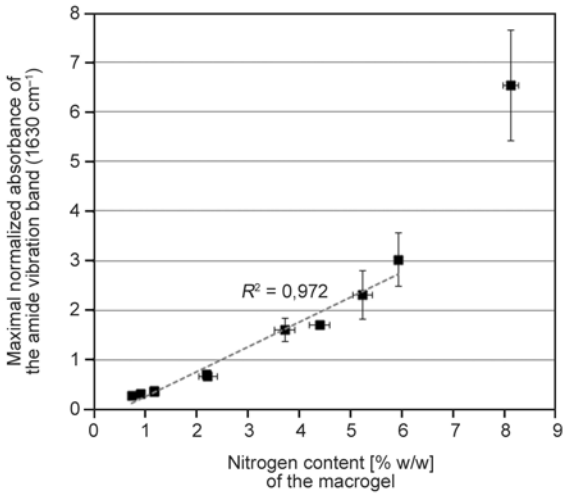

Figure 4. Evolution of the maximum absorbance of the amide I vibration band (1630 cm^{-1}) normalized by the maximum absorbance of the *cis*-1,4-isoprene band (840 cm^{-1}), with the nitrogen content of the washed macrogels. The macrogel with the highest nitrogen content (Sample K, N: 8.12% w/w) was not taken into account in the linear model.

For this sample, containing the highest nitrogen content (8.12% w/w, Table 2), normalization with the maximum absorbance of the *cis*-1,4-isoprene monomer (840 cm^{-1}) could be inappropriate.

3.3. Lipid characterization

Lipids of NR samples can also be studied using FT-IR spectroscopy. Esterified lipids and free fatty acids (carboxylic acids) show intense carbonyl stretching bands in the 1748-1738 cm^{-1} domain (ν-(**C=O**)OR) and at 1710 cm^{-1} (ν-(**C=O**)OH), respectively [17]. For all samples, the maximum normalized absorbances of the respective lipid bands (esters: 1748–1738 cm^{-1}; carboxyls: 1710 cm^{-1}), were higher for the soluble fraction than for the raw NR sample, indicating that lipids were probably concentrated in the soluble fraction during NR dissolution (Figure 3). On the other hand, no distinct ester or carboxyl band was observable for the majority of the macrogel samples. However, the high amide vibration bands may have masked the other carbonyl stretching bands and lipids might yet be present in the macrogel composition.

Lipids were extracted for two TSR10 samples with large amounts of macrogel (Samples A and C) and for their respective soluble fraction and washed macrogel, according to the method given by Liengprayoon *et al*. [35]. The selected samples A and C were made from the latex of clones GT1 and RRIM600, respectively (Table 1). The quantity of extractable lipids in the two raw NR samples was found to account for 2.63% (A: GT1) and 2.09% (C: RRIM600) of the material weight (Table 3). NR samples from RRIM600 latex usually have lower lipid extracts [16, 17]. The lipid extract was higher for the soluble fractions (A: 5.25% w/w; C: 5.53% w/w), while both macrogels showed much lower extracts, between 0.51% (A) and 0.58% w/w (C). These observations tallied well with the FT-IR spectra (Figure 3) and indicated a concentration of the lipid molecules in the soluble fraction of NR samples.

Material balances were calculated by using the respective proportion of each fraction (soluble fraction and macrogel) in the corresponding raw NR sample (Table 3). A clear overage of extracted material was highlighted for both soluble fractions. In fact, the lipid extracts of the two soluble fractions amounted

Table 3. Lipid extract of two TSR10 samples made from the latex of clones GT1 (A) and RRIM600 (C), and of their respective soluble fraction and macrogel (Sol – Soluble fraction; MG – Macrogel. Values in brackets are the standard deviations obtained from 3 independent measurements. Material balances were calculated from the macrogel amounts. Sol [%] = 100 – MG [%].)

Sample	Grade – Clone	Macrogel amount [% w/w]	Lipid extract [% w/w]			Material balance		
			Raw NR	Sol	MG	Sol	MG	Overage
A	TSR10 – GT1	14.0	2.63 (0.11)	5.25 (0.49)	0.51 –	172%	3%	74%
C	TSR10 – RRIM600	25.7	2.09 (0.08)	5.53 (0.22)	0.58 –	197%	7%	104%

to between 172% (A: GT1) and 197% (C: RRIM600) of the lipid extracts of the raw NR samples. Simultaneous extraction of *cis*-1,4-polyisoprene chains might explain these overages.

Each lipid extract was then characterized using HPTLC, with a mobile phase optimized for the elution of neutral lipids which are known to account for 83–86% of the total lipids of NR [16]. A calibration with well-known lipid standards was used to identify some substances (Figure 5). Both raw NR samples (A: GT1; C: RRIM600) showed the same neutral lipid composition. Free sterols (R_f = 0.15) were identified for the two samples. Unidentified substances with an R_f value of 0.06 were also found. Several free fatty acids (FFAs) were identified: at least two bands with an R_f value close to that of oleic acid (C18:1; R_f = 0.21) were attributed to furan fatty acids (FuFAs; R_f = 0.19) and to other FFAs (R_f = 0.22) [16]. γ-tocotrienol (R_f = 0.30) was also found. Substances with an R_f value between γ-tocotrienol (R_f = 0.30) and triolein (R_f = 0.57) may have been α-tocotrienol or triglycerides. Those bands showed low intensity, according to previous observations carried out on TSR10 samples [17]. Lastly, some other bands with an R_f value over 0.90 were attributed to esterified tocotrienols and esterified sterols [16].

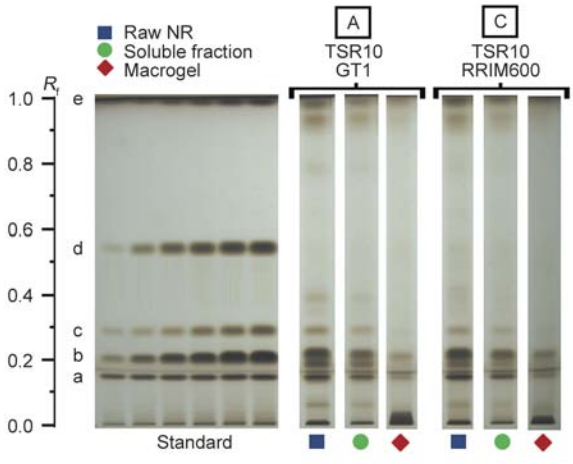

Figure 5. HPTLC analyses of the lipid extracts obtained from two TSR10 samples made from the latex of clones GT1 (A) and RRIM600 (C), and from their respective soluble fraction and macrogel, using standard calibrations: β-sitosterol (a); oleic acid (b); γ-tocotrienol (c); triolein (d); cholesteryl stearate (e)

All the substances identified in the raw NR samples were also found in the lipid extracts of both soluble fractions (Figure 5). Nevertheless, for the soluble fractions, the neutral lipid bands showed lower intensities, indicating lower concentrations in the corresponding lipid extracts. This result supports the idea of co-extraction of *cis*-1,4-polyisoprene during lipid extraction, leading to an overestimation of the lipid extract. In fact, the share of extractable lipids in the soluble fractions was probably lower than 5.25–5.53% w/w. On the other hand, the HPTLC analyses of the two macrogel lipid extracts revealed very few bands (Figure 5), corresponding to free sterols (R_f = 0.15) and to FFAs (R_f = 0.22). The previous esterified substances (triglycerides, esterified tocotrienols and esterified sterols) were not detected for either macrogel. It is important to note the existence of high concentrations of polar substances (R_f < 0.04) in the macrogel lipid extracts. These substances could be attributed to polar lipids but also to hydrophobic proteins, co-extracted with the lipids and not eliminated during the Folch-wash step. The presence of those polar substances indicated that the extractable neutral lipids contained in both macrogels might amount to less than 0.51% (A: GT1) and 0.58% (C: RRIM600).

It needs to be remembered that for these two macrogels the measured nitrogen contents were 1.18% (w/w; A: GT1; Table 2) and 0.74% (w/w; C: RRIM600), corresponding to protein concentrations of about 7.4 and 4.6% (w/w), respectively. Consequently, the quantities of extractable lipids were clearly much lower than the proteins in these two samples. Moreover, the two macrogels were among those with the lowest protein concentrations (Table 2).

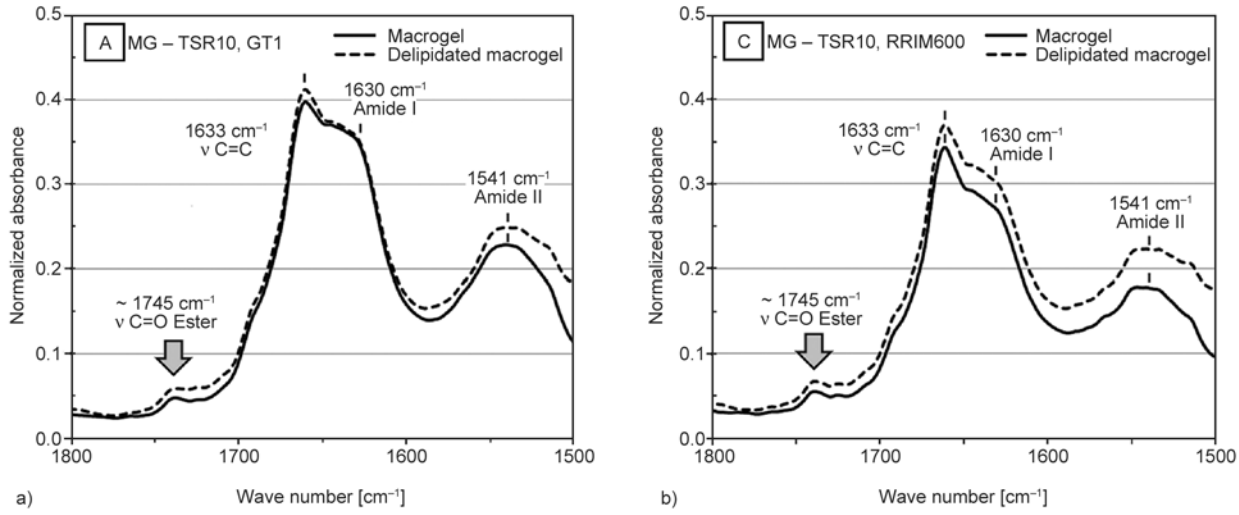

Figure 6. Normalized FT-IR spectra of the macrogels of two TSR10 samples made from latex of clones GT1 (a) and RRIM600 (b), before and after lipid extraction

For all macrogels, the share of extractable lipids could probably be neglected compared to the protein concentrations, which were estimated to be 4.6 to 50.8% (w/w). The role of proteins in macrogel structuring is probably predominant. However, it is worth noting that the method given by Liengprayoon *et al*. [35] can only be used to study extractable lipids. Non-extractable esters [17] might partly be responsible for the associative structure of NR, as suggested by Tanaka and coworkers [21, 22]. FT-IR characterization of the two macrogels showed the presence of non-extractable esters (Figure 6). A calibration curve obtained with mixtures of synthetic *cis*-1,4-polyisoprene (Nipol IR2200, Zeon Chemicals) with well-known amounts of methyl stearate [17], enabled an estimation of those non-extractable esters, which were found to amount to 4.5 (sample A) and 9.0 mmol/kg (sample C) in the macrogels.

3.4. Role of proteins in the crosslink density of the macrogels

Swelling was also measured for the 11 washed macrogels, in order to evaluate their respective crosslink density [36]. The change in weight of the swollen macrogel after drying was first used to calculate the swelling degree of the *cis*-1,4-polyisoprene fraction (Q_{PI}) of the macrogel (Equation (1)). In this model, the proteins of the macrogel, which were assumed to account for the majority of the non-isoprene compounds, were also considered but were unable to swell because of their insolubility in organic solvents. The protein concentrations (W_P) in the washed macrogel (Table 2) were used for this calculation. For the 11 macrogels, the swelling degree of the *cis*-1,4-polyisoprene fraction (Q_{PI}) was found to vary between 6.6 (Sample K: TSR3CV, GT1; Table 4) and 85.7 (Sample A: TSR10, GT1). These values indicate that the volume of THF (V_{THF}) in the swollen macrogels was 6.6 to 85.7 times greater than the volume of the *cis*-1,4-polyisoprene chains (V_{PI}). It is worth mentioning that both macrogels extracted from the two TSR3CV samples (Samples J and K) had the lowest Q_{PI} values (Table 4). On the other hand, the 4 macrogels extracted from samples A to D, which showed high macrogel contents, had the highest Q_{PI} values (Equation (1)):

$$Q_{PI} = \frac{V_{THF}}{V_{PI}} = \frac{m_{\text{swollen MG}} - m_{\text{dry MG}}}{\rho_{THF}} \cdot \frac{\rho_{PI}}{m_{\text{dry MG}} \cdot (1 - W_P)} \quad (1)$$

where Q_{PI} – swelling degree of the *cis*-1,4-polyisoprene fraction, V_{THF} – volume of THF in the swollen macrogel, V_{PI} – volume of *cis*-1,4-polyisoprene in the swollen macrogel, $m_{\text{swollen MG}}$ – weight of the swollen macrogel, $m_{\text{dry MG}}$ – weight of the macrogel after drying, ρ_{THF} – density of THF (0.887 g/cm^3), ρ_{PI} – density of *cis*-1,4-polyisoprene (0.910 g/cm^3), W_P – mass fraction of proteins in the macrogel (Table 2).

The calculated swelling degree (Q_{PI}) was then used to estimate the mean molar mass of *cis*-1,4-polyisoprene between crosslinks (M_c) for each macrogel, using the Flory-Rehner [36] equilibrium swelling equation (Equation (2)). The lowest mean molar mass

of *cis*-1,4-polyisoprene between crosslinks (M_c = 22 kg/mol; Table 4) was measured for the macrogel of sample K (TSR3CV, GT1), indicating that this macrogel was the most crosslinked. Indeed, a M_c value of 22 kg/mol corresponds to only 320 isoprene monomers between crosslinks. On the other hand, the macrogel extracted from sample A (TSR10, GT1) had a M_c value of 1985 kg/mol, corresponding to about 30 000 monomer units, and was the least crosslinked macrogel. The other macrogels showed intermediate M_c values (Table 4). Tangpakdee and Tanaka [34] already calculated the mean molar mass of *cis*-1,4-polyisoprene between crosslinks (M_c) for 3 macrogels extracted from a commercial NR sample and from two films of high-ammonia preserved latex. The authors found M_c values between 730 and 1100 kg/mol. However, they considered that their macrogel was only composed of *cis*-1,4-polyisoprene: they did not take into account the high protein contents (from 4.6 to 50.8% w/w for our samples, Table 2). Our results showed that macrogels extracted from commercial NR samples can be very diverse and more or less crosslinked compared to those studied by Tangpakdee and Tanaka [34]. An influence of the grade was also highlighted: the two macrogels extracted from TSR3CV samples were found to be the most crosslinked, with M_c values of 22 (sample K) and 37 kg/mol (sample J). On the other hand, all the macrogels from TSR10 and TSR10CV showed M_c values over 100 kg/mol (Table 4). The crosslink density (M_c^{-1}) of all macrogels was calculated as the inverse of the mean molar mass of *cis*-1,4-polyisoprene between crosslinks (M_c), and was found to vary between 0.51 (sample A) and 46.6 mmol/kg (sample K; Table 4). This parameter represents the quantity of crosslinks per kilogram of *cis*-1,4-polyisoprene.

It should be noted that the quantities of macrogel recovered after swelling were always lower than the initial quantities ($m_{MG,0}$) used for swelling measurements (Table 4). The recovered macrogel accounted for 52.8 to 98.5% of the initial macrogel, indicating the presence of a fraction structured by physical interactions, probably composed of microaggregates. An increase in crosslink density (M_c^{-1}) led to a decrease in the proportion of soluble fraction in the studied macrogel (Equation (2)):

$$M_c = \rho_{PI} \cdot V_0 \cdot \frac{0.5 \cdot v_{PI} - \sqrt[3]{v_{PI}}}{\ln(1 - v_{PI}) + v_{PI} + \chi v_{PI}^2} \quad (2)$$

where M_c – mean molar mass of *cis*-1,4-polyisoprene between crosslinks in the macrogel, ρ_{PI} – density of *cis*-1,4-polyisoprene (0.910 g/cm^3), V_0 – molar volume of THF (81.30 cm^3/mol), χ – NR – THF interaction parameter (0.442) [39], v_{PI} – volume fraction of *cis*-1,4-polyisoprene in the swollen macrogel (Equation (3)):

$$\frac{1}{v_{PI}} = \frac{V_{THF} + V_{PI} + V_P}{V_{PI}} = Q_{PI} + 1 + \frac{W_P \cdot \rho_{PI}}{(1 - W_P) \cdot \rho_P} \quad (3)$$

where v_{PI} – volume fraction of *cis*-1,4-polyisoprene in the swollen macrogel, V_{THF} – volume of THF in the swollen macrogel, V_{PI} – volume of *cis*-1,4-poly-

Table 4. Evaluation of the crosslink density (M_c^{-1}) of different macrogels extracted from 11 NR samples, using swelling measurements (Values in brackets are the standard deviations obtained from 3 independent measurements. For each column, values with the same letter are not significantly different (p = 0.05).)

Macrogel	Grade – Clone	Recovered macrogel after swelling [% w/w]	Q_{PI} Swelling degree of the *cis*-1,4-polyisoprene fraction (See Equation (1))	M_c [kg/mol] Mean molar mass of *cis*-1,4-polyisoprene between crosslinks (See Equation (2))	Quantity of isoprene units between crosslinks (= M_c/68 g/mol)	Crosslink density [mmol/kg] (= 1/M_c)
A	TSR10 – GT1	52.8 (0.8)	85.7 (6.6) a	1985 (265) a	29196 (3897)	0.51 (0.07)
B	TSR10 – GT1	54.2 (0.9)	73.7 (12.8) a,b	1544 (463) a,b	22703 (6808)	0.69 (0.20)
C	TSR10 – RRIM600	59.6 (1.3)	68.0 (6.7) b	1332 (233) b	19592 (3425)	0.76 (0.12)
D	TSR10 – RRIM600	63.7 (2.0)	63.8 (7.2) b	1193 (234) b	17543 (3469)	0.86 (0.16)
E	TSR10 – GT1	75.1 (1.6)	43.4 (1.4) c	605 (34) c	8891 (499)	1.66 (0.09)
F	TSR10CV – GT1	71.2 (5.6)	39.6 (2.4) c	515 (55) d	7580 (813)	1.96 (0.22)
G	TSR10CV – GT1	80.8 (1.4)	22.0 (1.7) d	181 (26) e	2665 (380)	5.59 (0.79)
H	TSR10 – PB235	88.0 (0.9)	19.3 (1.6) d,e	142 (22) e	2082 (328)	7.18 (1.09)
I	TSR10 – GT1	91.0 (0.8)	16.5 (1.3) e	108 (16) e	1583 (228)	9.43 (1.48)
J	TSR3CV – GT1	91.7 (2.1)	9.2 (0.9) f	37 (7) f	548 (96)	27.4 (4.36)
K	TSR3CV – GT1	98.5 (0.4)	6.6 (0.6) f	22 (3) f	320 (51)	46.6 (6.91)

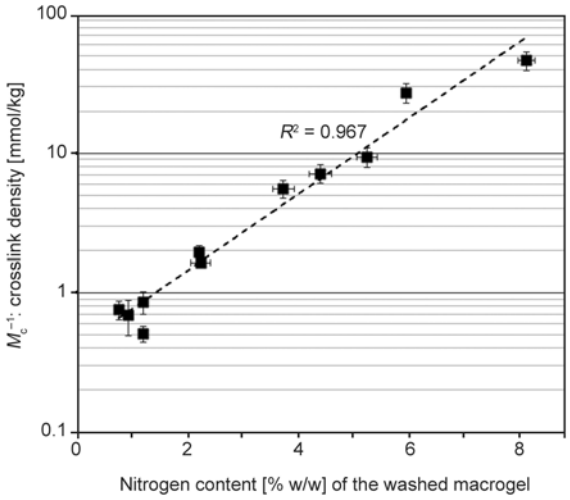

Figure 7. Relation between the nitrogen content of the macrogel and its crosslink density (M_c^{-1}) estimated by swelling measurements

isoprene in the swollen macrogel, V_P – volume of proteins in swollen macrogel, W_P – mass fraction of proteins in the macrogel (Table 2), ρ_{PI} – density of *cis*-1,4-polyisoprene (0.910 g/cm^3), ρ_P – mean density of proteins (1.37 g/cm^3).

Figure 7 shows the changes in crosslink density (M_c^{-1}) for the 11 macrogels, with their respective nitrogen contents measured by the Dumas method. Interestingly, the crosslink density of a macrogel exponentially increases with its protein concentration (R^2 = 0.967). Several studies have already suggested that proteins are partly responsible for the presence of macrogel in NR samples [14, 21]. Our results showed that proteins play a major role in the structuring of a macrogel, and seem to be involved in the majority of crosslinks. The influence of esterified lipids on the presence of macrogel has also been reported [21, 22]. In this paper, we have shown that extractable lipids amounted to less than 0.5% (w/w) for macrogels with low protein concentrations and could be neglected compared to proteins. Nevertheless, non-extractable ester functional groups were found to be present in the studied macrogels (0.13–0.27% w/w; Figure 6), indicating that lipids might play a minor role in macrogel structuring. One way to ensure that these non-extractable esters were from lipids would be to extract them after transesterification.

4. Conclusions

Eleven natural rubber (NR) samples of TSR grades (TSR10, TSR10CV and TSR3CV) made from the latex of 3 different clones (GT1, RRIM600 and PB235) were studied. Their respective macrogel and soluble fraction were separated. The protein content and lipid composition of each fraction were investigated. The majority of the non-isoprene compounds of the macrogel were found to be nitrogen-containing compounds. The protein content was estimated to account for 4.6 to 50.8% of the macrogel weight. Our results also showed that the soluble part contained large quantities of proteins: from 16 to 66% of the protein content of the raw NR sample before fractionation. These proteins were assumed to participate in the structuring of microaggregates present in the soluble fraction. Unlike proteins, very few extractable lipids were found in macrogel, amounting to less than 0.5% (w/w) of the macrogel.

The crosslink density of each macrogel was estimated by swelling measurements. A correlation between the protein contents of the 11 macrogels and their respective protein concentrations was highlighted ($R^2 > 0.96$). NR macrogel structuring was clearly correlated to the amount of proteins, suggesting that proteins are involved in the majority of crosslinks. Moreover, the grade was found to have an influence, as the macrogels extracted from the TSR3CV samples were more crosslinked and also had a higher protein concentration than the macrogels from TSR10 and TSR10CV samples.

Acknowledgements

This work was part of the CANAOPT project, which aims to develop new grades of NR with reduced and controlled variability, for anti-vibration applications. The authors would like to thank the members of the CANAOPT project: Hutchinson, Anvis, Emac, Metaldyne, Michelin, the LRCCP and the Université du Maine. Thanks to our local partners: S.A.P.H. (Côte d'Ivoire), Thai Hua (Thailand) and Dau Tieng Corporation (Vietnam). Thanks to the French public investment bank (BPI), to the French regions and departments of Bourgogne (CR), Pays de la Loire (CR), Languedoc-Roussillon (FEDER), Loiret (CG45), Nièvre (CG58) and Pyrénées-Atlantiques (CG64), and to the Montargis agglomeration for their financial support.

References

[1] International Rubber Study Group: Rubber Statistical Bulletin, April – June 2015 (2015).
[2] Fuller K. N. G.: Rheology of raw rubber. in 'Natural rubber science and technology' (ed.: Roberts A. D.) Oxford University Press, Oxford, 141–176 (1988).
[3] Eng A. H., Tanaka Y.: Structure of natural rubber. Trends in Polymer Science, **3**, 493–513 (1993).

[4] Vaysse L., Bonfils F., Sainte-Beuve J., Cartault M.: Natural rubber. in 'Polymer science: A comprehensive reference polymers for a sustainable environment and green energy' (eds: McGrath J. E., Hickner M. A., Höfer R.) Elsevier, Amsterdam, 281–293 (2012).

[5] Montes S., White J. L.: A comparative rheological investigation of natural and synthetic *cis*-1,4 polyisoprenes and their carbon black compounds. Rubber Chemistry and Technology, **55**, 1354–1369 (1982).
DOI: 10.5254/1.3535934

[6] Li S-D., Yu H-P., Peng Z., Li P-S.: Study on variation of structure and properties of natural rubber during accelerated storage. Journal of Applied Polymer Science, **70**, 1779–1783 (1998).
DOI: 10.1002/(SICI)1097-4628(19981128)70:9<1779::AID-APP16>3.0.CO;2-A

[7] Bonfils F., Flori A., Sainte Beuve J.: Relations between wallace plasticity and M_w for natural rubber. Journal of Applied Polymer Science, **74**, 3078–3087 (1999).
DOI: 10.1002/(SICI)1097-4628(19991220)74:13<3078::AID-APP10>3.0.CO;2-6

[8] Kim C., Morel M-H., Sainte Beuve J., Guilbert S., Bonfils F.: Better characterization of raw natural rubber by decreasing the rotor speed of Mooney viscometer: Role of macromolecular structure. Polymer Engineering and Science, **50**, 240–248 (2010).
DOI: 10.1002/pen.21525

[9] Campbell D. S., Fuller K. N. G.: Factors influencing the mechanical behavior of raw unfilled natural rubber. Rubber Chemistry and Technology, **57**, 104–117 (1984).
DOI: 10.5254/1.3535987

[10] Ehabé E. E., Bonfils F., Aymard C., Akinlabi A. K., Sainte-Beuve J.: Modelling of Mooney viscosity relaxation in natural rubber. Polymer Testing, **24**, 620–627 (2005).
DOI: 10.1016/j.polymertesting.2005.03.006

[11] Subramaniam A.: Characterisation of natural rubber. in 'Proceeding of the international rubber technology conference. Kuala Lumpur, Malaysia' 19–36 (1993).

[12] Bonfils F., Doumbia A., Char C., Sainte-Beuve J.: Evolution in the natural rubber native structure and plasticity retention index from the first tapping of clonal trees. Journal of Applied Polymer Science, **97**, 903–909 (2005).
DOI: 10.1002/app.21845

[13] Voznyakovskii A. P., Dmitrieva I. P., Klyubin V. V., Tumanova S. A.: A dynamic light scattering study of natural rubber in solution. Polymer science Series A: Chemistry, Physics, **38**, 1153–1157 (1996).

[14] Rippel M. M., Leite C. A. P., Lee L-T., Galemberg F.: Direct imaging and elemental mapping of microgels in natural rubber particles. Colloid and Polymer Science, **283**, 570–574 (2005).
DOI: 10.1007/s00396-004-1187-z

[15] Salomez M., Subileau M., Intapun J., Bonfils F., Sainte-Beuve J., Vaysse L., Dubreucq E.: Micro-organisms in latex and natural rubber coagula of *Hevea brasiliensis* and their impact on rubber composition, structure and properties. Journal of Applied Microbiology, **117**, 921–929 (2014).
DOI: 10.1111/jam.12556

[16] Liengprayoon S., Chaiyut J., Sriroth K., Bonfils F., Sainte-Beuve J., Dubreucq E., Vaysse L.: Lipid compositions of latex and sheet rubber from *Hevea brasiliensis* depend on clonal origin. European Journal of Lipid Science and Technology, **115**, 1021–1031 (2013).
DOI: 10.1002/ejlt.201300023

[17] Rolere S., Liengprayoon S., Vaysse L., Sainte-Beuve J., Bonfils F.: Investigating natural rubber composition with Fourier transform infrared (FT-IR) spectroscopy: A rapid and non-destructive method to determine both protein and lipid contents simultaneously. Polymer Testing, **43**, 83–93 (2015).
DOI: 10.1016/j.polymertesting.2015.02.011

[18] Sansatsadeekul J., Sakdapipanich J., Rojruthai P.: Characterization of associated proteins and phospholipids in natural rubber latex. Journal of Bioscience and Bioengineering, **111**, 628–634 (2011).
DOI: 10.1016/j.jbiosc.2011.01.013

[19] Nawamawat K., Sakdapipanich J. T., Ho C. C.: Effect of deproteinized methods on the proteins and properties of natural rubber latex during storage. Macromolecular Symposia, **288**, 95–103 (2010).
DOI: 10.1002/masy.201050212

[20] Tarachiwin L., Sakdapipanich J. T., Tanaka Y.: Gel formation in natural rubber latex: 2. Effect of magnesium ion. Rubber Chemistry and Technology, **76**, 1185–1193 (2003).
DOI: 10.5254/1.3547796

[21] Tanaka Y., Tarachiwin L.: Recent advances in structural characterization of natural rubber. Rubber Chemistry and Technology, **82**, 283–314 (2009).
DOI: 10.5254/1.3548250

[22] Tarachiwin L., Tanaka Y., Sakdapipanich J.: Structure and origin of long-chain branching and gel in natural rubber. Kautschuk Gummi Kunststoffe, **58**, 115–122 (2005).

[23] Allen P. W., Bristow G. M.: The gel phase in natural rubber. Journal of Applied Polymer Science, **7**, 603–615 (1963).
DOI: 10.1002/app.1963.070070217

[24] Kim C., Morel M-H., Sainte Beuve J., Guilbert S., Collet A., Bonfils F.: Characterization of natural rubber using size-exclusion chromatography with online multi-angle light scattering: Study of the phenomenon behind the abnormal elution profile. Journal of Chromatography A, **1213**, 181–188 (2008).
DOI: 10.1016/j.chroma.2008.10.052

[25] Shiibashi T.: Gel structure characterization of NR and IR and direct observation of individual polymer molecules by electron microscopy. International Polymer Science and Technology, **14**, T/33–T/39 (1987).
[26] Wisunthorn S., Liengprayoon S., Vaysse L., Sainte Beuve J., Bonfils F.: SEC-MALS study of dynamic structuring of natural rubber: Comparative study of two *Hevea brasiliensis* genotypes. Journal of Applied Polymer Science, **124**, 1570–1577 (2012).
DOI: 10.1002/app.35099
[27] McMahan C., Kostyal D., Lhamo D., Cornish K.: Protein influences on guayule and *Hevea* natural rubber sol and gel. Journal of Applied Polymer Science, **132**, 42051/1–42051/7 (2015)
DOI: 10.1002/app.42051
[28] Lu F. J., Hsu S. L.: A vibrational spectroscopic analysis of the structure of natural rubber. Rubber Chemistry and Technology, **60**, 647–658 (1987).
DOI: 10.5254/1.3536148
[29] Gregg E. C., Macey J. H.: The relationship of properties of synthetic poly(isoprene) and natural rubber in the factory. The effect of non-rubber constituents of natural rubber. Rubber Chemistry and Technology, **46**, 47–66 (1973).
DOI: 10.5254/1.3545022
[30] Rolere S., Char C., Taulemesse J. M., Bergeret A., Sainte-Beuve J., Bonfils F.: The majority of minerals present in natural rubber are associated with the macrogel: An ICP-MS and SEM/EDX investigation. Journal of Applied Polymer Science, **133**, 43062/1–43062/11 (2016).
DOI: 10.1002/APP.43062
[31] Yip E.: Clonal characterization of latex and rubber properties. Journal of Natural Rubber Research, **5**, 52–80 (1990).
[32] Yunyongwattanakorn J., Sakdapipanich J. T.: Physical property changes in commercial natural rubbers during long term storage. Rubber Chemistry and Technology, **79**, 72–81 (2006).
DOI: 10.5254/1.3547930
[33] Varghese L., Geethakumari M. L., Thomas K. T., Mathew N. M.: Effect of storage on properties of marketable forms of natural rubber: Influence of humidity and temperature. Rubber India, **60**, 39–46 (2008).
[34] Tangpakdee J., Tanaka Y.: Characterization of sol and gel in *Hevea* natural rubber. Rubber Chemistry and Technolology, **70**, 707–713 (1997).
DOI: 10.5254/1.3538454
[35] Liengprayoon S., Bonfils F., Sainte-Beuve J., Sriroth K., Dubreucq E., Vaysse L.: Development of a new procedure for lipid extraction from *Hevea brasiliensis* natural rubber. European Journal of Lipid Science and Technology, **110**, 563–569 (2008).
DOI: 10.1002/ejlt.200700287
[36] Flory P. J., Rehner J.: Statistical mechanics of cross-linked polymer networks II. Swelling. Journal of Chemical Physics, **11**, 521–526 (1943).
DOI: 10.1063/1.1723792
[37] Intapun J., Sainte-Beuve J., Bonfils F., Tanrattanakul V., Dubreucq E., Vaysse L.: Effect of microorganisms during the initial coagulum maturation of *Hevea* natural rubber. Journal of Applied Polymer Science, **118**, 1341–1348 (2010).
DOI: 10.1002/app.32331
[38] Gan S-N., Ting K-F.: Effect of treating latex with some metal ions on storage hardening of natural rubber. Polymer, **34**, 2142–2147 (1993).
DOI: 10.1016/0032-3861(93)90742-S
[39] Bristow G. M., Watson W. F.: Cohesive energy densities of polymers. Part 2. – Cohesive energy densities from viscosity measurements. Transactions of the Faraday Society, **54**, 1742–1747 (1958).
DOI: 10.1039/TF9585401742

eXPRESS Polymer Letters Vol.10, No.5 (2016) 420–429
Available online at www.expresspolymlett.com
DOI: 10.3144/expresspolymlett.2016.39

Enzymatic hydrophobization of jute fabrics and its effect on the mechanical and interfacial properties of jute/PP composites

A. Dong[1], *H. Wu*[1], *X. Fan*[1,2], *Q. Wang*[1,2*], *Y. Yu*[1], *A. Cavaco-Paulo*[2,3]

[1]Key Laboratory of Science and Technology of Eco-Textile, Ministry of Education, Jiangnan University, Wuxi, 214122 Jiangsu, China
[2]International Joint Research Laboratory for Textile and Fiber Bioprocesses, Jiangnan University, Wuxi, 214122 Jiangsu, China
[3]Centre of Biological Engineering, University of Minho, Campus de Gualtar, 4710-057 Braga, Portugal

Received 13 October 2015; accepted in revised form 14 December 2015

Abstract. In this work, a hydrophobic surface of lignocellulosic jute fabric was achieved via the laccase-mediated grafting of octadecylamine (OA) on lignin moieties of jute aiming to improve the interfacial compatibility with the hydrophobic polypropylene (PP) resins in the fiber-reinforced composites. Firstly, the surface and total elemental compositions of the modified jute fabrics were investigated by X-ray photoelectron spectroscopy (XPS) and elemental analysis, respectively. The increases in the surface C/O ratio and total nitrogen content of jute fabrics after the laccase/OA treatment indicated that OA molecules were successfully grafted onto the jute surface mediated by laccase. The grafting percentage of OA on jute fabrics was 0.96%. The surface hydrophobicity of jute fabrics with static contact angle of 112.5°, advancing angle of 116.4° and receding angle of 42.7° supported the presence of nonpolar alkyl chains on the jute surface after the laccase-mediated OA-grafting. The tensile strength, tensile modulus as well as the elongation at break of the hydrophobized jute/PP composites were increased. The fracture surface of the composites became neat and the jute fibers on the section surface were surrounded by PP resins closely, which suggested better interfacial adhesion between the jute reinforcement and the PP resin.

Keywords: *polymer composites, jute fiber reinforcement, laccase, hydrophobization, interfacial compatibility*

1. Introduction

The application of natural plant fibers such as ramie fiber, jute fiber, sisal fiber and bamboo fiber to replace glass fiber and synthetic fibers as the reinforcement of resin matrix composites has drawn a wide public attention in recent decades [1, 2]. These natural fibers can not only meet the property requirements for reinforced materials in composites but also have the merits of low cost, abundance, light weight, biodegradability and renewability. However, plant fibers mainly consisting of cellulose, hemicellulose and lignin always exhibit strong hydrophilicity and high moisture absorption. This deteriorates the interfacial compatibility with hydrophobic resins and then the mechanical properties of the fiber-reinforced composites [3, 4]. In order to obtain high-performance composite materials, surface modification of the fiber reinforcements including various physical and chemical processing technologies proved to be an effective and practical method.

However, these traditional approaches were demonstrated to have some inherent shortcomings. The physical methods may be difficult to industrialize and can seriously deteriorate the mechanical properties of the natural fibers, especially the tensile strength [5, 6]. The grafting modification with vinyl mono-

*Corresponding author, e-mail: qiang_wang@163.com
© BME-PT

mers can increase the hydrophobicity of the fibers and improve the compatibility with hydrophobic resin matrix [7]. But it is also known that the homopolymerization will occur inevitably. Although the treatment of fibers with organic silane coupling agents has achieved much success in improving the surface hydrophobicity, it usually involves complicated multi-step processes and waste disposal of emulsifiers present on the surface after the treatment [8, 9]. Moreover, the current increasing concern on the environmental protection also hinders the industrial application of silicon compounds. Therefore, it has great practical significance to explore new modification methods for the natural fibers.

Nowadays, the use of enzymes as important biotechnological catalysts in the surface processing of lignocellulosic polymers is increasing dramatically [10–14]. Enzymatic processes have advantages such as specificity, effectiveness, eco-friendly nature and working in mild conditions as compared to the conventional methods. Laccases (EC 1.10.3.2, benzenediol:oxygen oxidoreductase) are the most investigated enzymes in this field. They are multi-copper glycoproteins that catalyze the monoeletronic oxidation of phenols and aromatic amines to reactive radicals and simultaneously reduce molecular oxygen to water in a redox reaction [15, 16]. Studies show that lignin is a suitable substrate for laccase and the phenolic sites of lignin molecules can be oxidized to phenoxyl radicals by laccase [17]. With the laccase-catalyzed oxidation of lignin moieties rich on the surface, the lignocellulosic materials could be activated to create a radical-rich reactive surface to which oxidized (radical-containing) phenolic molecules of interest by laccase simultaneously can be grafted [18–23]. Natural jute fiber, a widely used lignocellulosic bioresource with lignin content of 14–20%, also has the potential to be modified by this green biotechnology for endowing it with better performance or novel functions [24, 25]. Besides the use of phenolic monomers in the enzymatic grafting reactions, aliphatic amines were first reported by Kudanga *et al*. [26] to couple with lignin model molecules mediated by laccase. However, as far as our knowledge goes, no attempt has seemingly been made before for the surface hydrophobization of jute fibers by the laccase-mediated grafting of amine monomers to increase the interfacial compatibility with hydrophobic resins in composites.

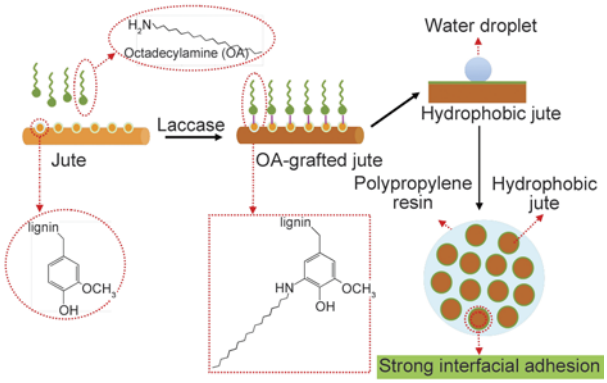

Figure 1. Schematic illustration of the enzymatic grafting of octadecylamine to lignins on the jute surface aiming to improve the interfacial adhesion with polypropylene resins

In the present work, lignocellulosic jute fabrics were modified to be hydrophobic via the laccase-mediated grafting of octadecylamine (OA) on the lignin moieties and then the hydrophobized jute was used as the reinforced material of the polypropylene (PP) matrix composites to improve the interfacial compatibility between the fiber reinforcements and the hydrophobic resins as shown in Figure 1. Initially, the surface elemental composition of jute fabrics was characterized by XPS and the grafting percentage of OA on jute fabrics was determined by elemental analysis. Then, the surface hydrophobicity of jute fabrics was investigated in terms of static and dynamic contact angles. Further, the pyrolytic characteristics of jute fabrics were studied by means of thermogravimetry (TGA) and differential thermogravimetry (DTG) measurements. Lastly, the tensile properties, dynamic mechanical performances and fracture surface of jute fabric/ PP composites were analyzed.

2. Experimental

2.1. Materials and reagents

Laccase from *Trametes Versicolor* was provided by Sigma-Aldrich. The 100% raw jute fabrics (427 g/m^2), with a 7/7 (warp/weft) cm^{-1} fabric density, were supplied by Longtai Weaving Co. Ltd. (Changshu, China). Octadecylamine (OA) with 90% purity was obtained from Aladdin Technology Co. Ltd. (Shanghai, China). Polypropylene (PP) melt-blown nonwoven cloths (200 g/m^2) were purchased from Yonghui Textile Technology Co. Ltd. (Yangzhou, China). All the other chemicals used in this study were commercially available and analytical grade.

2.2. Laccase assay

The activity of laccase was measured using a UV-Vis spectrophotometer by monitoring the oxidation of 2, 2′-azino-bis-(3-ethylthiazoline-6-sulfonate) (ABTS; ε_{420} = 36 000 $M^{-1}\cdot cm^{-1}$) as the substrate at 420 nm in 80/20 (v/v, %) 0.2 M acetate buffer (pH 4)/EtOH mixtures at 50 °C. The enzyme activity was expressed in units defined as micromoles of ABTS oxidized per minute [27].

2.3. Pretreatment of jute fabrics

Jute fabrics (500 mm long and 100 mm wide) were Soxhlet-extracted with benzene/ethanol (v/v, 2:1) for 12 h to remove the lipophilic extractives and then boiled with distilled water for 3 h to remove the water-soluble fractions. As a result, the oxidation of substrate molecules by laccase and the analysis of modified fabrics could be carried out without interference.

2.4. Enzymatic grafting of jute fabrics with OA monomers

Jute fabrics of 1 g were incubated in 50 mL 80/20 (v/v, %) 0.2 M acetate buffer (pH 4)/EtOH solutions with 1.5 U/mL laccase and 20 mM OA. The reaction was carried out at 50 °C for 24 h in a shaking bath. Afterwards, the fabrics were washed twice with distilled water at 50 °C for 20 min and then extracted with benzene/ethanol (v/v, 2:1) for 12 h to remove the absorbed (non-covalent bonding) OA monomers. Control and laccase-treated samples followed the same treatment condition as mentioned above.

2.5. XPS measurement of jute fabrics

X-ray photoelectron spectroscopy (XPS) experiments were performed on a RBD upgraded PHI-5000C ESCA system (Perkin Elmer) with Mg Kα radiation ($h\nu$ = 1253.6 eV). The X-ray anode was run at 250 W, and the high voltage was maintained at 14.0 kV with a detection angle of 54°. The whole spectra (0–1100 eV) and the narrow spectra of all the elements with much high resolution were both recorded using RBD 147 interface (RBD Enterprises, USA) through AugerScan 3.21 software. Binding energies were calibrated with the contaminant carbon (C_{1s} = 284.6 eV).

2.6. Elemental analysis of jute fabrics

The total carbon, hydrogen and nitrogen contents of the jute fabric samples were determined in an elemental analyzer (Elementar Vario EL III, Germany).

2.7. Determination of grafting percentage on jute fabrics

The grafting percentage (Gp) of the enzymatic OA-grafting onto jute fabrics was calculated from the total nitrogen content of samples using Equation (1):

$$Gp\,[\%] = \frac{N_g - N_c}{14}\cdot M_{C_{18}H_{39}N} \quad (1)$$

where N_g is the nitrogen content of the grafted jute fabrics [%], N_c is the nitrogen content of the control jute fabrics [%], and M is the molar mass of OA molecules [$g\cdot mol^{-1}$].

2.8. Contact angle measurements of jute fabrics

Before the contact angle measurements, jute fabric samples were conditioned to equilibrium moisture content (ca. 6.4%) in a constant temperature and humidity equipment (21 °C, 65%RH). The static contact angle of jute fabrics was determined in 3 s after water drop deposition using a JC2000D4 contact angle meter (Zhongchen, Shanghai). For each sample, five spots were measured, and then the results were averaged.

The dynamic contact angle of jute fabrics was measured by the Wilhelmy technique on a DCAT-21 interfacial tension meter (Dataphysics, Germany). Samples with a thickness of 1.2 mm and a width of 15 mm were immersed into and withdrawn out of water while simultaneously measuring the force acting on the sample at 20 °C. The advancing and receding contact angles could then be calculated from the recorded force curve. Three samples were taken for each treatment and the results were averaged.

2.9. Thermal analysis of jute fabrics

The thermogravimetric analysis (TGA) of the jute fabric samples was conducted on a Q500 thermogravimetric analyzer (TA Instruments, USA) in the range of 30–700 °C with a heating rate of 20 °C/min.

2.10. Preparation of jute fabric/PP composites

First, jute fabrics (1.2 mm thick after the enzymatic treatments) and PP foils (0.6 mm thick) were cut into samples of 20 mm width and 100 mm length. Then, the jute fabric/PP complex was prepared by the successive laying with two layers of jute fabrics and three layers of PP foils in a mass ratio of 1:1.

Finally, the composite samples were compressed in the steel mould (1 mm thick) at 180 °C in 10 ton pressure for 10 min.

2.11. Tensile measurement of jute fabric/PP composites

The tensile properties of the jute fabric/PP composites were determined using a KD111-5 microcomputer-controlled electronic universal testing machine. The composite samples had a dimension of 100 mm (length)×20 mm (width). The average thickness of the composites was 1 mm with a random error of <0.1 mm. The gauge length was set at 60 mm, and the testing speed was 2 mm/min. A stress-strain curve of the composites and the data of the breaking strength, modulus and elongation were recorded. All measurements were performed using at least five samples.

2.12. Fracture analysis of jute fabric/PP composites

The fracture sections of the jute fabric-reinforced PP composites were scanned using a SU1510 scanning electron microscope (SEM, Hitachi, Japan) under 5.00 k voltages at 2.00 k magnification.

2.13. Dynamic mechanical analysis (DMA) of the jute fabric/PP composites

A Q800 DMA analyzer (TA Instruments, USA) was used for the evaluation of storage modulus and loss modulus. A three-point bending mode was employed. The samples were tested in a fixed frequency of 1.0 Hz and a heating rate of 5 °C/min. The samples were evaluated in the range from 30 to 160 °C. Each sample had a thickness of 1±0.1 mm, a width of 13 mm and a length of 60 mm.

3. Results and discussion

3.1. XPS analysis of jute fabric surface

XPS analysis of material surfaces could provide the surface information of the elemental composition as well as the bonding states of atoms. In this study, XPS spectroscopy was used to understand efficiently the changes in the surface chemistry of jute fabrics resulted from the laccase/OA treatment. Table 1 showed a general survey of the surface atomic composition for the treated jute fabric samples. The surface C/O ratio of the laccase/OA-treated jute (3.4) was increased compared with the laccase-treated jute (2.7) and the control jute (2.6). This could be attributed to the grafting of OA molecules onto the jute surface mediated by laccase, as the OA structure has a high carbon content of 93.9% without any oxygen atoms.

Table 1. Surface chemical composition of the treated jute fabric samples obtained by XPS analysis

Samples	Elements [%]			C/O
	C_{1s}	O_{1s}	Others	
Control jute	68.8	26.6	4.7	2.6
Laccase-treated jute	68.5	25.5	6.0	2.7
Laccase/OA-treated jute	73.3	21.7	5.0	3.4

3.2. Estimation of grafting percentage via elemental analysis

The total nitrogen content of jute fabrics was measured by the elemental analyzer, from which the grafting percentage (*Gp*) of OA on jute fabrics could be calculated by using Equation (1). The total nitrogen, carbon, hydrogen, oxygen contents as well as the C/O ratio of jute fabric samples after the laccase/OA and control treatments were listed in Table 2. The total nitrogen content of the laccase/OA treated jute (0.18%) was increased when contrasted with the control jute (0.13%). The obtained *Gp* of the laccase-mediated OA-grafting reaction was 0.96%. In addition, there also has an enhancement in the total C/O ratio of the laccase/OA-treated jute fabrics, which indicated that the long alkyl chains of OA molecules were successfully incorporated to the jute surface via the laccase-mediated grafting in the laccase/OA treatment.

This eco-friendly enzymatic process provides an attractive alternative to the current methods for improving the surface hydrophobicity of jute fiber and other natural lignocellulosic fibers. Enzyme technologies are specific, effective, green and work in mild conditions in response to the shortcomings of traditional physical and chemical approaches. The monomers of the laccase-mediated grafting can be divided into two categories, phenolic compounds and amine compounds. It is generally reported that the laccase-mediated grafting of phenolic monomers

Table 2. Total elemental composition of jute fabrics after the laccase/OA and control treatments

Treatments	Element content [%]				C/O
	C	H	O	N	
Laccase/OA	45.07	6.96	47.78	0.18	0.94
Control	44.48	6.88	48.51	0.13	0.92

onto lignocellulosic materials has been successfully achieved to endow such polymers with novel functions [18–25]. However, the homopolymerization of these phenols will occur inevitably accompanied with the desired enzymatic grafting reaction. By contrast, the amine compounds such as OA used in this study could not be polymerized or self-coupled by laccase and are considered as ideal monomers for the enzymatic grafting modification of natural lignocellulosic polymers.

3.3. Effect of OA-grafting on surface hydrophobicity of jute fabrics

Wettability of fibers is an important factor for the interfacial adhesion with the hydrophobic resin matrix in composites as well as the water absorption behavior of the composites [28]. The hydrophilic characteristics of jute fibers lead to poor wettability and weak interfacial bonding with resins and facilitate the intake of water when the composites were immersed in water, finally resulting in decreased mechanical and physical properties of the composites [29]. In order to evaluate the surface hydrophobization of jute fabrics via the laccase-mediated grafting of OA, both static and dynamic contact angles were measured. The contact angle data were summarized in Table 3 and the force curves acting on jute fabric samples in the Wilhelmy measurement were presented in Figure 2.

Table 3. Static/dynamic contact angles of jute fabrics after different treatments

Treatments	Static contact angle [°]	Advancing angle [°]	Receding angle [°]
Laccase/OA	112.5±8.1	116.4±2.0	42.7±2.8
Laccase alone	0.0	75.1±1.8	0.0
Control	0.0	43.5±0.6	0.0

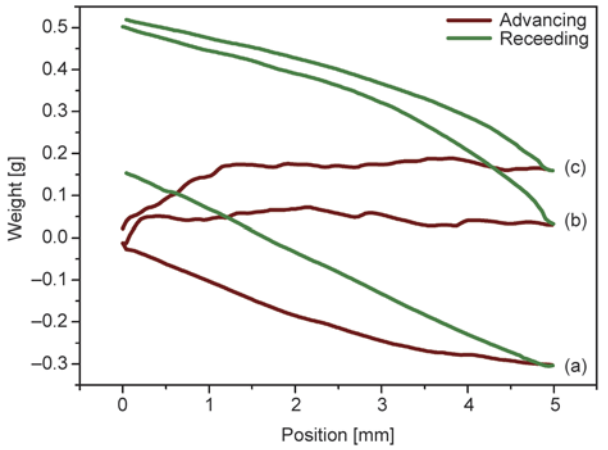

Figure 2. Force curves acting on laccase/OA treated jute fabrics (a), laccase-treated jute fabrics (b) and control jute fabrics (c) when immersed into and withdrawn out of water

For the control and laccase-treated jute fabrics, the water droplets on their surfaces disappeared with no specular reflectance in 3 s. In contrast, the laccase/OA-treated samples showed an increased static contact angle of 112.5°. However, the static contact angle is not able to explain exactly the dynamic behavior of the surface wettability because of the hysteresis of the contact angle. The dynamic contact angle measurement, based on the Wilhelmy principle, is specially designed to reveal the dynamic process of wetting. When a solid object is immersed into a liquid, the liquid will ascend (hydrophilic) or descend (hydrophobic) along the vertical direction of the solid. The Wilhelmy method measures the pull force or the push force acting on the solid to calculate the dynamic contact angles. According to Huang's description, the relationship between the force acting on samples (F) and the contact angle of samples (θ) is as followed [30] (Equation (2)):

$$F = 2w \cdot t \cdot \sigma \cdot \cos\theta \quad (2)$$

where w is the width of the sample and t is the thickness of the sample.

For the control and the laccase-treated jute samples, the advancing angles were 43.5 and 75.1°, respectively. Both of them had no receding angles. By contrast, the laccase/OA-treated samples showed a larger advancing contact angle of 116.4° and a receding angle of 42.7°. The surface hydrophobic enhancement of jute fabrics after the laccase/OA treatment supported that OA monomers containing nonpolar alkyl chains have been grafted onto the jute fabric surface mediated by laccase.

3.4. Effect of OA-grafting on thermal properties of jute fabrics

TGA and DTG curves of the treated jute fabrics and the OA monomer were shown in Figure 3. The OA monomer got its maximum mass loss rate at 245 °C, and there was no solid residue left at 690 °C. The control jute attained the maximum mass loss rate at 388 °C with 14.1% residue left at 690 °C. The laccase-treated sample displayed a similar trend as the control sample with the maximum mass loss rate at 389 °C and 13.1% residue at 690 °C. For the laccase/OA treated jute, its thermal resistance was decreased

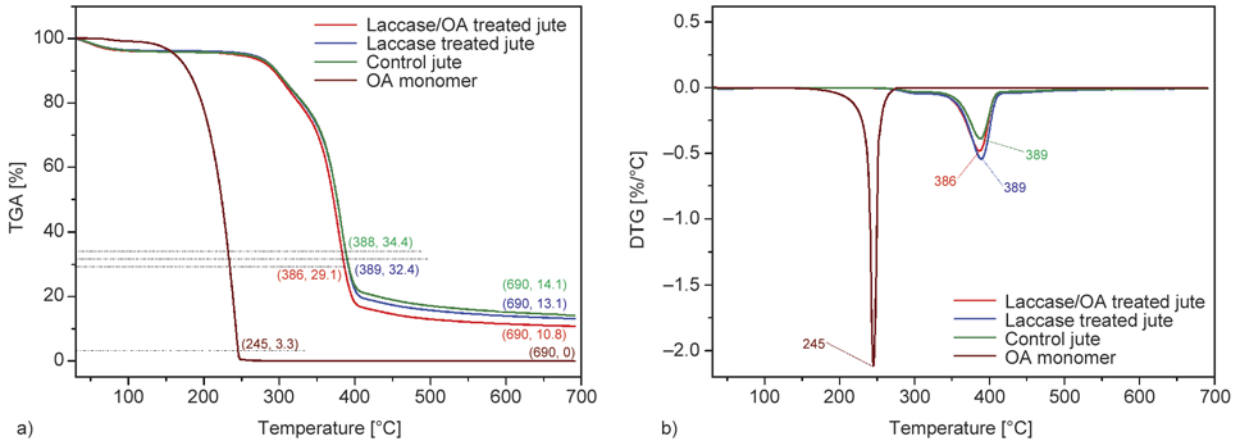

Figure 3. TGA (a) and DTG (b) curves of the treated jute fabrics and the OA monomer

with the maximum mass loss rate at 386 °C and the solid residue of 10.8% at 690 °C. This could result from the laccase-mediated grafting of OA molecules with lower thermo-stability onto jute fabrics. However, it should be noted that the enzymatic modification of jute could only occurs on the surface and thus it has slight effects on the thermal properties of the entire jute fabrics.

In addition, the jute was used later to prepare fiber-reinforced PP matrix composites at 180 °C by using hot pressing. According to the thermal data of OA molecules and jute fabrics, their temperatures at the maximum mass loss are both much higher than the temperature of the hot press process. Therefore, the hydrocarbon chains grafted on the jute surface and the jute fabrics wouldn't be damaged or change their chemical structures in the preparation of the jute/PP composites.

3.5. Interfacial behavior of jute fabric/PP composites

The fracture surfaces of all the composites were produced by stretching on a universal testing machine and then observed by SEM. The micrographs of the fracture sections were exhibited in Figure 4. The diameter of natural jute fibers is generally 15–25 μm with an oval cavity inside. The areas marked by red circles and rectangles in the SEM images are the ends or tips of jute fibers breaking by the stretching of the jute/PP composites. In the case of the control composites (Figure 4a) and the laccase-treated jute/PP composites (Figure 4b), the tips of fibers were protruded from the polymer matrix and thus the fracture surfaces became uneven and irregular. In addition, there are multitudes of pores normally seen on the tips, which resulted from the breaking and denting of the PP-filled fiber cavities by pulling. For the OA-grafted jute/PP composites (Figure 4c), PP matrix surrounding jute fibers and in the cavities of the fibers was pulled out together with the jute fibers. Jute fibers well adhered to the PP resins to form a neat and smooth fracture surface, indicating the stronger interfacial adhesion of the composites and adequate wetting of fibers with PP resins. While in the other two images, the fibers were pulled out of the polymer matrix during fracturing of the sample, indicating a much weaker interaction between the polymers and the fibers. Therefore, it could be concluded that the modified jute fibers were better coated by PP and stronger fiber-matrix adhesion was obtained owing to the enzymatic hydrophobic modification of the jute surface.

3.6. Tensile properties of jute fabric/PP composites

The breaking strength, Young's modulus and elongation at break of the treated jute/PP composites were given in Table 4. Besides, the tensile stress-strain curves of these composites were shown in Figure 5.

The control jute/PP composites showed the lowest breaking strength (25.6 MPa) and Young's modulus (5.4 GPa) among the three types of composites. After the laccase treatment of jute, the breaking strength and the Young's modulus of the composites were increased by 32.8 and 3.7%, respectively. Moreover, the OA-grafted jute/PP composites displayed larger increases in breaking strength and Young's modulus by 82.0 and 22.2%, respectively. These enhancements in tensile strength and modulus of OA-grafted jute/PP composites suggested that the interfacial compatibility of the composites

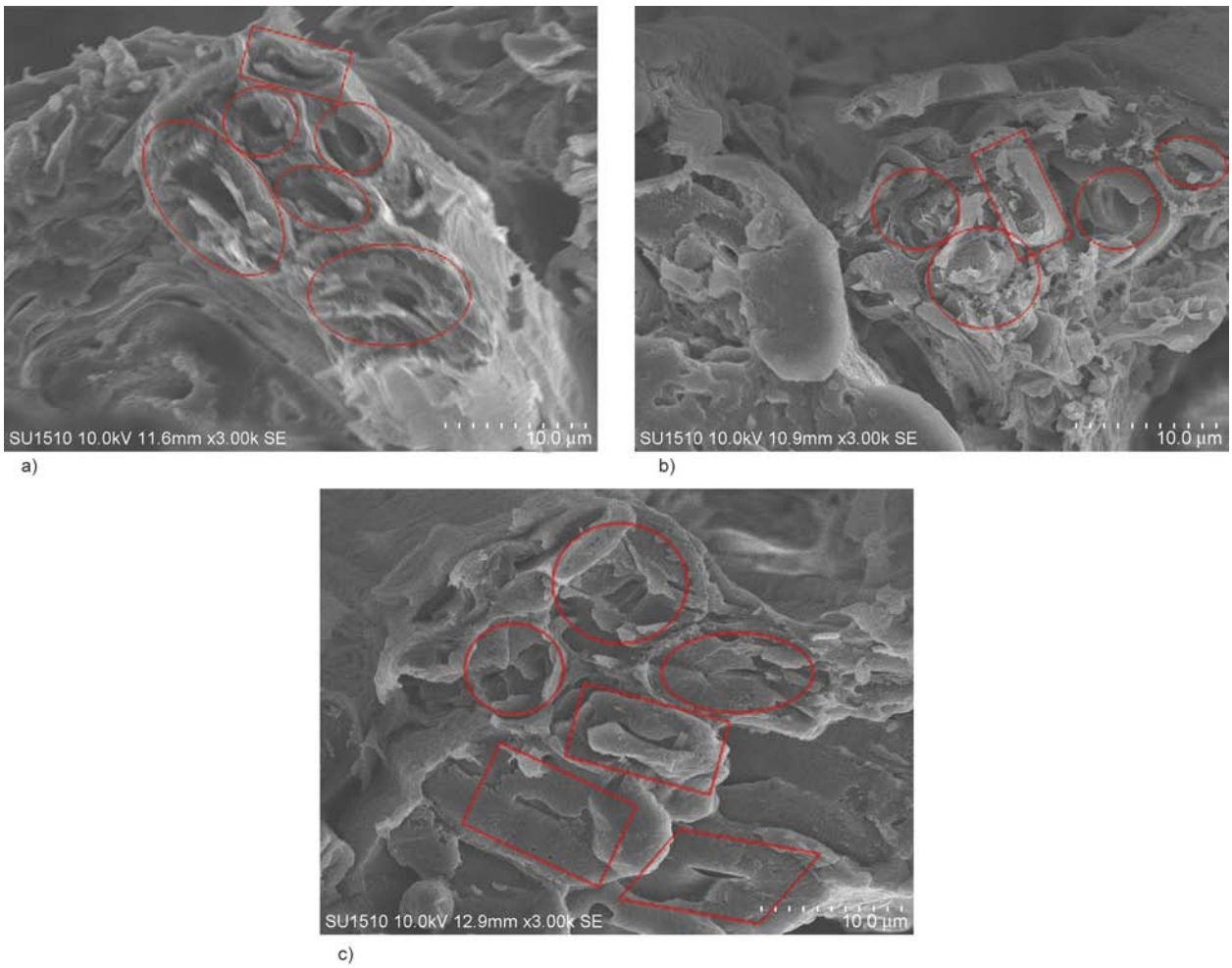

Figure 4. SEM images of fracture sections of control jute fabric/PP composites (a), laccase-treated jute fabric/PP composites (b) and OA-grafted jute fabric/PP composites (c)

Table 4. Mechanical properties of the treated jute/PP composites

Composites	Breaking strength [MPa]	Young's modulus [GPa]	Elongation at break [%]
Control jute/PP	25.6±0.7	5.4±0.4	1.5±0.1
Laccase-treated jute/PP	34.0±1.3	5.6±0.1	2.4±0.1
OA-grafted jute/PP	46.6±0.9	6.6±0.2	3.1±0.1

was enhanced after the surface hydrophobization of jute fabrics. The long alkyl chains of OA molecules grafted on the jute surface could interact with the PP resins via numerous van der Waals' forces. Therefore, better interfacial adhesion between fibers and hydrophobic resins were obtained, which made the stress to transfer effectively and thus satisfied the requirement of reinforcing the composites with better mechanical properties. In addition, the elongation at break of the enzymatic treated jute/PP composites was also increased. This may be owing to the increase in the elongation at break of jute fabrics after the laccase treatment (no data shown).

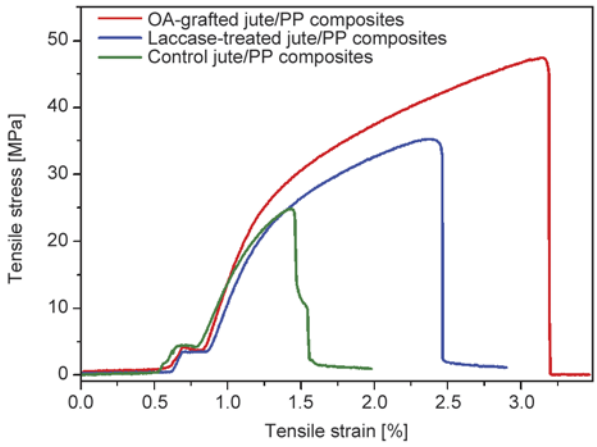

Figure 5. Tensile stress-strain curves of the treated jute fabric/PP composites

3.7. Dynamic mechanical properties of jute fabric/PP composites

Dynamic thermo-mechanical properties of the jute fabric/PP composites, storage modulus (E') and loss modulus (E'') curves as a function of temperature were measured and illustrated in Figure 6. E' is very

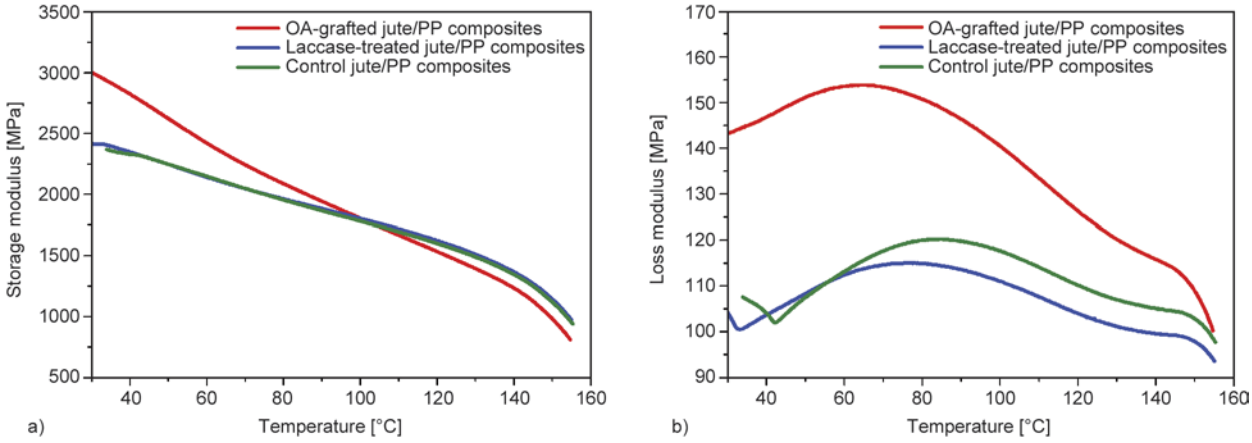

Figure 6. Dynamic mechanical properties of the treated jute fabric/PP composites: Storage (a) and loss modulus (b)

sensitive to the structural and molecular changes of composites, such as fiber-matrix interfacial bonding [31]. The E' values of all the composites dropped with the increase of temperature. However, the PP composites reinforced by the OA-grafted jute fabrics had a significant increase in the E' before 100 °C in contrast with the laccase-treated jute/PP composites and the control composites. This can be explained as the result of improved interfacial adhesion between the hydrophobic jute and the PP matrix, which allowed greater stress to transfer at the interface.

As shown in Figure 6b, the OA-grafted jute/PP composites had higher E'' values in the whole range of testing temperatures than those of the control composites and the laccase-treated jute/PP composites. E'' is attributed to the mobility of resin molecules in composites [9]. Larger E'' values suggest stronger restraining effect of fibers on the mobility of the resin matrix. The corresponding increase in E'' value indicated the restriction was enhanced with the enzymatic hydrophobization of fibers and the fact of immobilization of PP molecules near to the hydrophobic surface of the modified jute fibers. The improved interfacial adhesion reduced the mobility of the PP molecular chain at the interface.

4. Conclusions

The present work demonstrated that the covalent attachment of OA onto jute surface mediated by laccase resulted in increases in the surface hydrophobicity of jute fabrics and the interfacial compatibility between jute fibers and PP resins. The surface C/O ratio and the total nitrogen content of jute fabrics were increased after the enzymatic grafting, which suggested that OA molecules have been successfully incorporated onto the jute fabric surface mediated by laccase. The *Gp* of the enzymatic OA-grafting reaction was 0.96%. The modified jute obtained excellent water repellency with static contact angle of 112.5°, advancing angle of 116.4° and receding angle of 42.7°, which supported the presence of nonpolar alkyl chains on the jute surface after the laccase-mediated grafting of OA. No evident decrease of thermal properties was found due to the specificity of laccase to substrates and the surface modification of the enzymatic grafting. The tensile strength, tensile modulus as well as the breaking elongation of the hydrophobized jute/PP composites were increased. The fracture surface of the composites became neat and the jute fibers on the section surface were surrounded by PP resins closely, which suggested better interfacial adhesion between the jute reinforcement and the PP resin.

Acknowledgements

This work was financially supported by National Natural Science Foundation of China (51173071), Program for New Century Excellent Talents in University (NCET-12-0883), Program for Changjiang Scholars and Innovative Research Team in University (RT_15R26), Fundamental Research Funds for the Central Universities (JUSRP51312B, JUSRP51505).

References

[1] Wambua P., Ivens J., Verpoest I.: Natural fibres: Can they replace glass in fibre reinforced plastics? Composites Science and Technology, **63**, 1259–1264 (2003). DOI: 10.1016/S0266-3538(03)00096-4

[2] Bledzki A. K., Mamun A. A., Faruk O.: Abaca fibre reinforced PP composites and comparison with jute and flax fibre PP composites. Express Polymer Letters, **1**, 755–762 (2007). DOI: 10.3144/expresspolymlett.2007.104

[3] Hughes M.: Defects in natural fibres: Their origin, characteristics and implications for natural fibre-reinforced composites. Journal of Materials Science, **47**, 599–609 (2012).
DOI: 10.1007/s10853-011-6025-3

[4] Bledzki A. K., Mamun A. A., Lucka-Gabor M., Gutowski V. S.: The effects of acetylation on properties of flax fibre and its polypropylene composites. Express Polymer Letters, **2**, 413–422 (2008).
DOI: 10.3144/expresspolymlett.2008.50

[5] Albanoa C., Reyes J., Ichazo M., González J., Brito M., Moronta D.: Analysis of the mechanical, thermal and morphological behaviour of polypropylene compounds with sisal fibre and wood flour, irradiated with gamma rays. Polymer Degradation and Stability, 76, 191–203 (2002).
DOI: 10.1016/S0141-3910(02)00014-9

[6] Yuan X., Jayaraman K., Bhattacharyya D.: Effects of plasma treatment in enhancing the performance of woodfibre-polypropylene composites. Composites Part A: Applied Science and Manufacturing, **35**, 1363–1374 (2004).
DOI: 10.1016/j.compositesa.2004.06.023

[7] Kalia S., Kaith B. S., Kaur I.: Pretreatments of natural fibers and their application as reinforcing material in polymer composites – A review. Polymer Engineering and Science, **49**, 1253–1272 (2009).
DOI: 10.1002/pen.21328

[8] Gassan J., Bledzki A. K.: The influence of fiber-surface treatment on the mechanical properties of jute-polypropylene composites. Composites Part A: Applied Science and Manufacturing, **28**, 1001–1005 (1997).
DOI: 10.1016/S1359-835X(97)00042-0

[9] Hong C. K., Hwang I., Kim N., Park D. H., Hwang B. S., Nah C.: Mechanical properties of silanized jute–polypropylene composites. Journal of Industrial and Engineering Chemistry, **14**, 71–76 (2008).
DOI: 10.1016/j.jiec.2007.07.002

[10] Hüttermann A., Mai C., Kharazipour A.: Modification of lignin for the production of new compounded materials. Applied Microbiology and Biotechnology, **55**, 387–394 (2001).
DOI: 10.1007/s002530000590

[11] Nyanhongo G. S., Kudanga T., Prasetyo E. N., Gübitz G. M.: Enzymatic polymer functionalisation: Advances in laccase and peroxidase derived lignocellulose functional polymers. Advances in Biochemical Engineering/Biotechnology, **125**, 47–68 (2011).
DOI: 10.1007/10_2010_86

[12] Kudanga T., Prasetyo E. N., Sipilä J., Nyanhongo G. S., Guebitz G. M.: Chemo-enzymatic functionalisation of lignocellulose materials using oxiranes. Process Biochemistry, **45**, 1557–1562 (2010).
DOI: 10.1016/j.procbio.2010.06.008

[13] Aracri E., Colom J. F., Vidal T.: Application of laccase-natural mediator systems to sisal pulp: An effective approach to biobleaching or functionalizing pulp fibres? Bioresource Technology, **100**, 5911–5916 (2009).
DOI: 10.1016/j.biortech.2009.06.016

[14] Zhou H., Yang D., Qiu X., Wu X., Li Y.: A novel and efficient polymerization of lignosulfonates by horseradish peroxidase/H_2O_2 incubation. Applied Microbiology and Biotechnology, **97**, 10309–10320 (2013).
DOI: 10.1007/s00253-013-5267-1

[15] Claus H.: Laccases: structure, reactions, distribution. Micron, **35**, 93–96 (2004).
DOI: 10.1016/j.micron.2003.10.029

[16] Riva S.: Laccases: Blue enzymes for green chemistry. Trends in Biotechnology, **24**, 219–226 (2006).
DOI: 10.1016/j.tibtech.2006.03.006

[17] Lahtinen M., Kruus K., Heinonen P., Sipilä J.: On the reactions of two fungal laccases differing in their redox potential with lignin model compounds: Products and their rate of formation. Journal of Agricultural and Food Chemistry, **57**, 8357–8365 (2009).
DOI: 10.1021/jf901511k

[18] Kudanga T., Prasetyo E. N., Widsten P., Kandelbauer A., Jury S., Heathcote C., Sipilä J., Weber H., Nyanhongo G. S., Guebitz G. M.: Laccase catalyzed covalent coupling of fluorophenols increases lignocellulose surface hydrophobicity. Bioresource Technology, **101**, 2793–2799 (2010).
DOI: 10.1016/j.biortech.2009.12.002

[19] Widsten P., Heathcote C., Kandelbauer A., Guebitz G., Nyanhongo G. S., Prasetyo E. N., Kudanga T.: Enzymatic surface functionalisation of lignocellulosic materials with tannins for enhancing antibacterial properties. Process Biochemistry, **45**, 1072–1081 (2010).
DOI: 10.1016/j.procbio.2010.03.022

[20] Garcia-Ubasart J., Vidal T., Torres A. L., Rojas O. J.: Laccase-mediated coupling of nonpolar chains for the hydrophobization of lignocellulose. Biomacromolecules, **14**, 1637–1644 (2013).
DOI: 10.1021/bm400291s

[21] Fillat A., Gallardo O., Vidal T., Pastor F. I. J., Díaz P., Roncero M. B.: Enzymatic grafting of natural phenols to flax fibres: Development of antimicrobial properties. Carbohydrate Polymers, **87**, 146–152 (2012).
DOI: 10.1016/j.carbpol.2011.07.030

[22] Liu N., Shi S. L., Gao Y., Qin M.: Fiber modification of kraft pulp with laccase in presence of methyl syringate. Enzyme and Microbial Technology, **44**, 89–95 (2009).
DOI: 10.1016/j.enzmictec.2008.10.014

[23] Dong A., Yu Y., Yuan J., Wang Q., Fan X.: Hydrophobic modification of jute fiber used for composite reinforcement *via* laccase-mediated grafting. Applied Surface Science, **301**, 418–427 (2014).
DOI: 10.1016/j.apsusc.2014.02.092

[24] Dong A., Yu Y., Fan X., Wang Q., Cavaco-Paulo A.: Enzymatic coating of jute fabrics for enhancing anti-ultraviolent properties via in-situ polymerization of polyhydric phenols. Journal of Industrial Textiles, in press (2016).
DOI: 10.1177/1528083715577935

[25] Thakur K., Kalia S., Kaith B. S., Pathania D., Kumar A.: Surface functionalization of coconut fibers by enzymatic biografting of syringaldehyde for the development of biocomposites. RSC Advances, **5**, 76844–76851 (2015).
DOI: 10.1039/c5ra14891j

[26] Kudanga T., Prasetyo E. N., Sipilä J., Guebitz G. M., Nyanhongo G. S.: Reactivity of long chain alkylamines to lignin moieties: Implications on hydrophobicity of lignocellulose materials. Journal of Biotechnology, **149**, 81–87 (2010).
DOI: 10.1016/j.jbiotec.2010.06.020

[27] Childs R., Bardsley W.: The steady-state kinetics of peroxidase with 2,2′-azino-di-(3-ethylbenzthiazoline-6-sulphonic acid) as chromogen. Biochemical Journal, **145**, 93–103 (1975).
DOI: 10.1042/bj1450093

[28] Ramamoorthy S. K., Bakare F., Herrmann R., Skrifvars M.: Performance of biocomposites from surface modified regenerated cellulose fibers and lactic acid thermoset bioresin. Cellulose, **22**, 2507–2528 (2015).
DOI: 10.1007/s10570-015-0643-x

[29] Ramamoorthy S. K., Di Q., Adekunle K., Skrifvars M.: Effect of water absorption on mechanical properties of soybean oil thermosets reinforced with natural fibers. Journal of Reinforced Plastics and Composites, **31**, 1191–1200 (2012).
DOI: 10.1177/0731684412455257

[30] Huang F., Wei Q., Wang X., Xu W.: Dynamic contact angles and morphology of PP fibres treated with plasma. Polymer Testing, **25**, 22–27 (2006).
DOI: 10.1016/j.polymertesting.2005.09.017

[31] Jacob M., Francis B., Thomas S.: Dynamical mechanical analysis of sisal/oil palm hybrid fiber-reinforced natural rubber composites. Polymer Composites, **27**, 671–680 (2006).
DOI: 10.1002/pc.20250

eXPRESS Polymer Letters Vol.10, No.5 (2016) 430–437
Available online at www.expresspolymlett.com
DOI: 10.3144/expresspolymlett.2016.40

Lipid-mediated protein functionalization of electrospun polycaprolactone fibers

C. Cohn[1], S. L. Leung[2], J. Crosby[1], B. Lafuente[3], Z. Zha[2], W. Teng[2], R. Downs[3], X. Wu[1,2]*

[1]Biomedical Engineering Graduate IDP, University of Arizona, AZ 85721 Tucson, USA
[2]Aerospace & Mechanical Engineering, University of Arizona, AZ 85721 Tucson, USA
[3]Department of Geosciences, University of Arizona, AZ 85721 Tucson, USA

Received 30 September 2015; accepted in revised form 16 December 2015

Abstract. In this study, electrospun polycaprolactone (PCL) fibers are plasma-treated and chemically conjugated with cholesteryl succinyl silane (CSS). In addition to Raman spectroscopy, an immobilization study of DiO as a fluorescent probe of lipid membranes provides evidence supporting the CSS coating of plasma-treated PCL fibers. Further, anti-CD20 antibodies are used as a model protein to evaluate the potential of lipid-mediated protein immobilization as a mechanism to functionalize the CSS-PCL fiber scaffolds. Upon anti-CD20 functionalization, the CSS-PCL fiber scaffolds capture Granta-22 cells 2.4 times more than the PCL control does, although the two fiber scaffolds immobilize a comparable amount of anti-CD20. Taken together, results from the present study demonstrate that the CSS coating and CSS-mediated antibody immobilization offers an appealing strategy to functionalize electrospun synthetic polymer fibers and confer cell-specific functions on the fiber scaffolds, which can be mechanically robust but often lack biological functions.

Keywords: *coatings, electrospun polycaprolactone fibers, cholesteryl succinyl silane, protein immobilization*

1. Introduction

Nanofiber scaffolds, which are fabricated by using self-assembling (SA) [1, 2] or fiber-spinning techniques [3–6], resemble the fibrillar and mechanical characteristics of extracelullar matrix (ECM) and are extensively explored for their potential applications in tissue and cell engineering. Various strategies have been pursued to introduce bioactive functionalities into nanofiber scaffolds to recapitulate the biological properties of ECM. For instance, amino acid sequences that are derived from ECM proteins have been incorporated into SA nanofiber hydrogels via protein engineering or click chemistry, promoting cell-specific activities such as cell adhesion and proliferation [7–9]. Subsequently, biofunctions of amino acid sequences may be well retained, because SA nanofiber hydrogels are often prepared under cell-compatible conditions. Compared to SA nanofiber hydrogels, synthetic polymer scaffolds fabricated using fiber-spinning techniques may possess enhanced mechanical properties that are necessary for many applications [10]. ECM derived proteins such as gelatin [10-12] and collagen [13-15] may be co-spun with synthetic polymers into nanofibers, and amino acid sequences or antibodies may be chemically conjugated onto synthetic polymer fibers [16–18], rendering the fiber scaffolds biologically active. However, the selection of protein- or peptide-based functionalities that can be incorporated onto synthetic polymer nanofibers may be limited by the harsh conditions of fiber spinning or by the particular conjugation chemistry that only works for certain biomolecules.

Here, we envision that the coating of electrospun polycaprolactone (PCL) fibers with cholesteryl succinyl silane (CSS) and the subsequent CSS-mediated anti-

*Corresponding author, e-mail: xwu@email.arizona.edu
© BME-PT

body immobilization on the fibers may provide an appealing strategy to biologically functionalize mechanically robust polymer scaffolds that otherwise support little cell-specific activities. Previously, we have engineered CSS fibers that are capable of immobilizing membrane-bound antibodies and retaining the antibody's cell-binding functions [19]. Recently, we have demonstrated that the CSS fibers possess a greater ability to functionally immobilize antibodies for cell capture than the PCL and plasma-treated PCL fibers do [20]. However, our previous work illustrates that the CSS fibers lack tensile strength [21], limiting their applications in tissue and cell engineering. In contrast, electrospun PCL fibers are well known for their good mechanical strength, slow enzyme-mediated degredation, and minimal toxicity [22–24]. As a continuation of our recent work, CSS molecules are hydrolyzed in ethanol solutions with the addition of a small amount of water, and the hydrolyzed CSS molecules form lipid vesicles; electrospun PCL fibers are plasma-treated and incubated with CSS vesicles in ethanol, leading to the immobilization, rupture and fusion of CSS vesicles into a continuously supported lipid bilayer on PCL fibers. Membrane-bound proteins such as antibodies can be immobilized on the PCL fibers coated with the CSS bilayers (CSS-PCL fibers) via a lipid-mediated immobilization mechanism, conferring cell-specific activities on the fiber scaffolds. As a result, the CSS-PCL fibers integrate the mechanical strength of PCL fibers and the ability of CSS bilayers to functionally immobilize membrane-bound proteins. This presents an appealing approach to functionalizing synthetic polymer fiber scaffolds for applications in tissue and cell engineering.

2. Experimental section

2.1. Fabrication of PCL fibers

PCL fibers were prepared with a 10% w/v solution of PCL (Polycaprolactone, M_W: 80 kDa, Sigma Aldrich, St. Louis, USA) in 1,1,1,3,3,3-Hexafluoro-2-propanol (HFP, M_W: 168.04, Sigma Aldrich, St. Louis, USA) [20]. The solution was incubated at room temperature for a minimum of 6 h, briefly vortexed, and electrospun at a flow rate of 20 μL/min, a voltage of 12 kV, and a spinneret-to-ground distance of 12 cm. The electrospun PCL fibers were collected on 0.25 cm^2 silicon chips that were placed on top of the aluminum foil collector plate. A portion of the silicon chips that collected electrospun PCL fibers immediately underwent an air-plasma treatment (Harrick Plasma, Model PDC-001, Ithaca, USA) for 10 min under vacuum, generating plasma-treated PCL fibers for further use [20].

2.2. Formation of CSS-PCL fibers

CSS was dissolved in 100% EtOH at the desired concentrations (e.g., 1.0, and 5.0% w/v); 200 μL of DI water was added to the 4 mL CSS solution, permitting the occurrence of hydrolysis and polymerization [19, 21]; silicon chips that collected freshly plasma-treated PCL fibers were each placed in a single well of a 48-well plate; a 500 μL solution of CSS was added to each well, submerging the plasma-treated PCL fibers. The 48-well plate was sealed, and placed under humidified conditions, allowing CSS to hydrolyze, forming vesicles and conjugating onto PCL fibers. The resulting CSS-PCL fibers were rinsed three times with DI water prior to use.

The water contact angles were assessed for electrospun PCL, plasma-treated PCL, and CSS-PCL fibers to evaluate changes in the hydrophilicity of fiber scaffolds due to air plasma treatment and CSS coating. A 10 μL droplet of DI water was placed on each type of fiber scaffolds (n = 3) and measured with instrumentation FTA-200 (RS-170 camera, First Ten Angstroms, Portsmouth, USA). The water contact angle was determined with FTA-32 software (First Ten Angstroms, Portsmouth, USA), and presented as mean ± standard error for each fiber type.

2.3. Characterization of CSS-PCL fibers

DiO (3,3′-Dioctadecyloxacarbocyanine perchlorate, Sigma Aldrich, St. Louis, USA), which is frequently used as a fluorescent probe of lipid bilayers [25], was utilized as a model system to study the CSS-mediated immobilization of membrane-bound molecules on CSS-PCL fibers. A working solution of DiO was prepared in 100% EtOH at a final concentration of 30 μg/mL. Silicon chips that collected CSS-PCL or PCL fibers were each placed in a single well of a 48-well plate. A 300 μL working solution of DiO was added to each well, and the fiber samples were incubated for 1 h in the dark and at room temperature. For a control study, the fiber samples were first exposed to 1% bovine serum albumin (BSA) solutions for 1 h at room temperature to block the fibers from interacting with DiO, and then incubated with DiO solutions for 1 h. The fiber specimens were washed with 100% EtOH three times, and submerged

in fresh EtOH, before the relative fluorescence intensities of immobilized DiO were read using a microplate reader (Synergy 2 SL Luminescence Microplate Reader, BioTek, Winooski, USA) at an excitation wavelength of 485 nm and an emission wavelength of 508 nm.

Raman spectroscopy was also employed to characterize CSS-PCL fibers, in comparison to the PCL control. The Raman spectra for each sample were collected from 20 scans and 60 seconds per scan on a micro-Raman system (Thermo Almega, Thermo Fisher Scientific, Waltham, USA), using a solid-state laser with a wavelength of 532 nm, and a thermoelectrically cooled CCD detector. The laser is partially polarized with a resolution of 4 cm^{-1} and a spot size of 1 µm.

2.4. Anti-CD20 immobilization on CSS-PCL fibers

The immobilization of anti-CD20 antibodies on the CSS-PCL fibers was examined, in comparison to the PCL and plasma-treated PCL controls. Following a protocol previously reported [19, 26], silicon chips that collected electrospun fibers were each placed in a single well of a 48-well plate, rinsed with PBS three times, exposed to 200 µL of a 10 µg/mL anti-CD20 solution, and incubated for 90 min at 37 °C. After the incubation period the solution was collected and placed in fresh wells of a new and sterile 96-well plate. The fiber specimens and wells were rinsed three times with PBS. The amount of unbound anti-CD20 remaining in the solution and washes from the same specimen was detected with a microplate reader (Synergy 2 SL Luminescence Microplate Reader, BioTek, Winooski, USA) at an excitation wavelength of 460/40 nm and an emission wavelength of 590/10 nm.

2.5. Cell capture

After anti-CD20 immobilization, the fiber specimens were incubated in a 0.1% w/v solution of BSA in 1× PBS for 1 h at 37 °C to block unbound reaction sites, washed with 1× PBS three times, and seeded with Granta-22 B-cell lymphomas at a density of $2 \cdot 10^4$ cells per sample. The functionalized fiber specimens were incubated for 45 min to allow for cell capture. After cell capture the specimens were washed three times with 1× PBS and subjected to a 15-min incubation in 4% w/v paraformaldehyde. The captured cells were treated with Triton-X prior to being stained with ProLong® Gold Antifade with DAPI (Thermo Fisher Scientific, Waltham, USA) against the cell nuclei, and imaged the following day with a Nikon fluorescent microscope.

2.6. Statistical analysis

A Student's *t*-test was computed between each fiber type to determine statistical significance for DiO immobilization, antibody immobilization, and cell capture efficiencies. *P*-values less than 0.05 were considered statistically significant whereas anything greater than 0.05 was considered statistically insignificant.

3. Results and discussion

As shown in Figure 1, air-plasma treatment induces chemical modification of electrospun PCL fibers and creates hydroxyl groups on the fiber surfaces, transforming hydrophobic PCL fiber scaffolds with a water contact angle of 93.3±2.3° into hydrophilic fiber scaffolds with a water contact angle of 35.1±2.2°. At a concentration of 1~5% w/w that exceeds the critical micelle concentration of lipid [27], CSS in ethanol can be hydrolyzed in the presence of a small amount of water and the hydrolyzed CSS molecules form lipid vesicles [28]. In a polar solvent, CSS vesicles adopt bilayer structures, in which their hydroxyl groups are exposed to solvents [28]. When the plasma-treated PCL fibers are immersed in CSS solutions, CSS vesicles would be immobilized on the fibers. It has been reported that PCL fibers can be modified by air-plasma treatment and chemical conjugated with laminin [24]. Here, PCL fibers can be

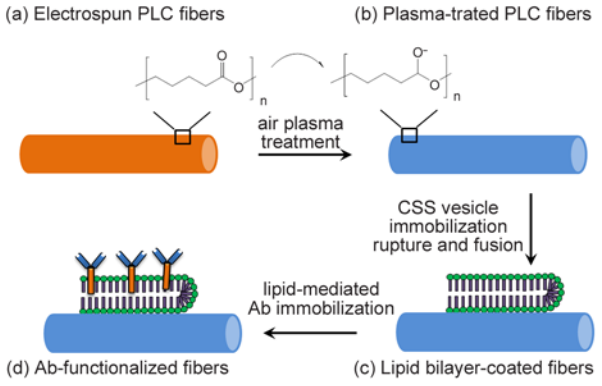

Figure 1. Schematic illustration of electrospinning of hydrophobic PCL fibers (a), air-plasma treatment of PCL fibers and generation of hydrophilic fibers (b), CSS vesicle immobilization, rupture and fusion on the plasma-treated PCL fibers (c), and antibody immobilization on and functionalization of the PCL fibers (d)

conjugated with CSS after air plasma treatment, improving the immobilization of CSS vesicles. Following a mechanism proposed by others [29, 30], the immobilized vesicles may rupture and fuse into a continuously supported lipid bilayer (Figure 1c). As suggested by others [29], the spreading of CSS bilayers on the fiber surfaces may provide a natural environment for the oriented immobilization of membrane-bound proteins such as antibodies under non-denaturing conditions (Figure 1d).

DiO was used as a lipid-membrane probe in the initial study to verify the CSS coating of the CSS-PCL fibers in comparison to the PCL control. The CSS-PCL fibers were obtained by incubating the plasma-treated PCL fibers in either a 1 or 5% w/v CSS solution overnight. The relative fluorescent intensity (RFI) of immobilized DiO was determined to be 45.8±5.76 on the CSS-PCL fibers and 13.5±3.6 on the PCL control (Figure 2). Compared to the PCL control, a 2.4-fold increase in RFI may be due to (1) an increase in the amount of DiO immobilized on the CSS-PCL fibers, (2) enhanced fluorescence of DiO in the presence of CSS membranes, or (3) both. As a lipid probe, DiO is fluorescent in the presence of lipid membranes. The lipid membranes of the CSS-PCL fibers may enhance DiO fluorescence in comparison to the PCL control. When the CSS-PCL fibers and the PCL control were exposed to BSA for 1 h, the fiber surfaces would be partially covered with BSA molecules and blocked from interacting with DiO. After the BSA treatment, the RFI of DiO was measured to be 17.86±1.12 on the CSS-PCL fibers and 9.2±2.4 on the PCL control. The BSA treatment leads to a 32% reduction in RFI on the PCL control and a 61% reduction on the CSS-PCL fibers. This suggests that the BSA treatment has more detrimental effects on the lipid-mediated immobilization of DiO on the CSS-PCL fibers than the hydrophobic immobilization of DiO on the PCL control.

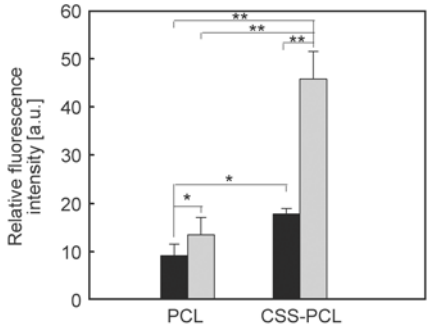

Figure 2. Relative fluorescence intensities (RFI) of DiO immobilized on the PCL control and CSS-PCL fibers, which were treated (gray) or not treated (black) with BSA. $^{*}p \leq 0.05$; $^{**}p \leq 0.01$.

Raman spectroscopy was further employed to characterize the CSS-PCL fibers. The use of a 100× objective generates a sampling spot of 1 μm in size, comparable to the diameters of PCL fibers [20]. This permits Raman spectroscopic analysis of single PCL or CSS-PCL fibers. In the spectral region of 600–1800 cm^{-1}, the PCL fibers display characteristic bands at 1725 (C=O stretching), 1462 and 1442 (CH_2 scissoring and wagging [31] and CH_3 asymmetric bending [32]), 1305 and 1285 (CH_2 bending), 1110 (C–O–C asymmetric stretching [33]), and 1066 (C–O–C symmetric stretching [33]), 958 (CH_3 rocking [34]), 916, 868, and 713 cm^{-1} (C=O bending [33]) (Figure 3). Compared to the PCL control, the CSS-PCL-1 fibers did not show noticeable changes in Raman spectra. However, the DiO immobilization study clearly indicates the CSS coating of CSS-PCL-1 fibers. Likely, Raman spectroscopy conducted at a single spot of about 1μm in size does not possess the same detection sensitivity of the DiO assay that is performed on fiber specimens of 0.25 cm^2 in size. When the CSS-PCL fibers were prepared by incubating plasma-treated PCL fibers with 5% w/v CSS solutions, new bands appeared at 1670 (C=O amide I), 877, 851, 801, 736, and 700 cm^{-1}, which can be attributed to CSS' cholesterol portion [35]. This suggests that the use of 5% w/v solutions improves the total mass of CSS coated on PCL fibers for Raman detection. In addition to the characteristic bands of the cholesterol segment of CSS, the hydrolyzed tri-

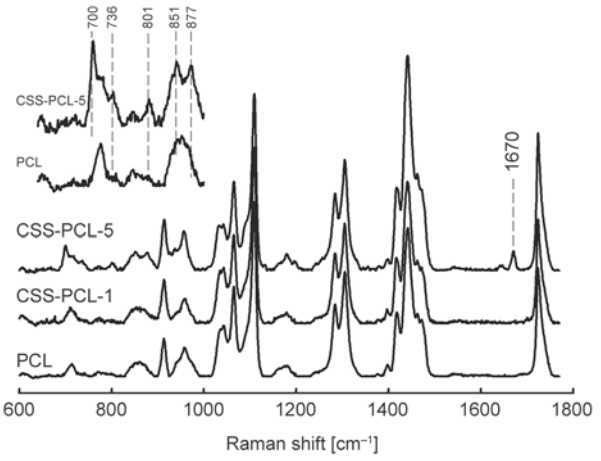

Figure 3. Raman spectra of CSS-PCL (i.e., CSS-PCL-1 and CSS-PCL-5) and PCL fibers. CSS-PCL-1 and CSS-PCL-5 fibers were obtained by incubating plasma-treated PCL fibers with 1 and 5% w/v CSS solutions, respectively

ethoxysilyl moieties may display peaks at 1092 (SiOC asymmetric stretching), 1046 (SiOSi asymmetric stretching), 948 (SiOC symmetric stretching), and 792 cm^{-1} (SiOSi symmetric stretching). However, those bands may be masked by the stronger bands of PCL at the similar locations.

Murine anti-CD20 was used to further investigate the ability of the CSS-PCL-1 fibers to immobilize membrane-bound proteins and retain protein functions. The amount of unbound anti-CD20 remaining in the solution was quantified (Figure 4a) and the amount of anti-CD20 immobilized on the fiber specimens was calculated (Figure 4b). When exposed to 2 μg anti-CD20 per sample, the amount of anti-CD20 remaining in the solution was evaluated to be 0.38±0.4, 0.96±0.40, and 0.31±0.21 μg for the PCL, plasma-treated PCL, and CSS-PCL-1 fiber scaffolds, respectively. The percentage of immobilized anti-CD20 was computed to be 81±12, 55±18, and 85±10% on the PCL, plasma-treated PCL, and CSS-PCL-1 fiber scaffolds, respectively. The CSS-PCL-1 fibers immobilized more anti-CD20 than the plasma-treated PCL control but a comparable amount of anti-CD20 as the PCL control. However, difference in the amounts of anti-CD20 immobilized on the three fiber types is statistically insignificant.

As previously reported, the function retention of anti-CD20 immobilized on electrospun fibers can be evaluated by using a cell-capture assay [20]. Because anti-CD20 specifically recognizes CD20 phosphoprotein expressed on the surfaces of normal B lymphocytes and B-cell lymphomas [36, 37], Granta-22 B cells were used in the cell capture study. Due to their non-adherent nature, Granta-22 cells immobilized on fiber specimens via non-specific binding can be readily removed by PBS washing. Consequently, the capture of Granta-22 cells on fiber specimens is attributed solely to immobilized anti-CD20 that retains its cell-binding functions. The number density of Granta-22 cells immobilized on the fiber scaffolds was normalized using the PCL control, which captured 28.8±6.4 cells per mm^2. The CSS coating on plasma-treated PCL fibers improves the ability of the anti-CD20 functionalized fiber scaffolds to capture Granta-22 cells. Compared to the PCL control, the CSS-PCL-1 fiber scaffolds capture 35% more cells and the CSS-PCL-5 fiber scaffolds captures 139% more cells (Figure 5). A representative image of the CSS-PCL-5 fiber scaffolds with captured cells was shown in Figure 6. Because the CSS-PCL and PCL fiber scaffolds immobilized a comparable amount of anti-CD20, the increased cell capture by the CSS-coated fibers is likely due to the improved antibody orientation and function retention that is facilitated by CSS lipid membranes. In comparison to the CSS-PCL-1 fiber scaffolds, the CSS-PCL-5 fiber scaffolds display a better ability to capture cells.

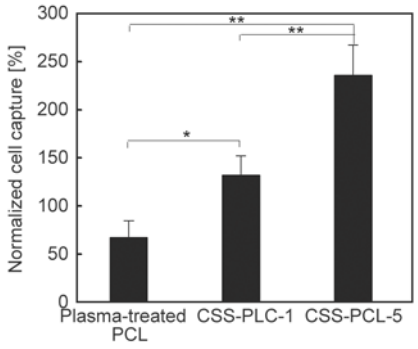

Figure 5. The normalized number of Granta-22 cells captured on the plasma-treated PCL, CSS-PCL-1, and CSS-PCL-5 fiber scaffolds. The CSS-PCL-1 and CSS-PCL-5 fibers were obtained by incubating plasma-treated PCL fibers with 1 and 5% w/v CSS solutions, respectively. All the fiber scaffolds were functionalized using anti-CD20 for cell capture. $^{*}p < 0.05$, $^{**}p < 0.01$.

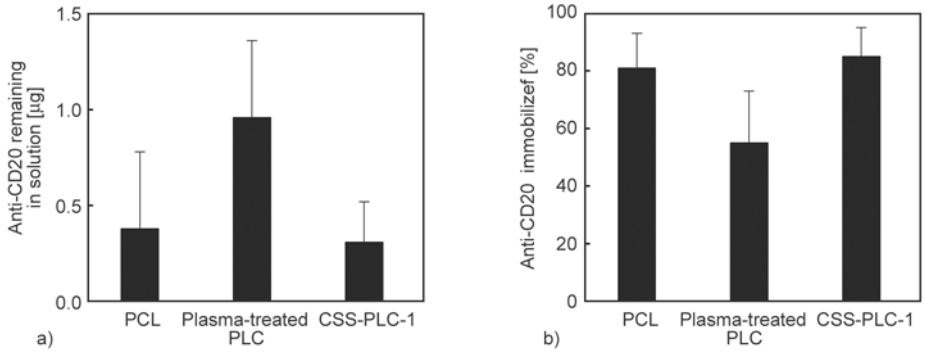

Figure 4. Anti-CD20 was immobilized onto the CSS-PCL-1 fibers and the PCL and plasma-treated PCL controls. The amount of unbound anti-CD20 remaining in solution was measured (a), and the percentage of anti-CD20 immobilized was calculated (b). Among the three fiber groups, $p > 0.05$.

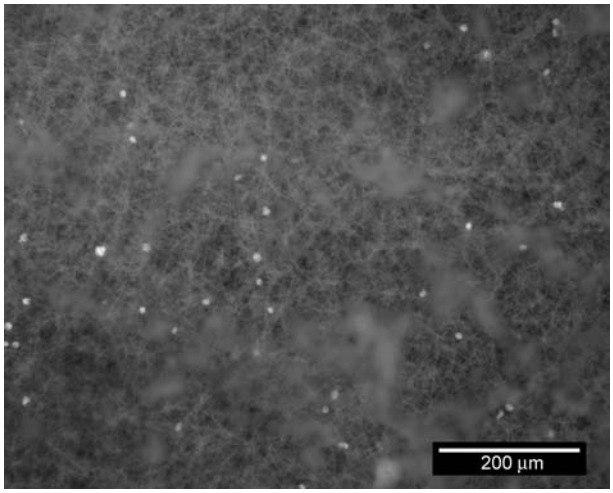

Figure 6. Optical images of the CSS-PCL-5 fibers with captured Granta-22 B cells. The cells were stained with ProLong® Gold Antifade with DAPI against the cell nuclei.

It is likely that the use of 5% w/v CSS solutions to treat plasma-treated PCL fibers improves CSS coating, which, in turn, enhances the oriented immobilization and function retention of anti-CD20. The use of more concentrated (>5% w/v) CSS solutions to treat plasma-treated PCL fibers was not pursued due to concerns of precipitation. Compared to the PCL control, the plasma-treated PCL fiber scaffolds are less effective in capturing cells. This may be due to the fact that the hydrophilic fibers immobilize less anti-CD20 and/or are less efficient in retaining antibody functions than the hydrophobic PCL fibers.

4. Conclusions

A simple and facile approach has been developed to functionalize electrospun PCL fibers. Specifically, PCL fibers are treated using air plasma and incubated with ethanol solutions of CSS at a concentration of 1~5% w/v, leading to the immobilization of CSS lipid bilayers on the plasma-treated PCL fibers. The CSS immobilization on the fibers is facilitated by chemical conjugation and confirmed by a DiO immobilization assay and micro-Raman spectroscopy. The lipid environments of the CSS-PCL fibers improve the oriented immobilization and function retention of membrane-bound proteins such as antibodies. This view is supported by results from studies on the immobilization of anti-CD20 antibodies on the CSS-PCL fibers and the capture of Granta-22 cells using the anti-CD20 functionalized CSS-PCL fiber scaffolds. Although beyond the scope of the present study, the CSS-PCL fiber scaffolds can be readily functionalized by other membrane-bound proteins to acquire cell-specific functions. The mechanically robust PCL fibers conferred with cell-specific functions may find important applications in cell and tissue engineering.

Acknowledgements

This work was supported by the US National Institutes of Health (EB009160) and National Science Foundation (CMMI0856215).

References

[1] Zhang S.: Fabrication of novel biomaterials through molecular self-assembly. Nature Biotechnology, **21**, 1171–1178 (2003).
DOI: 10.1038/nbt874

[2] Beniash E., Hartgerink J. D., Storrie H., Stendahl J. C., Stupp S. I.: Self-assembling peptide amphiphile nanofiber matrices for cell entrapment. Acta Biomaterialia, **1**, 387–397 (2005).
DOI: 10.1016/j.actbio.2005.04.002

[3] Huang L., Nagapudi K., Apkarian R. P., Chaikof E. L.: Engineered collagen–PEO nanofibers and fabrics. Journal of Biomaterials Science, Polymer Edition, **12**, 979–993 (2001).
DOI: 10.1163/156856201753252516

[4] Li W-J., Laurencin C. T., Caterson E. J., Tuan R. S., Ko F. K.: Electrospun nanofibrous structure: A novel scaffold for tissue engineering. Journal of Biomedical Materials Research, **60**, 613–621 (2002).
DOI: 10.1002/jbm.10167

[5] Buttafoco L., Kolkman N. G., Engbers-Buijtenhuijs P., Poot A. A., Dijkstra P. J., Vermes I., Feijen J.: Electrospinning of collagen and elastin for tissue engineering applications. Biomaterials, **27**, 724–734 (2006).
DOI: 10.1016/j.biomaterials.2005.06.024

[6] Qiu W., Huang Y., Teng W., Cohn C. M., Cappello J., Wu X.: Complete recombinant silk-elastinlike protein-based tissue scaffold. Biomacromolecules, **11**, 3219–3227 (2010).
DOI: 10.1021/bm100469w

[7] Genové E., Shen C., Zhang S., Semino C. E.: The effect of functionalized self-assembling peptide scaffolds on human aortic endothelial cell function. Biomaterials, **26**, 3341–3351 (2005).
DOI: 10.1016/j.biomaterials.2004.08.012

[8] Woolfson D. N., Mahmoud Z. N.: More than just bare scaffolds: Towards multi-component and decorated fibrous biomaterials. Chemical Society Reviews, **39**, 3464–3479 (2010).
DOI: 10.1039/c0cs00032a

[9] Chwalek K., Tsurkan M. V., Freudenberg U., Werner C.: Glycosaminoglycan-based hydrogels to modulate heterocellular communication in in vitro angiogenesis models. Scientific Reports, **4**, 4414/1–4414/8 (2014).
DOI:10.1038/srep04414

[10] Lee S. J., Liu J., Oh S. H., Soker S., Atala A., Yoo J. J.: Development of a composite vascular scaffolding system that withstands physiological vascular conditions. Biomaterials, **29**, 2891–2898 (2008). DOI: 10.1016/j.biomaterials.2008.03.032

[11] Gu S-Y., Wang Z-M., Ren J., Zhang C-Y.: Electrospinning of gelatin and gelatin/poly(L-lactide) blend and its characteristics for wound dressing. Materials Science and Engineering: C, **29**, 1822–1828 (2009). DOI: 10.1016/j.msec.2009.02.010

[12] Merkle V. M., Zeng L., Slepian M. J., Wu X.: Core-shell nanofibers: Integrating the bioactivity of gelatin and the mechanical property of polyvinyl alcohol. Biopolymers, **101**, 336–346 (2013). DOI: 10.1002/bip.22367

[13] Zhang Y. Z., Venugopal J., Huang Z-M., Lim C. T., Ramakrishna S.: Characterization of the surface biocompatibility of the electrospun PCL-collagen nanofibers using fibroblasts. Biomacromolecules, **6**, 2583–2589 (2005). DOI: 10.1021/bm050314k

[14] Kwon I. K., Matsuda T.: Co-electrospun nanofiber fabrics of poly(L-lactide-*co*-ε-caprolactone) with type I collagen or heparin. Biomacromolecules, **6**, 2096–2105 (2005). DOI: 10.1021/bm050086u

[15] Chiu J. B., Liu C., Hsiao B. S., Chu B., Hadjiargyrou M.: Functionalization of poly(L-lactide) nanofibrous scaffolds with bioactive collagen molecules. Journal of Biomedical Materials Research Part A, **83**, 1117–1127 (2007). DOI: 10.1002/jbm.a.31279

[16] Guex A. G., Hegemann D., Giraud M. N., Tevaearai H. T., Popa A. M., Rossi R. M., Fortunato G.: Covalent immobilisation of VEGF on plasma-coated electrospun scaffolds for tissue engineering applications. Colloids and Surfaces B: Biointerfaces, **123**, 724–733 (2014). DOI: 10.1016/j.colsurfb.2014.10.016

[17] Kim K., An H. J., Jun S-H., Kim T-J., Lim S. A., Park G., Na H. B., Park Y. I., Hyeon T., Yee C., Bluestone J. A., Kim J., Lee K-M.: Single step isolation and activation of primary $CD3^+$ *T lymphocytes* using alcohol-dispersed electrospun magnetic nanofibers. Nano Letters, **12**, 4018–4024 (2012). DOI: 10.1021/nl301388d

[18] Jun S-H., Kim K., An H. J., Kim B. C., Sonn C. H., Kim M., Doh J., Yee C., Lee K-M., Kim J.: Ethanol-dispersed polymer nanofibers as a highly selective cell isolation and release platform for $CD4^+$ *T lymphocytes*. Advanced Functional Materials, **22**, 4448–4455 (2012). DOI: 10.1002/adfm.201200657

[19] Zha Z., Cohn C., Dai Z., Qiu W., Zhang J., Wu X.: Nanofibrous lipid membranes capable of functionally immobilizing antibodies and capturing specific cells. Advanced Materials, **23**, 3435–3440 (2011). DOI: 10.1002/adma.201101516

[20] Cohn C., Leung S. L., Zha Z., Crosby C., Teng W., Wu X.: Comparative study of antibody immobilization mediated by lipid and polymer fibers. Colloids and Surfaces B: Biointerfaces, **134**, 1–7 (2015). DOI: 10.1016/j.colsurfb.2015.06.021

[21] Zhang J., Cohn C., Qui W., Zha Z., Dai Z., Wu X.: Atomic force microscopy of electrospun organic-inorganic lipid nanofibers. Applied Physics Letters, **99**, 103702/1–103702/3 (2011). DOI: 10.1063/1.3635783

[22] Venugopal J., Ma L. L., Yong T., Ramakrishna S.: *In vitro* study of smooth muscle cells on polycaprolactone and collagen nanofibrous matrices. Cell Biology International, **29**, 861–867 (2005). DOI: 10.1016/j.cellbi.2005.03.026

[23] Shin M., Ishii O., Sueda T., Vacanti J. P.: Contractile cardiac grafts using a novel nanofibrous mesh. Biomaterials, **25**, 3717–3723 (2004). DOI: 10.1016/j.biomaterials.2003.10.055

[24] Zander N. E., Orlicki J. A., Rawlett A. M., Beebe T. P.: Quantification of protein incorporated into electrospun polycaprolactone tissue engineering scaffolds. Acs Applied Materials and Interfaces, **4**, 2074–2081 (2012). DOI: 10.1021/am300045y

[25] Honig M. G., Hume R. I.: Dil and DiO: versatile fluorescent dyes for neuronal labelling and pathway tracing. Trends in Neurosciences, **12**, 333–341 (1989). DOI: 10.1016/0166-2236(89)90040-4

[26] Zha Z., Jiang L., Dai Z., Wu X.: A biomimetic mechanism for antibody immobilization on lipid nanofibers for cell capture. Applied Physics Letters, **101**, 193701/1–193701/4 (2012). DOI: 10.1063/1.4766191

[27] McKee M. G., Layman J. M., Cashion M. P., Long T. E.: Phospholipid nonwoven electrospun membranes. Science, **311**, 353–355 (2006). DOI: 10.1126/science.1119790

[28] Ma Y., Dai Z., Zha Z., Gao Y., Yue X.: Selective antileukemia effect of stabilized nanohybrid vesicles based on cholesteryl succinyl silane. Biomaterials, **32**, 9300–9307 (2011). DOI: 10.1016/j.biomaterials.2011.08.043

[29] Sackmann E.: Supported membranes: Scientific and practical applications. Science, **271**, 43–48 (1996). DOI: 10.1126/science.271.5245.43

[30] Kam L., Boxer S. G.: Formation of supported lipid bilayer composition arrays by controlled mixing and surface capture. Journal of the American Chemical Society, **122**, 12901–12902 (2000). DOI: 10.1021/ja0034038

[31] Koenig J. L.: Raman spectroscopy of biological molecules: A review. Journal of Polymer Science: Macromolecular Reviews, **6**, 59–177 (1972). DOI: 10.1002/pol.1972.230060102

[32] Barth A., Zscherp C.: What vibrations tell about proteins. Quarterly Reviews of Biophysics, **35**, 369–430 (2002). DOI: 10.1017/S0033583502003815

[33] Porwal V., Singh M., Chaturvedi D., Tandon P., Gupta V. D.: Vibrational dynamics and heat capacity in poly (L-lactic acid). Journal of Polymer Science Part B: Polymer Physics, **48**, 175–182 (2010). DOI: 10.1002/polb.21886

[34] Monti P., Taddei P., Freddi G., Asakura T., Tsukada M.: Raman spectroscopic characterization of *Bombyx mori* silk fibroin: Raman spectrum of silk I. Journal of Raman Spectroscopy, **32**, 103–107 (2001). DOI: 10.1002/jrs.675

[35] Lippert J. L., Peticola W. L.: Laser Raman investigation of the effect of cholesterol on conformational changes in dipalmitoyl lecithin multilayers. Proceedings of the National Academy of Sciences of the United States of America, **68**, 1572–1576 (1971). DOI: 10.1073/pnas.68.7.1572

[36] Reff M. E., Carner K., Chambers K. S., Chinn P. C., Leonard J. E., Raab R., Newman R. A., Hanna N., Anderson D. R.: Depletion of B cells in vivo by a chimeric mouse human monoclonal antibody to CD20. Blood, **83**, 435–445 (1994)

[37] Davis T. A., Czerwinski D. K., Levy R.: Therapy of B-cell lymphoma with anti-CD20 antibodies can result in the loss of CD20 antigen expression. Clinical Cancer Research, **5**, 611–615 (1999).